UNIVERSITY OF PADUA

DEPARTMENT OF INDUSTRIAL ENGINEERING DII

MASTER OF SCIENCE IN AEROSPACE ENGINEERING

# *Propulsion System Design of the LuNaDrone*

**Supervisor:**
***Prof. Pavarin Daniele***

**Assistant Supervisor:**
***Prof. Barato Francesco***

**Candidate:**
***Scolaro Alessandro 1234060***

Academic Year 2021/2022

# Acknowledgements

I would like to express my gratitude to my supervisor, Prof. Pavarin Daniele, for giving me the opportunity to participate in this great project. I really loved your course, even though I did not excel at the exam.

I would like to extend my sincere thanks also to my assistant supervisor, Prof. Francesco Barato, and to the project coordinator in Turin, PhD student Stefano Pescaglia. Without your constant help, also during weekends and festivities, probably, I would not have been able to conclude anything.

Another big thank you goes to my parents, Stefania and Michele, and my sister, Giulia. During these almost six years, you have always supported me, both after successes and failures. You gave me the strength to go on and get to this great achievement.

Last but not least, a special thanks is reserved for my girlfriend, Ylenia, and my friends, both close and far away. You have helped me to relax and to get distracted in difficult times, and there have been many of them in the last few years.

Without all of your help, this would have never been possible.

# Abstract

The LuNaDrone is a liquid propelled and compact size drone, able to fly autonomously. Its mission is the exploration of lunar caves since they could potentially represent shelters for human life on the Moon, guaranteeing protection from radiations and impact of micrometeorites.

This thesis is focused on the search for an actual working design for the LuNaDrone propulsion system. A preliminary study on this topic has already been done by Gabriele Podestà in his thesis, which provided for a vague idea of how the propulsion system should have been.

The first part of this dissertation is about a brief mission overview and a presentation on how the spacecraft had already been designed.

Consequently, is presented a new 50N main thruster design, in collaboration with T4i, which follows the ArianeGroup 20N canted nozzle concept. It will have a completely custom combustion chamber, with propellant inlet perpendicular to the nozzle outlet.

Having this new configuration for the main engine permits to design a completely new propellant tank, which will no longer be toroidal but cylinder shaped. It will consist in two pieces, the container and a cap, in order to insert a separation element between the pressurant and the propellant.

Then, an almost definitive and simplified design for the fluidic line is analyzed, choosing a COTS product for each component, whenever it is possible. Knowing the performances of each valve, the various pressure drops are determined and the resulting minimum propellant tank pressure is calculated.

Subsequently, the main bell nozzle is optimized in terms of length, analyzing how the decrease in expansion ratio would negatively affect specific impulse, but would greatly increase the mass of storable propellant.

In the end, a primary external structure is modelled and the attitude control system is designed. It has been calculated the minimum required thrust to provide, aiming to compensate the unwanted couples; furthermore, the maximum firing time has been determined, in order to meet the rotation angle precision and the angular velocity requirements.

# Contents

# List of Figures

# List of Tables

# Symbols

| **Symbol** | **Description** | **Unit** |
|---|---|---|
| $\Delta P$ | Differential pressure $P_1$ - $P_2$ | bar |
| $\varepsilon$ | Expansion ratio | – |
| $\vartheta$ | Yaw rotation angle precision | ° |
| $\dot{\vartheta}$ | Yaw rotational speed requirement | $^\circ\,\mathrm{s}^{-1}$ |
| $\lambda_{Inconel}$ | Thermal conductivity coefficient of Inconel | $\mathrm{W\,m^{-1}\,K^{-1}}$ |
| $\nu$ | Poisson's ratio | – |
| $\sigma_{id}$ | Ideal stress | Pa |
| $\sigma_{rr\_max}$ | Normal stress in the r-direction | Pa |
| $\sigma_{\theta\theta\_max}$ | Normal stress in the theta direction | Pa |
| $\varphi$ | Pitch rotation angle precision | ° |
| $\dot{\varphi}$ | Pitch rotational speed requirement | $^\circ\,\mathrm{s}^{-1}$ |
| $\psi$ | Roll rotation angle precision | ° |
| $\dot{\psi}$ | Roll rotational speed requirement | $^\circ\,\mathrm{s}^{-1}$ |
| $A*$ | Critical area | $\mathrm{m}^2$ |
| $A_e$ | Exit area | $\mathrm{m}^2$ |
| $A_t$ | Throat area | $\mathrm{m}^2$ |
| $A_{tf}$ | Combustion chamber supports section | $\mathrm{m}^2$ |
| $B$ | Distance between the main nozzle exit section and the mass center of the drone | m |
| $B_{x\_y}$ | $F_y$ arm along the x-direction | m |
| $B_{y\_x}$ | $F_x$ arm along the y-direction | m |
| $B_{z\_y}$ | $F_y$ arm along the z-direction | m |
| $B_{z\_x}$ | $F_x$ arm along the z-direction | m |
| $C_1$ | Unwanted couple around the x-axis, resulting from the vertical component of the thrust | N m |
| $C_2$ | Unwanted couple around the x-axis, resulting from the horizontal component of the thrust | N m |
| $C_3$ | Unwanted couple around the y-axis, resulting from the vertical component of the thrust | N m |
| $C_4$ | Unwanted couple around the y-axis, resulting from the horizontal component of the thrust | N m |
| $C_5$ | Unwanted couple around the z-axis, resulting from the horizontal component of the thrust | N m |
| $C_f$ | Thrust coefficient | – |
| $C_x$ | Total unwanted couple around the x-axis | N m |
| $C_y$ | Total unwanted couple around the y-axis | N m |
| $C_z$ | Total unwanted couple around the z-axis | N m |
| $c$ | Effective exhaust velocity | $\mathrm{m\,s^{-1}}$ |
| $c*$ | Characteristic velocity | $\mathrm{m\,s^{-1}}$ |

| Symbol | Description | Unit |
|---|---|---|
| $c_p$ | Specific heat at constant pressure | $\mathrm{kg^{-1}\,K^{-1}}$ |
| $c_v$ | Specific heat at constant volume | $\mathrm{kg^{-1}\,K^{-1}}$ |
| $D$ | Flexural stiffness of the plate | $\mathrm{N\,m^2}$ |
| $D_e$ | Exit section diameter | m |
| $D_t$ | Throat diameter | m |
| $d$ | Combustion chamber supports length | m |
| $F_x$ | ACS thrust in x-direction | N |
| $F_y$ | ACS thrust in y-direction | N |
| $f_t$ | Temperature correction factor | – |
| $g_0$ | Earth gravitational acceleration | $\mathrm{m\,s^{-2}}$ |
| $H$ | Differential pressure | bar |
| $h$ | Plate width | m |
| $I$ | Liquid flow rate: Volumetric | $\mathrm{L\,min^{-1}}$ |
| $Isp$ | Specific impulse | s |
| $I_x$ | Moment of inertia along x-direction | $\mathrm{kg\,m^2}$ |
| $I_y$ | Moment of inertia along y-direction | $\mathrm{kg\,m^2}$ |
| $I_z$ | Moment of inertia along z-direction | $\mathrm{kg\,m^2}$ |
| $K$ | Unit constant | – |
| $k$ | Heat capacity ratio | – |
| L | Lohm or liquid Ohm, measure of fluid resistance | *Lohm* |
| $L_{bell}$ | Divergent bell nozzle length | m |
| $L_{cone}$ | Divergent conic nozzle length | m |
| $M_{rr}$ | Radial moment | N m |
| $M_{\theta\theta}$ | Torsional moment | N m |
| $\dot{m}$ | Propellant mass flow | $\mathrm{kg\,s^{-1}}$ |
| $P_0$ | Combustion chamber pressure | Pa |
| $P_1$ | Upstream absolute pressure | bar |
| $P_2$ | Downstream absolute pressure | bar |
| $P_a$ | Ambient pressure | Pa |
| $P_c$ | Combustion Chamber pressure | Pa |
| $P_e$ | Exit section pressure | Pa |
| $p_0$ | Uniform pressure acting on the plate | Pa |
| $Q$ | Gas flow rate | $\mathrm{kg\,min^{-1}}$ |
| $Q_{tf}$ | Instant heat transferred by conduction | J |
| $R$ | Plate radius | m |
| $S$ | Specific gravity | – |
| $T$ | Main engine thrust | N |
| $T_{cc}$ | Combustion chamber temperature | K |
| $T_{tank}$ | Propellant tank temperature | K |
| $t_x$ | Maximum actuation time of x-direction ACS thrusters | s |
| $t_y$ | Maximum actuation time of y-direction ACS thrusters | s |
| $t_z$ | Maximum actuation time of x and y-direction ACS thrusters | s |
| $V$ | Viscosity compensation factor | – |
| $w$ | Plate vertical displacement | m |
| $w_f$ | Liquid flow rate: Gravimetric | $\mathrm{kg\,min^{-1}}$ |
| $x_1$ | Main nozzle axis offset | m |
| $x_2$ | Main nozzle axis radial inclination | ° |
| $x_3$ | Main nozzle axis tangential inclination | ° |

# Chapter 1

# Context and objectives of the study

The purpose of this thesis is to provide a direct continuation of the study[17] already been done by Gabriele Podestà, mainly focusing on subsystems not fully analyzed and on possible improvements of the elements studied in first approximation.

## 1.1 The mission

Mission statement:

*“To design a flying drone able to autonomously hover inside a lunar lava tube entering a skylight, taking photos and mapping the internal surface".*

The primary and secondary objectives of the mission derive directly from the latter and are:

Primary objectives:

- To design an autonomously flying drone.
- To provide photographic evidence of the interior of the lava tubes.

Secondary objectives:

- Provide for a map of the inside of the lava tubes
- To develop a low mass and low cost drone concept to be standardised

## 1.2 Lunar lava tubes

A lava tube is a formation that develops when a low-viscosity lava flow forms a continuous and hard crust, which thickens and forms a roof above the lava stream while it still flows. The existence of lunar lava tubes was first postulated during the early 1960's but only in the last couple decades it has been proved. The typical entrance possibilities for a lava tube are presented in Fig.1.1. A remnant of the volcanic tube, whose roof has capsized and created a valley is named a "rille". A "skylight", instead, is formed when a lava tube ceiling collapse providing a means of entrance into the tunnel. It may happen that the roof of a tube does not collapse and remain intact, with a hollow interior in most cases.

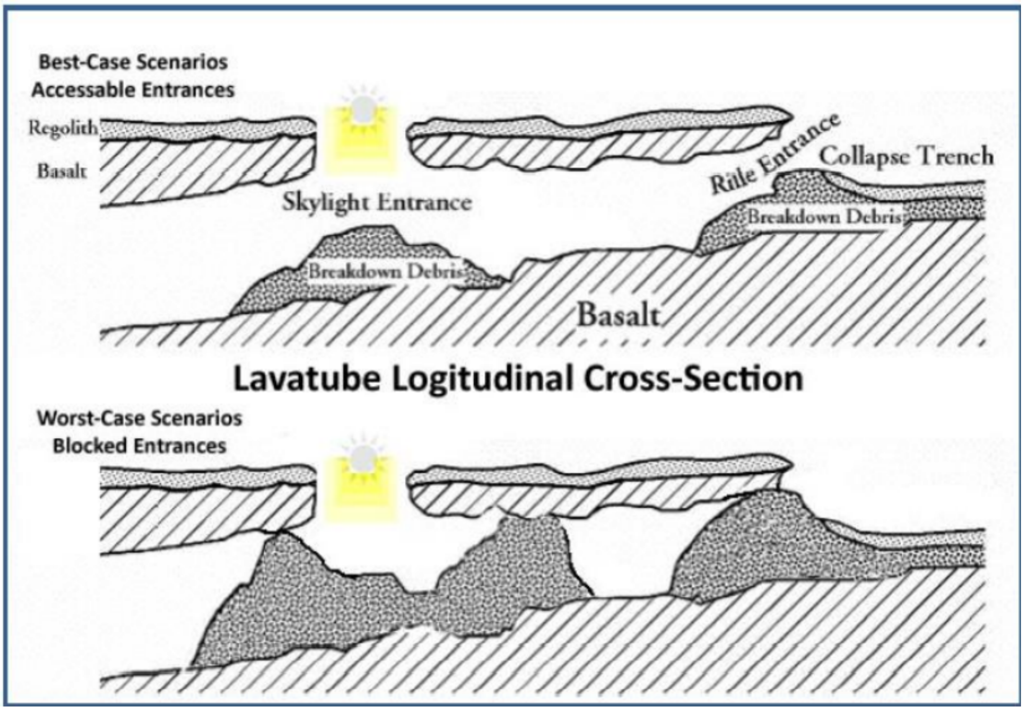

**Figure 1.1:** Potential entrance outcomes from observed pits and rilles.

Lava tubes tend to have smooth floors, with possible "soda straws" stalactites formed by lava dipping from the ceiling. Due to the lesser gravity, lava tubes on the Moon may have a much larger diameter than those found on Earth. One of the biggest pits ever detected is located in the Marius Hills region, it's skylight measures 65 metres in diameter and is 85 metres deep, with a roof thickness of around 20-25 metres. It is expected to hide a large cavern beneath the visible surface that extends about 60 $km$ to the west of the skylight, where the cavern itself is approximately 30 $km$ in length. This makes the idea of how lava tubes could protected from the harsh environment of the lunar surface, which is bombarded by radiation, micro-meteorites impacts and experiences temperature extremes.

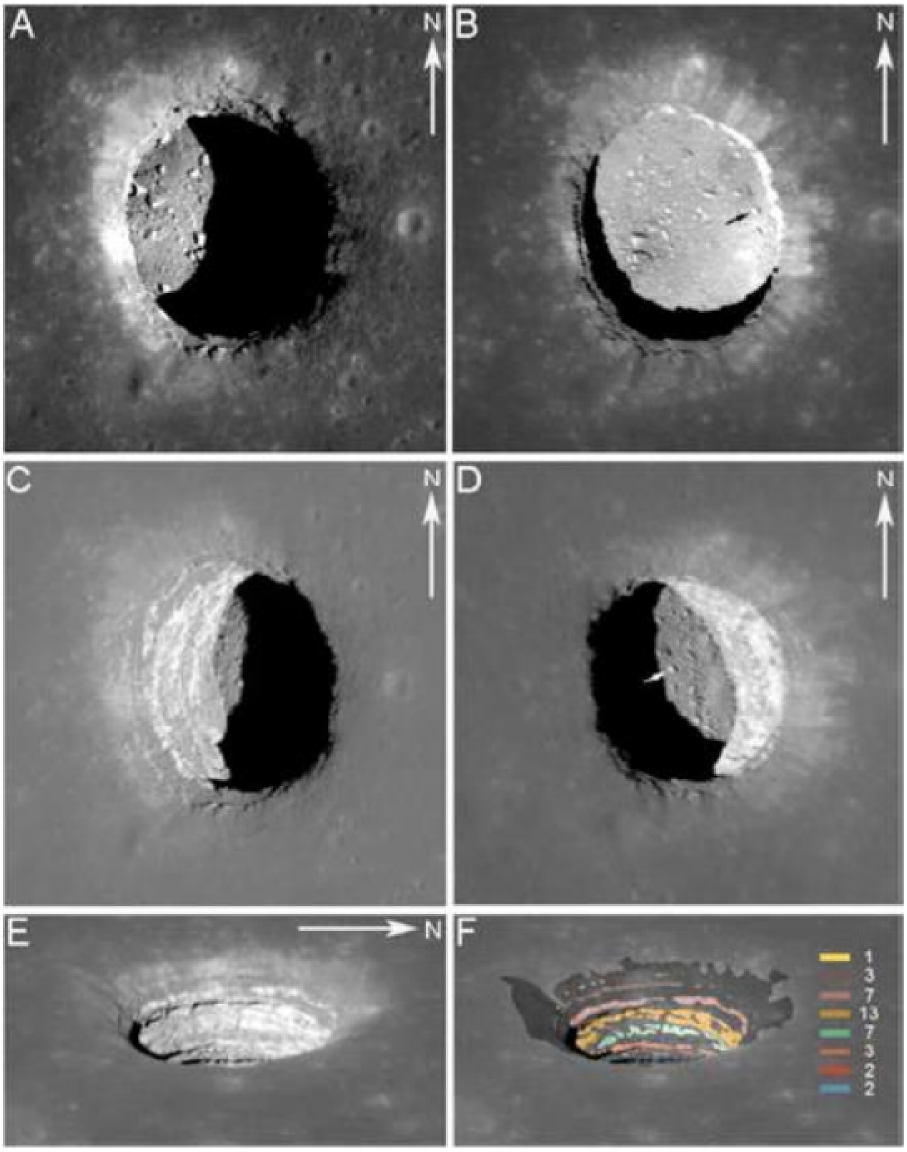

**Figure 1.2:** Mare Tranquillitatis pit.

The thickness of the caves roof could be even a few tens of metres, that would certainly be advantageous speaking about radiation protection, however, it would represent an obstacle for the implementation of a communication system between the inside and the outside of these caves.

## 1.3 Mission overview

The mission concept is based on the assumption that a lander and/or a rover would deploy LuNaDrone in the proximity of a selected skylight, from there it will start its flight, which consist in three main phases: vertical ascent, horizontal translation and descent.

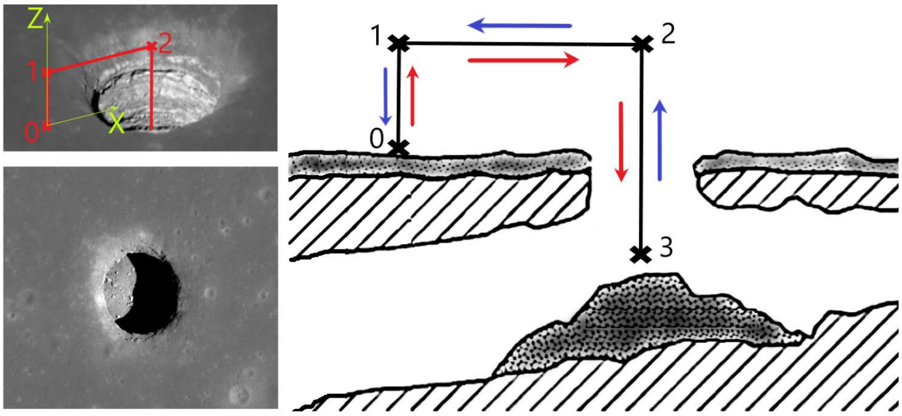

**Figure 1.3:** Drone trajectory.

In Fig.1.3 it is shown a scheme of the possible trajectory that the drone will follow, starting from point 0 at a predetermined distance from the entrance of the pit, it will start the first phase, the vertical ascent, that will end at a predetermined height corresponding to point 1. The following segment involves the horizontal translation from point 1 to point 2, situated over the pit. Finally the segment 2-3 refers to the vertical descent that will lead the drone inside the pit, where he can take the photos required. At the end of each flight segment, it is assumed that the drone will have no residual velocity and, if required, could hover for a predetermined time frame. Once accomplished its mission he will follow the same trajectory in reverse in order to go back to the starting point.

In order to fulfil this purpose, the drone must comply many functional, performance, interface, operational and implementation requirements, among all, the most important ones regarding the propulsion system design are:

- The LuNaDrone shall be able to fly autonomously, departing from the surface of a rover, entering in a target Lunar Cave and leaving it at the end of its mission, landing on the Moon surface or returning to the rover.
- The LuNaDrone shall be equipped with a propulsion system able to complete the entire mission.
- The LuNaDrone wet mass shall be less than 15 $Kg$.
- The volume of the LuNaDrone shall be less than 30x20x20 $cm$ while in stowage in the rover.
- The LuNaDrone shall make use of non-toxic propellants that are safe to handle on ground.

## 1.4 Initial propulsion system architecture

As already mentioned at the beginning of this work, a preliminary design of the LuNaDrone propulsion system has already been analyzed[17]. The final results of that analysis asserted that the best configuration, among those taken into account, is a liquid propellant propulsion system, with a pressure regulated feed system as shown in Fig.1.4. This design has been the starting point of the present dissertation.

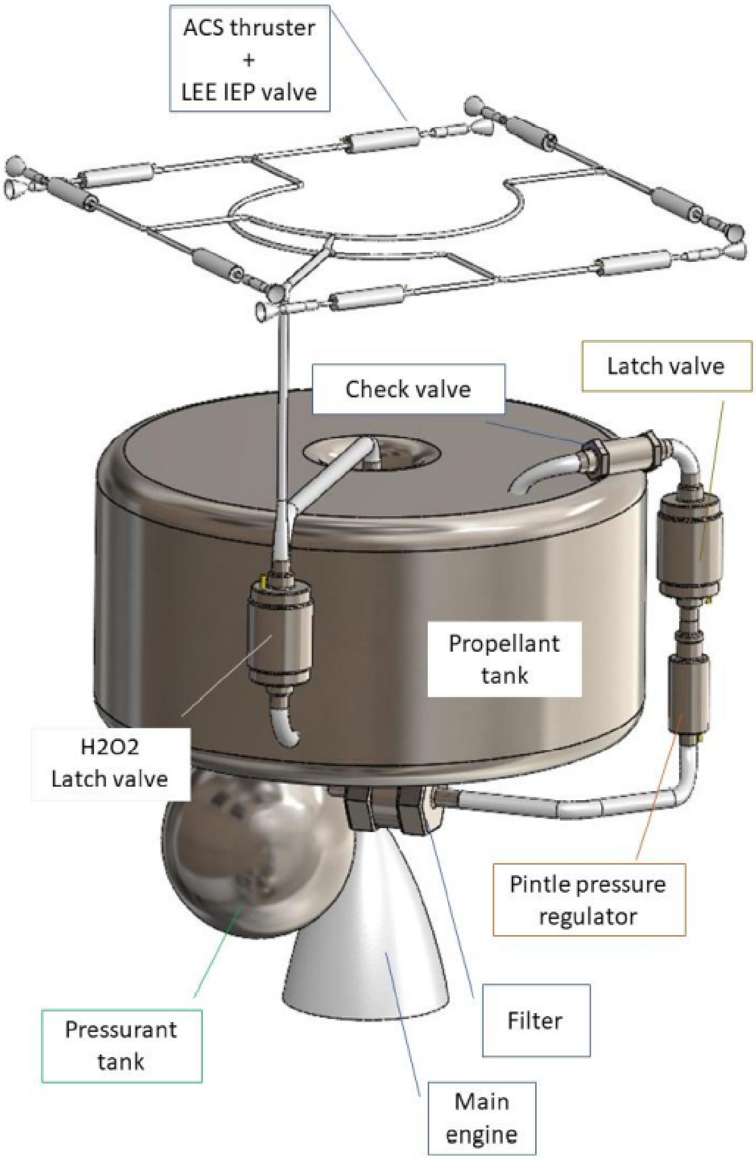

**Figure 1.4:** Propulsion system design.

Starting from the top of the image there are the eight attitude control thrusters, providing 1 N of thrust each, and their fluidic line; the inflow is coming from the toroidal shaped propellant tank at 20 *bar*, with an almost rectangular section where the angles are fitted with 10 *mm* radius,thanks to a latch valve which divide the flow between the ACS (Attitude Control System) and the main thruster. It was thought that, for encumbrance reasons, the best solution to fit all the needed elements in a 30x20x20 *cm* volume, was to make the in-line main engine pass through the inner hole of the toroidal tank. Anyways, this solution raised many doubts because of the problems of the internal bladder, which should have been very difficult to shape and mount, and the internal stresses, that in this case exceed the 170 *MPa* limit imposed by the material (AISI 316 stainless steel). Below the propellant tank there is one titanium spherical tank for the pressurant at 350 *bar*, with attached filter and valves, working with Nitrogen. The main engine is a monopropellant liquid thruster, working with 90% Hydrogen peroxide manufactured by T4i, which is a spin-off from the University of Padua, and it consists of an injection plate, a catalytic bed, a decomposition chamber and a nozzle. The entire engine could be built by using additive manufacturing in Inconel 718. In table 1.1 are shown the values of the main useful parameters chosen or calculated during the previous work.

| Parameter | Value |
|---|---|
| Decomposition Temperature | 750 °$C$ |
| Characteristic velocity | $950\ \mathrm{m\,s^{-1}}$ |
| Chamber Pressure | 10 bar |
| Propellant Flow | $0.0329\ \mathrm{kg\,s^{-1}}$ |
| Specific Impulse | 155 s |
| Nozzle Correction Factor | 98 % |
| Expansion Ratio | 70 |
| Percent of 15° cone nozzle | 70 % |
| Initial Parabola Angle | 34° |
| Final Parabola Angle | 10.5° |
| Bed Loading | $100\ \mathrm{kg\,m^{-2}\,s^{-1}}$ |
| Thrust | 50 N |

**Table 1.1:** Most important parameters of the main engine

In conclusion, the final design for the main thruster is represented in Fig.1.5.

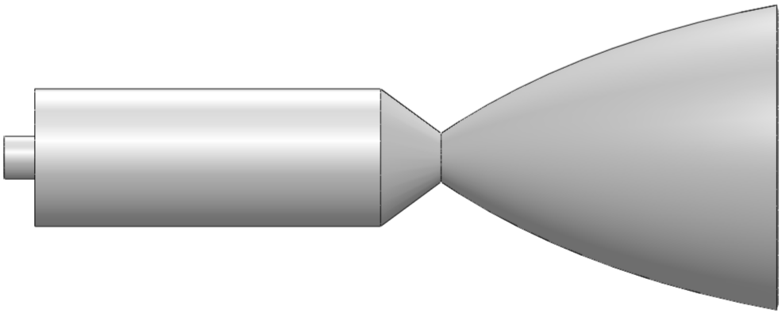

**Figure 1.5:** 50 $N$ main thruster.

For what regards the fluidic line, only a few between all the needed valves were chosen and implemented in the CAD model, due to the complexity of finding miniaturized products which fulfill the drone requirements. For this reason, an almost completely new analysis will be discussed in Chapter 4. A schematic idea of how the fluidic line was designed is shown in Fig.1.6. The whole fluidic line supports 1/4" tubes except for the ACS ones, because they require a much smaller mass flow rate.

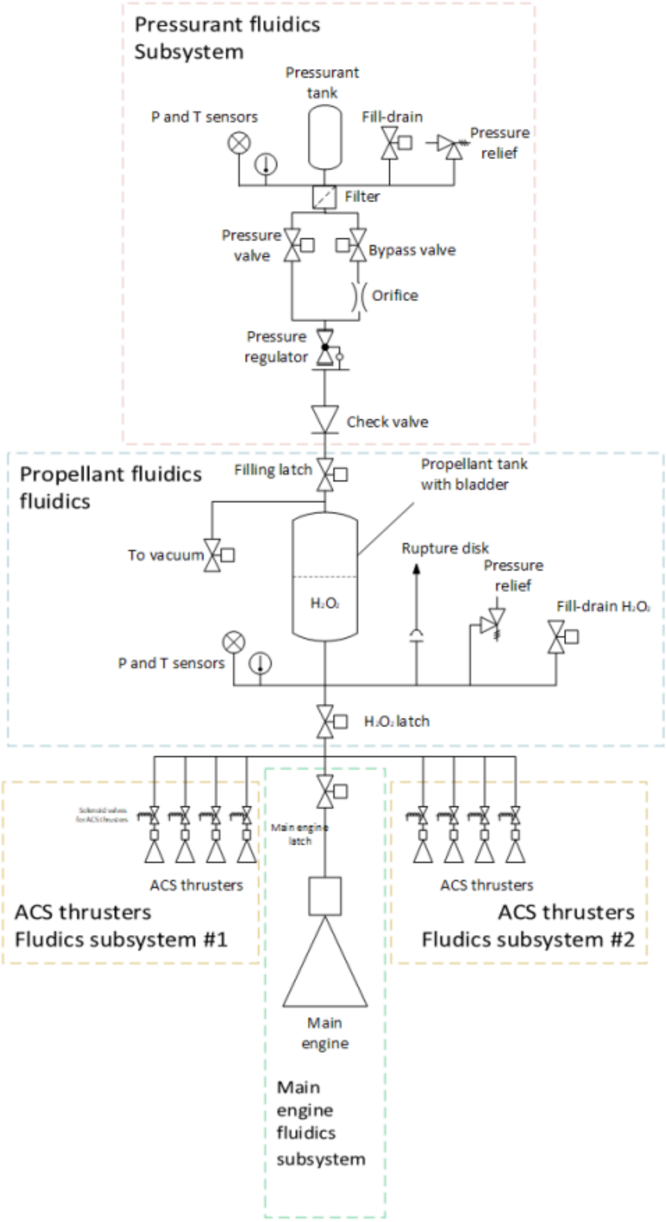

**Figure 1.6:** Scheme of the fluidic line.

# Chapter 2

# Main thruster design

In this chapter will be analyzed a potentially better configuration for the main engine, with the purpose of gaining available volume inside the drone. Having more space available inside the 30x20x20 $cm$ volume would mean that a bigger propellant tank could be designed, so that a greater amount of Hydrogen Peroxide could be carried, enabling the possibility of spending more time in hovering, if necessary, or even to make more than one trip inside the lunar lava pit.

## 2.1 Canted nozzle

Traditionally, the combustion chamber and nozzle are located in the rear of a satellite/missile, in this case a drone, with the axis of the nozzle coincident with the centreline of the rest of the engine. However, it could happen that in some cases the requirements of satellites or missiles demand to place some equipment on the rear of the propelled vehicle, so that the propulsion system needs to be moved forward. For such applications, the nozzle axis necessarily can no longer coincide with the engine axis; instead, the nozzle is canted at an angle to the rest of the engine centreline. Of course this leads to a side force that in these applications can be balanced using more nozzles in a symmetrical configuration.
An example of the of this kind of applications is shown in Fig.2.1, where the inflow and the exhausts are not only misaligned, but even reversed.

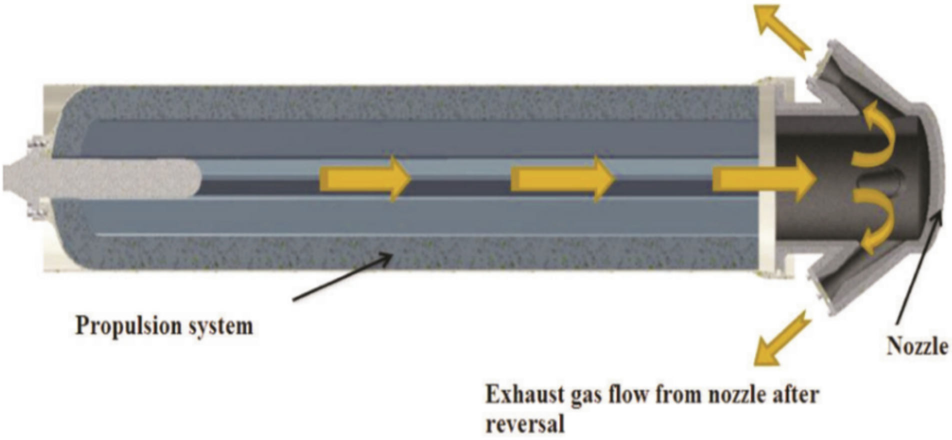

**Figure 2.1:** Example of application where the inflow and the exhausts are not aligned.

In this case study even if there is not any equipment positioning requirement that demands to use a canted nozzle configuration, it could be a great advantage in terms of exploitation of available volume. The actual configuration for the main engine provides for an in-line thruster extending along the height of the drone, which forced to think about a possible solution in terms of encumbrance for the design of the propellant tank. This led to a toroidal tank, with an almost rectangular section where the angles are fitted with 10 $mm$ radius, as can be seen in Fig.2.2.

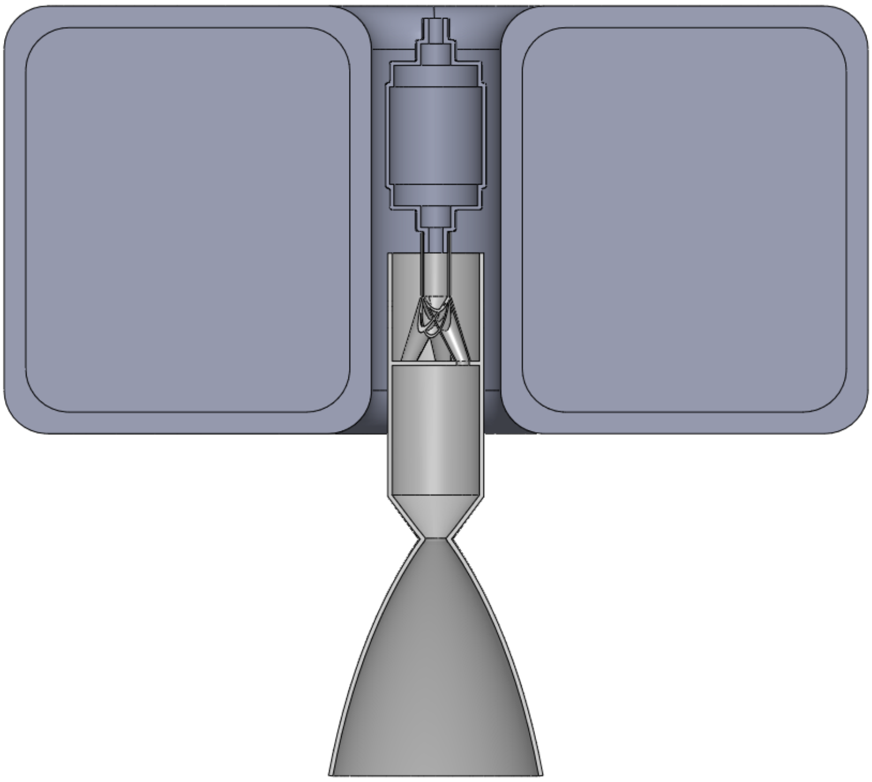

**Figure 2.2:** Section view of main engine passing through the toroidal shaped tank.

Choosing this shape instead of a traditional cylinder would lead to an increase of the height of the tank in order to obtain the same internal volume, that is, the amount of propellant to carry. Furthermore it would also represent an issue under many other aspects, first of all the difficulties on a constructive level to insert a toroidal bladder in order to separate the pressurant end the propellant, the possible thermal issues linked to having the engine emanating heat passing through the tank, as well as the high stresses on the walls that exceed the 170 $MPa$ limit imposed by the material, and last but not least, the mass increase linked to the inner lateral face added.

Keeping this in mind, it was thought that if only the main engine could not be aligned with the nozzle, there would be no need to making it pass through a toroidal tank. For this reason a canted nozzle configuration has been taken into account.

The model taken as reference for the design of a canted nozzle thruster is the ArianeGroup 20 $N$ Chemical Monopropellant Hydrazine Thruster[3], shown in Fig.2.3, which is designed for attitude, trajectory and orbit control of satellites, spacecraft and platforms.

**Figure 2.3:** 20 *N* Chemical Monopropellant Hydrazine Thruster by ArianeGroup.

For this specific thruster, the exhaust direction is perpendicular to the inflow direction, which is exactly what we are looking for. The whole length of the engine is 195 $mm$, which would seem to make it incompatible with the LuNaDrone because of the very limited volume of 30x20x20 $cm$. However most of the 20 $N$ thruster length is given by a flow control valve, consisting of two identical monostable, normally-closed valves placed in series within a single housing. This means that in our case study it would be possible to just separate this valve from the rest of the engine and place it in a different misaligned configuration, to make it fit inside the drone.
A possible solution for the positioning of the valves is like a serpentine, as shown in Fig.2.3. The propellant flow starts from point 1 where the tube is inserted in the bottom of the tank, then pass through the first latch valve, corresponding to point 2 in the figure, then a pipe junction (3) separates the flow and directs a part of it towards the ACS while the rest proceed towards the main engine latch valve (4), after this there is the injection plate (5), the catalytic bed (6) and finally the combustion chamber and nozzle (7).

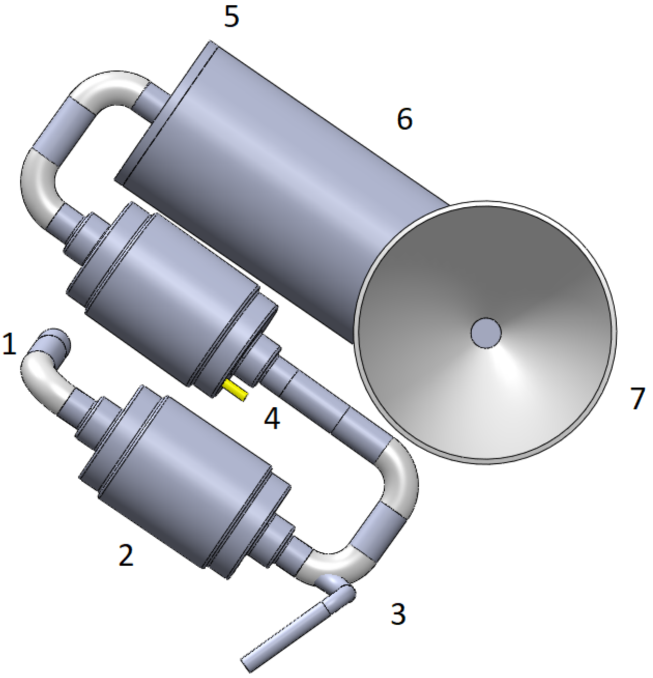

**Figure 2.4:** Bottom view of the main engine.

The combustion chamber has been redesigned to look like the ArianeGroup one, but maintaining the same internal volume of the cylindrical previous one, so that the engine could ideally work at the same pressure range, maintaining the same nozzle and continuing to provide 50 $N$ thrust. A more detailed view of the combustion chamber will be illustrated in Annex E.

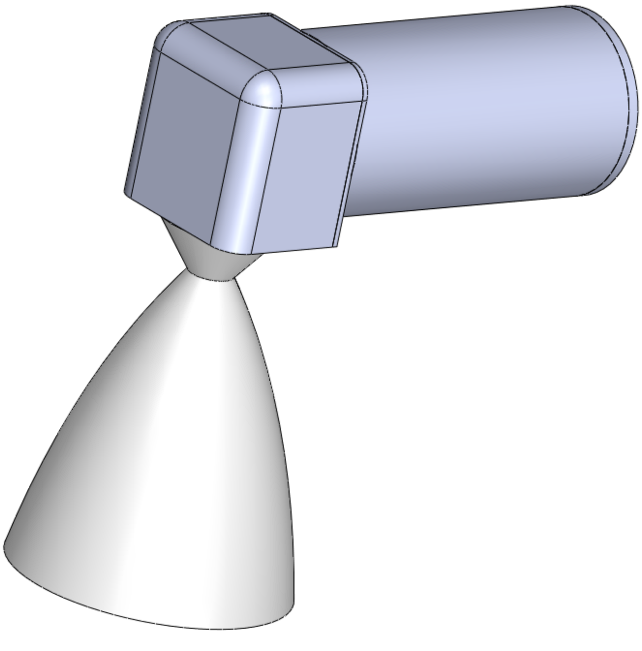

**Figure 2.5:** New combustion chamber design.

Note that that this design is based on the hypothesis that the asymmetry of the flow at the nozzle entry, that is further enhanced when the nozzles are canted, does not affect thrust and its direction. To be able to properly affirm this, a CFD analysis should be carried on. A similar study is displayed in "Numerical Simulations of Canted Nozzle and Scarfed Nozzle Flow Fields"[10], where CFD techniques are used to study the effects on the exhaust of asymmetric inlet flow field of canted nozzles. The study is on an end burning rocket with solid double base propellant, where the products of combustion are exhausted from two conical nozzles that are not canted at 90°, but at a smaller angle. However, since this would be an even worse condition, because the fumes are already produced and just deflected by a canted nozzle, it is reasonable to considerate the results as valid also for our case study. The analysis results show that, because of the canting of the nozzle as well as the position of it on the motor, the flow field at the entry of the nozzles has not the same direction of the flow at the start of the motor. This flow asymmetry at the entry of the nozzle is found to reduce and finally vanish with the passage of time. Also the axial distributions of Mach numbers through the nozzle indicate that the flow field becomes axisymmetric near/before the throat section and the thrust vector would not have any misalignment with the nozzle axis.

Based on these considerations, the hypothesis that the asymmetry of the flow at the nozzle entry does not affect thrust and its direction can be considered valid, even if a proper CFD analysis could be useful.

## 2.2 Combustion chamber supports

The system combustion chamber plus nozzle, described in Section 2.1, nominally provides 50 $N$ of thrust aligned whit the direction of the axis of the nozzle, however a system to transfer the thrust from the combustion chamber to the entire drone is needed. If the thrust has no means to be transferred to the whole drone, during the periods when the engine is on, the exhausts will act on the combustion chamber and the related fluidic line just like an end load acts on a rigid beam, moving and bending all the tubes. This would result in a very dangerous situation in terms of possible breakage of the components as well as the changes in the direction of the thrust, that would lead to attitude control and navigation problems.

For these reasons, it has been thought to a possible way to transfer the thrust from the combustion chamber directly to the propellant tank, which will be a steady element of the drone, fixed directly to the external structure.

The most reasonable solution is probably to connect combustion chamber and propellant tank by means of four supports in Inconel 718, a precipitation hardenable nickel-based alloy designed to display exceptionally high yield, tensile and creep-break properties at temperatures up to 704 $°C$. These supports are shaped like a cylinder with the bases resting one on the top face of the combustion chamber, connected to the four superior edges, and one on the bottom face of the propellant tank, while the centerline is not perpendicular to them but is inclined by an angle a shown in Fig.2.6.

Some really important aspects to take into account while designing these supports are that they must handle the stresses, caused by the decomposition chamber that presses them against the propellant tank, and that they also act like four thermal fingers that transfer heat from a solid body to another.

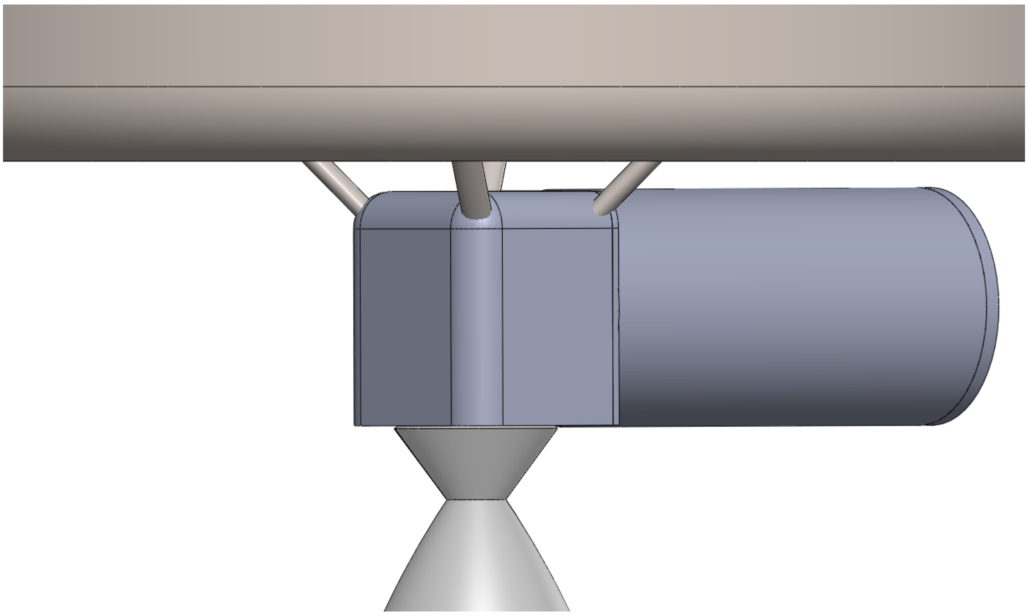

**Figure 2.6:** Mechanical supports for the combustion chamber.

The choice of the material of the supports is one of the most important parameters, together with the inclination angle and the section surface, because it has to be strong enough to resist to the stresses, resist at relatively high temperatures (up to around 650 $°C$) and to have a low thermal conductivity so that the propellant tank temperature will not rise too much during the firing time.
Choosing Inconel 718 seems to be the most valid idea, because it has exceptionally high yield, tensile and creep-break properties in a range of temperatures that includes the operative one of this case study, moreover being the same material the combustion chamber will be made of, it will be possible to produce them as a unique item, maybe through additive manufacturing.
Many simulations have been carried on, varying the inclination angle of each cylinder, and consequently its length, the section area and the positioning of the inferior base on the combustion chamber. The physical principle behind these simulation is a pure heat conduction, where the heat is transferred from a hotter body, the combustion chamber at around 650 $°C$, to a colder one, the propellant tank at around 25 $°C$, by means of four thermal fingers.
In Eqn.2.1 is shown how to determine the instant heat transferred by conduction by all the four cylinders combined, $A$ represents the section of the cylinder, $d$ represents its length, $T_{\text{cc}}$ the temperature of the combustion chamber, $T_{\text{tank}}$ the temperature of the tank and $\lambda_{\text{Inconel}}$ the thermal conductivity of Inconel 718. Note that the 4 in Eqn.2.1 is referred to the four thermal fingers, each acting like a a bridge for the transfer of heat.

$$Q_{tf} = 4 * \frac{(T_{\text{cc}} - T_{\text{tank}}) * A * \lambda_{Inconel}}{d} \tag{2.1}$$

All the assumptions used were chosen in the most conservative way, assuming that the maximum heat transferable will be transferred for the whole simulation time, which is at least double the time of firing of the main engine. This would be like considering that the thruster fires constantly for the duration of two flights roundtrip, with the combustion chamber at the maximum temperature of 650 $°C$ for the whole time, from the instant it is turned on to the instant it is turned off.

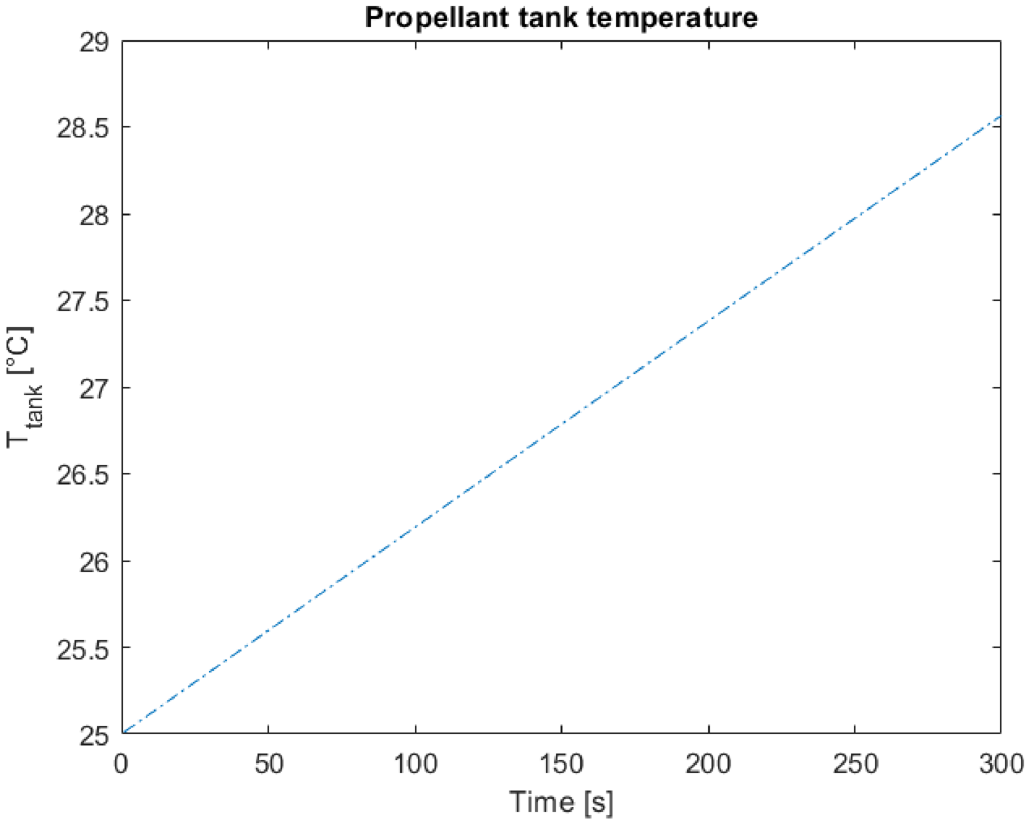

**Figure 2.7:** Tank temperature trend.

In Fig.2.7 it is shown the evolution trend of the temperature of the tank, the simulation has been protracted for 300 seconds where, after each second, the new tank temperature was calculated so that for the following time step it will be used for the calculation of the correct heat transferred through conduction. It can be seen that there is not a relevant increase in the propellant tank temperature, the only lack of this simulation that could have distorted a little the results is that it is not considered that the propellant tank could have a non homogeneous increase of temperature, so that probably in proximity of the supports it will have a little higher temperature while far from them it will be lower than the estimated one.

A large range of values for the inclination angle and the section area were analyzed through this simulation: the radius of the section area was varying from 1 $mm$ to 5 $mm$ while the inclination angle was varying from 0°, that is perpendicular to both combustion chamber and propellant tank, to 75°.

However, it must not be forgotten that the purpose of these four Inconel 718 supports is to transfer the thrust from the combustion chamber to the propellant tank, without allowing the fluidic line to bend or shift. For this reason, after the thermal analysis, when a possible design of these supports were chosen, a mechanical analysis has been perpetuated.

Through the Solidworks simulation add-on, a stress/strain/displacement analysis has been carried on the selected design, in order to verify that the stresses to which the supports are subjected do not exceed the yield stress of Inconel 718, with a factor of safety of 2, using the von Mises criterion. In Fig.2.8 the results of this simulation are shown proving that, even on the most critical areas, the stresses are less than half of the yield stress value.

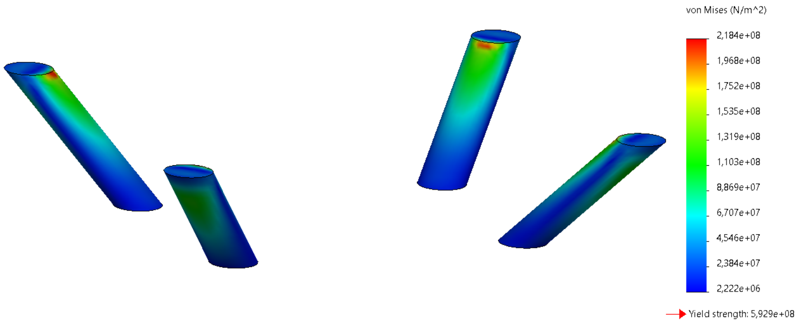

**Figure 2.8:** Von Mises stresses on the combustion chamber supports.

By virtue of the thermal and mechanical simulations that have been carried on, the final design chosen for the supports is a symmetric layout with the four cylinders placed at the four superior edges of the combustion chamber, 2 *mm* of section radius and 45° of axis inclination.

# Chapter 3

# Propellant tank design

In this chapter, will be analyzed in detail the design of the new propellant tank and fluidic line.
As already said in Chapter 2, having a canted nozzle configuration permits to do not have a toroidal shaped propellant tank but a classic cylinder with rounded edges, so that a greater amount of Hydrogen peroxide could be carried, for equal height of the tank.

## 3.1 Propellant tank

Since the design of the main thruster no longer provides for an axis symmetric engine but a canted nozzle thruster, the propellant tank is no longer required to have a cavity through which should pass the combustion chamber and valves. A more efficient shape, in terms of volume encumbrance compared to contained quantity of propellant, could be chosen and the most efficient is a classical cylinder.
Satisfying the requirement of internal volume of the tank shown in table 3.1, a cylindrical tank has been shaped, as shown in Fig.3.1, where the internal radius is 93 $mm$, the height is 87.69 $mm$, the thickness of the lateral surface is 2 $mm$ while the bases one is 5 $mm$.

| | | |
|---|---|---|
| Required internal volume | 2372479 $mm^3$ | 2.372479 *litres* |
| Toroidal shaped internal volume | 2380552 $mm^3$ | 2.380552 *litres* |
| Cylinder shaped internal volume | 2380730 $mm^3$ | 2.380730 *litres* |

**Table 3.1:** Internal volumes for propellant tank.

The Radius has been chosen as the maximum possible, considering the thickness of the external structure of the drone, which is 5 $mm$, and the minimum thickness of the lateral surface of the cylinder where the first one is a standard value that will be discussed in Chapter 4, while the second one is chosen in order to satisfy the maximum stress tolerable by the material, which is AISI 316 stainless steel, with a factor of safety of at least 2 in respect to the yield stress. The height of the tank, instead, is simply calculated starting from the required internal volume by dividing by the base area.

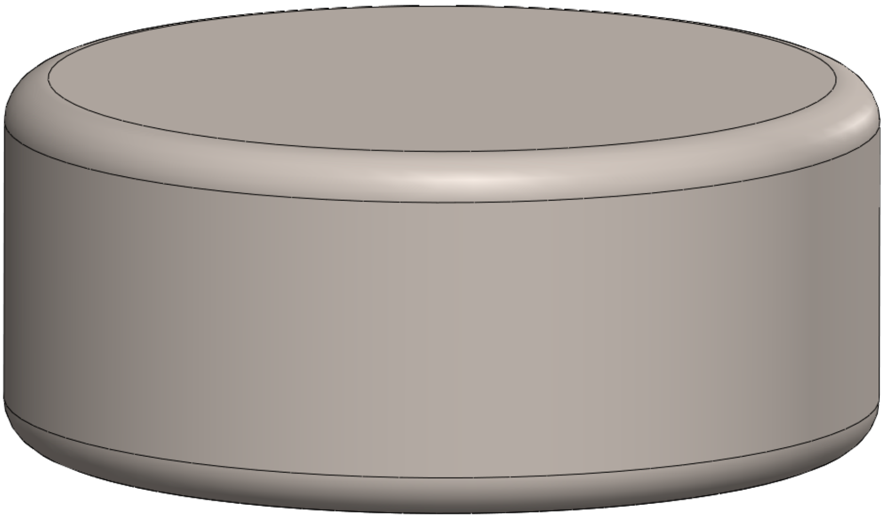

**Figure 3.1:** Cylindrical tank basic design.

The radius of the tank was chosen this way not only in order to obtain the lower possible value of its height, but also because more than likely, the tank will be a structural element of the drone. Making the cylinder perfectly fit inside the available dimensions will allow to easily fix its lateral surface to the four structure lateral panels. This would mean that the biggest element inside the drone could be used as a support for many other smaller parts, as for example the combustion chamber supports that transfer the thrust to the whole system.

### 3.1.1 Stress analysis

The final design of the propulsion system provides for a pressure regulated pressurant flow, in order to work at a constant pressure in the propellant tank of 18 *bar*, as will be shown in Chapter 4.
This means that the tank must be able to resist the internal pressure of 18 *bar* without any relevant displacement, maintaining the stresses always lower than the yield stress of the material, with a factor of safety of at least 2. After a Finite Element Method (FEM) simulation[1] it is discovered that this does not represent a problem for the lateral surface of the cylinder, but it does for the lower and upper base. In order to re-enter the range of admissible values, three possible solutions where analyzed: make the upper and lower walls thicker, attach some kind of external isogrid to reinforce the bases and analyze other possible materials and geometries for the whole tank.
The first solution provides for increasing the thickness of the whole upper and lower faces, until the stresses on the most critical spots will be at most half of the yield stress of AISI 316 stainless steel, following the von Mises criterion. As can be seen in Annex B, the upper and lower bases host the most critical stresses in the middle of each face and in correspondence of the edges, as expected if we look at the analogy with a circular embedded plate subjected to a uniform pressure $p_0$, as the one shown in Fig.3.2.

---

[1] All the results of the analysis mentioned in this chapter are shown in detail in Annex B

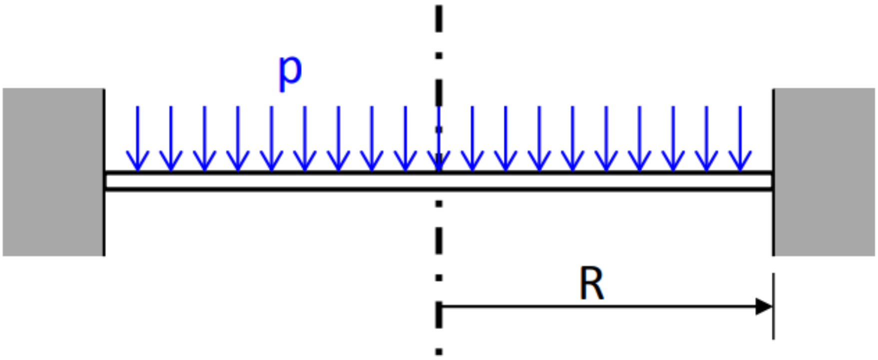

**Figure 3.2:** Circular embedded plate subjected to a uniform pressure $p_0$.

$$\sigma_{id}(r) = \max\left(\left|\sigma_{rr\_\max}\right|, \left|\sigma_{\theta\theta\_\max}\right|\right) \tag{3.1}$$

The Eqn.3.1 suggests that the maximum stresses on the plate will be in correspondence of the maximum between $\sigma_{rr\_\max}$ and $\sigma_{\theta\theta\_\max}$, which are respectively the normal stress in the r-direction the normal stress in the theta direction,

$$\begin{aligned} \sigma_{rr\_\max}(r) &= \frac{6M_{rr}(r)}{h^2} \\ \sigma_{\theta\theta\_\max}(r) &= \frac{6M_{\theta\theta}(r)}{h^2} \end{aligned} \tag{3.2}$$

which in turn correspond to the maximum of $M_{rr}(r)$ and $M_{\theta\theta(r)}$, respectively the radial moment and the torsional moment as a function of $r$, radius of the plate.

$$\begin{aligned} M_{rr} &= -D\left(\frac{d^2w}{dr^2} + v\frac{1}{r}\frac{dw}{dr}\right) = \left[\frac{(1+v)p_0R^2}{16} - \frac{(3+v)p_0r^2}{16}\right] \\ M_{\theta\theta} &= -D\left(\frac{1}{r}\frac{dw}{dr} + v\frac{d^2w}{dr^2}\right) = \left[\frac{(1+v)p_0R^2}{16} - \frac{(1+3v)p_0r^2}{16}\right] \end{aligned} \tag{3.3}$$

$M_{rr}(r)$ and $M_{\theta\theta(r)}$ are shown in Eqn.3.3, where $D$ stands for the flexural stiffness of the plate and $v$ stands for the Poisson ratio.
The trend of these moments as a function of the radius is shown in Fig.3.3, noting that in this specific example the maximum radius is worth 1.5 $m$.

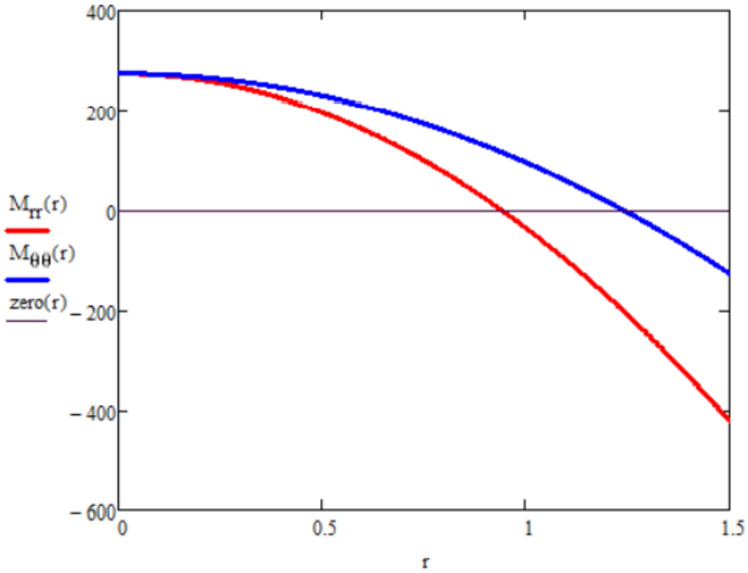

**Figure 3.3:** Trends for the radial and torsional moment on the circular plate.

This means that the ideal normal stress should have a local maximum in correspondence of $r = 0$, the middle of the plate, and an absolute maximum in $r = R$, where the plate is embedded, as can be seen in Fig.3.4, just like the simulation on the tank shows.

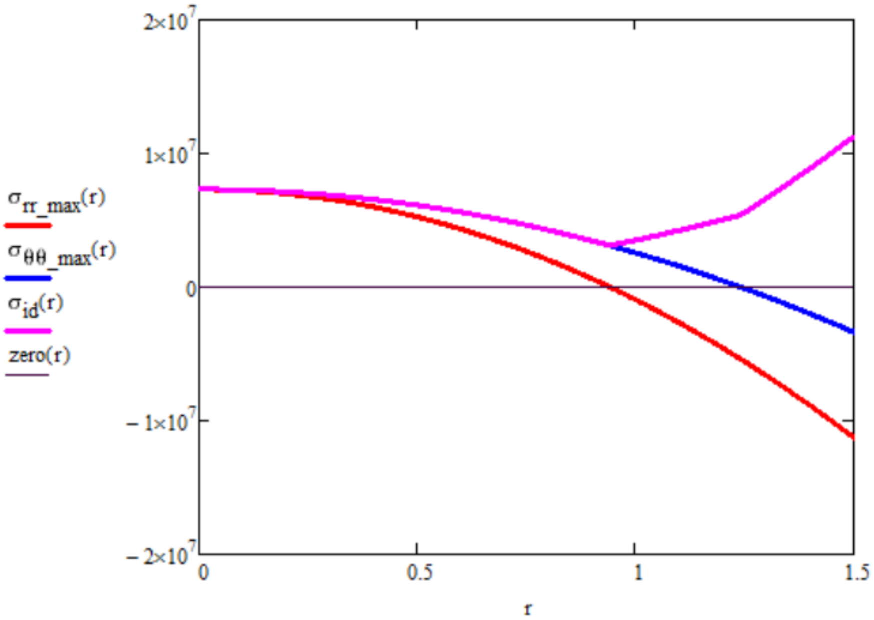

**Figure 3.4:** Trends for the r-direction, theta direction and ideal normal stresses on the circular plate.

Considering our case study, the actual thickness of each base of the tank is 5 $mm$ while the lateral surface thickness is 2 $mm$, the bases are filleted to the lateral face with a curvature radius of 10 $mm$; according to the simulations, in order to have a tolerable stress in correspondence of the center of the bases and near the edges, the thickness of the bases should be increased by around 10 $mm$, reaching almost 15 $mm$. The size of this thickness increase can be appreciated in Fig.3.5.

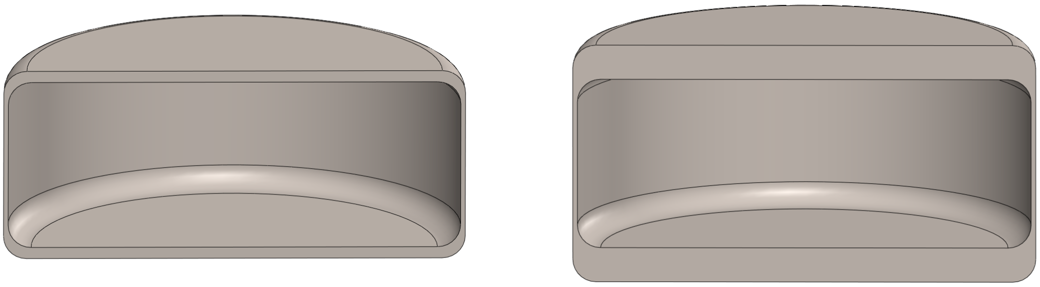

**Figure 3.5:** Evolution of the bases thickness of the propellant tank in order to withstand the stresses caused by the 18 *bar* of internal pressure, from 5 *mm* to 15 *mm*.

This solution would means of course an increment in terms of volumes, but most importantly in term of mass, because this way the tank mass will rise starting from 4.457 *kg* and reaching 9.005 *kg*, remembering that the tank material is AISI 316 stainless steel.
The second solution, instead, provides for fixing to the upper and lower bases an isogrid like reinforcement, taking advantage of the fact that is much harder to bend an high and thin beam compared to a low and thick one with the same volume. This way, instead of thicken the whole surface, only a minimal part will be increased in height but of a greater quantity.
Thinking about a possible design for this isogrid, the simplest and possibly best configuration is the one shown in Fig.3.6, which includes an outer thin ring with a 78 *mm* diameter and an inner thin ring with a 30 *mm* diameter, linked by four thin radii.

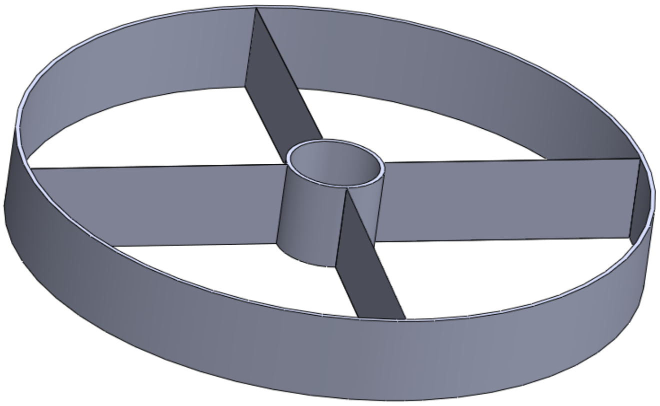

**Figure 3.6:** Possible design for the isogrid reinforcements for the upper and lower bases of the propellant tank.

This design includes 1 *mm* thin walls, 40 *mm* high. According to the simulations, the stresses to which the bases are subjected if reinforced with an isogrid of this kind are barely equal to the yield stress of AISI 316 stainless steel, surely there is not a safety factor of 2. The relatively great height of these reinforcements is for sure a very limiting factor for the design of the propulsion system, because the available volume is already very low and furthermore it must be considered that under the propellant tank will be placed all the valves of the fluidic line, the catalytic bed, the pressurant tank, the combustion chamber and the main engine. It can be easily seen just by looking at the new tank shown in Fig.3.7 that this is a much complex task.

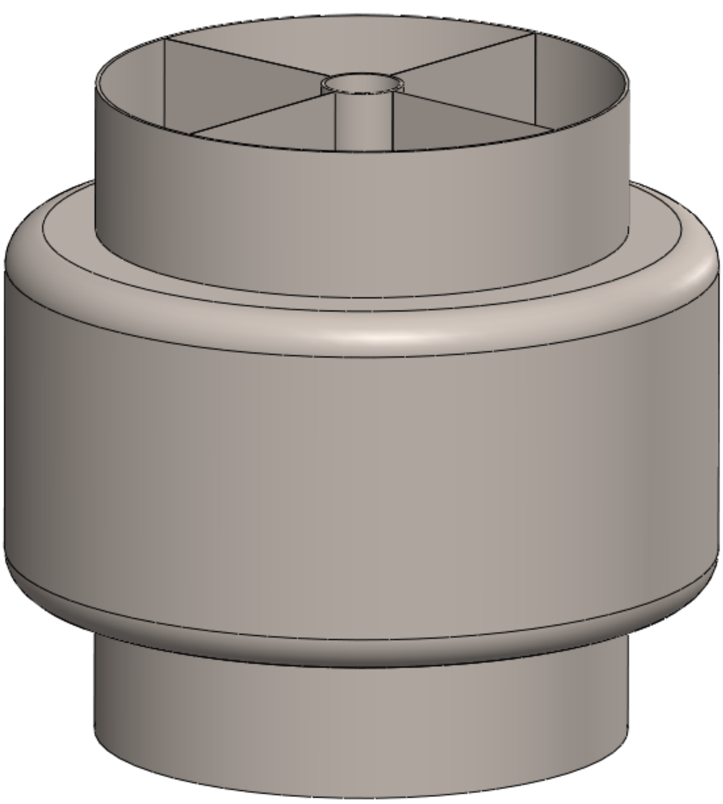

**Figure 3.7:** Propellant tank with bases reinforced by isogrids.

All those elements should be placed in a millimetric precise configuration, which should be proven to exist first of all, compatibly with an isogrid geometry that increases the stresses resistance of the cylinder base. This definitely means that a way more complex design should be evaluated, in order to make everything fit between the radii of the isogrid, but considering that 40 $mm$ of height it's still not enough to reach a tolerable level of stresses on the bases, this value should also be increased, with its relative encumbrance increase. For this reason a more detailed analysis should be carried on in order to implement this solution in the actual propulsion system design but, probably, the high encumbrance linked to it would make it incompatible anyway.
Finally, the third solution provides for implementing other possible materials and geometries for the whole tank. Between the eligible materials, the most promising one is for sure Ergal, which is the trade name of an Aluminium alloy of the 7000 series, characterized by excellent mechanical strength (the best among all conventional aluminium alloys) but greater susceptibility to corrosive agents, due to the presence of Zinc. This last characteristic is the main reason why this Aluminium alloy was first discarded, because it would make it incompatible with the Hydrogen Peroxide in terms of long time storage. However, in order to reduce its sensibility to stress corrosion cracking, specific "stabilizing" treatments with the addition of Chrome were developed, otherwise anodizing treatments could be analyzed, giving to Ergal an even higher mechanical strength and making it more resistant to corrosion. If none of these treatments would make it exploitable for a long time storage of Hydrogen Peroxide, as a last choice, it will be possible to entirely cover the

inside surfaces of the propellant tank.

|  | AISI 316 stainless steel | Ergal 7075 |
|---|---|---|
| Yield stress [$M$Pa] | 290 | 700 |
| Density [$\mathrm{kg\,m^{-3}}$] | 8000 | 2880 |

**Table 3.2:** Materials properties comparison.

According to the simulations, using Ergal 7075 would almost automatically solve the problem with stress at the center of the bases, corresponding to the local maximum in Fig.3.4, but the one at the edges would slightly remain. In order to make the whole tank compatible with the internal pressure, it would be enough to increase the curvature radius on the edges, from 10 $mm$ to 15 $mm$, and add a reinforcement disc at the center of the bases with 30 $mm$ of radius and 2 $mm$ of thickness. This way even on the most stressed spot of the tank there will still be a factor of safety of at least 2 in respect to the yield stress of Ergal 7075. The tank design if this solution is approached can be seen in Fig.3.8.

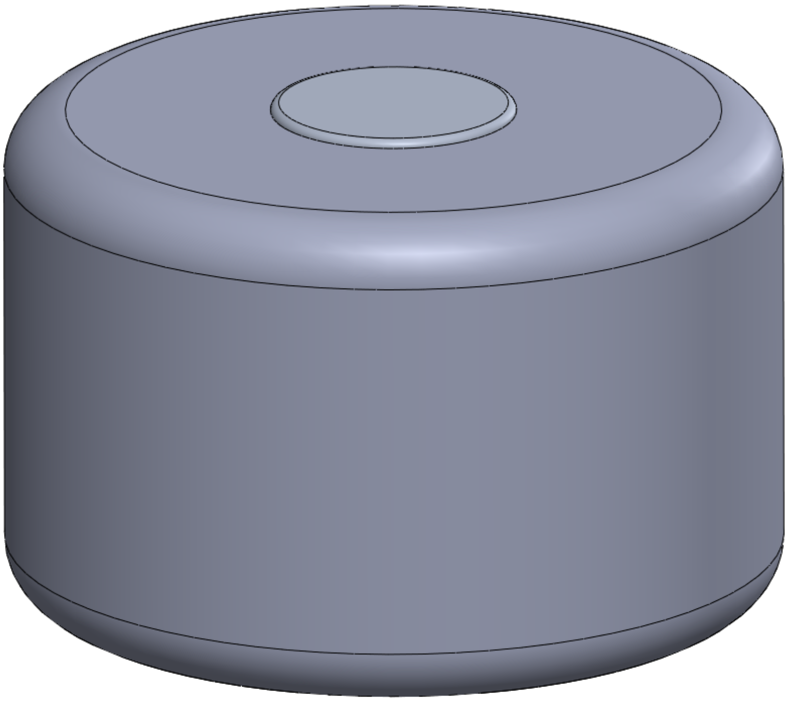

**Figure 3.8:** Design of the propellant tank if made of Ergal 7075, with 15 $mm$ radii of curvature on the edges and disc reinforcements on the bases.

Analyzing the pro e cons of each solution, the first one would be better of the third one because the material would be compatible with long time storage of Hydrogen Peroxide, furthermore it would occupy less volume than the second solution, but much more than the third one and the mass increase is way more relevant. The second solution has some potential but a much more complex study has to be carried on in order to verify if the pros overcome the cons, because between all the alternatives it is for sure the one that encumber more. Finally, the third solution is the best one in terms of encumbrance and mass, the only con is that a further study on the long time storage problem should be carried on, even if this should not represent a problem because, if the Chrome treatment or the anodization are not sufficient to overcome the corrosion problem, it would be enough to film the inner surfaces with a thin layer of Teflon.

For these reasons the final design for the propellant tank will be the one presented with the third solution, a classical cylindrical propellant tank with reinforced bases, entirely made of Ergal 7075, with curvature radii on the edges of 15 $mm$.

### 3.1.2 Two pieces propellant tank

For construction reasons, it is preferable to do not build the tank as a single peace of Ergal, as it will be necessary to insert a mechanical element that will separate the pressurant from the propellant, avoiding mixing and preventing Nitrogen from entering the fuel pipe line, that would cause variations in terms of chamber pressure, fumes products, thrust and potentially mission fail. Furthermore it will be very useful in order to prevent sloshing of the fuel, because with the decrease of the level of the hydrogen peroxide in the tank, also this separation element will be pushed down by the pressurant, leaving no available volumes where the liquid could move causing variations of the center of gravity of the drone, resulting in thrust misalignment.

The concept behind this separation element is a piston like mechanism: a disc parallel to the bases will be inserted in the tank and sealed with a proper gasket, allowing no leakage, capable to slide from its initial position, adjacent to the upper base, and moving vertically towards the lower base thanks to the reciprocating seal. Once needed, the pressurant will flow from the pressurant tank to the propellant tank, with a constant volumetric flow rate equals to the one required by the main engine plus attitude control systems, it will enter the tank from its upper base, pushing down the piston-like disc which in turn will push out fuel that will flow through its fluidic line ending in the combustion chamber.

In order to insert this disc inside the tank, it would be much easier if the vessel were made by two different pieces: a container and its cover.

The container will just be a classical cylinder shaped tank, just like the the one proposed for the final design in section 3.1.1, but missing the upper base, while the cover will be "U" shaped so that it could be inscribed inside the container with some millimeters of play where to place the sealing O-ring in a "c" shaped gasket.

Regarding the design of the separation element, from a private call with a T4i[2] expert, it has been decided to make it a disc 1 $mm$ thick, made of Teflon. However, since during the filling pre flight procedures it is supposed to create vacuum alternatively in both the propellant and pressurant fluidic lines, as will be shown in Chapter 4, it must be ensured that when the separation disc will be touching the cover, it must not support any structural load, just like when it will be touching the lower base. This means that in the exact same time when the reciprocating gasket reach one of the two possible ending configuration, the whole disc must also be in contact with the solid element of the tank, whether it is the cap or the lower base. In order to do so, a more complex design for the separation element have been thought: since the bottom edges have an internal radius of curvature of 15 $mm$, this means that the gasket would end its stroke when the flat disk is still 15 $mm$ far from the bottom surface, for this reason the Teflon separation element should have a design which follows the curvature of the base of the tank, just like it's shown in Fig.3.9.

---

[2] "T4i, Technology for Propulsion and Innovation"

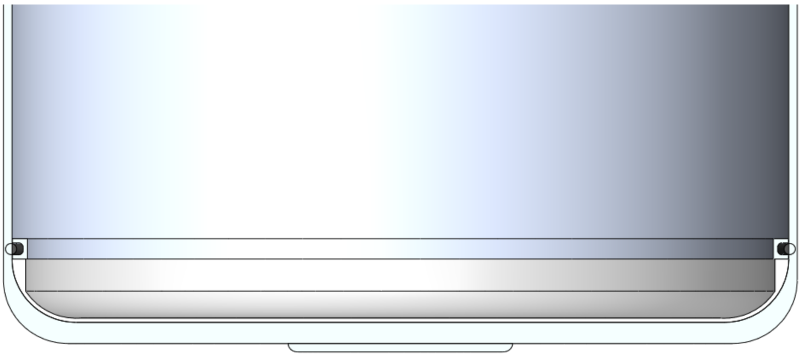

**Figure 3.9:** Teflon separation element bottom end configuration where the design of the disk follows the curvature of the tank.

Using this geometry for the separation element, also the cover must be designed to make sure that when the reciprocating seal of the Teflon piston reaches the gasket of the static seal of the cap, the whole Teflon surface will be in contact with the Ergal cover, just like it is shown in Fig.3.10, so that the thin layer of Teflon should not carry any structural load. Moreover, as an additional level of security, it should be considered that the separation element could be structurally weakened in correspondence of the pressurant inlet. This way, if the Hydrogen Peroxide decomposition exceeds the pressurant ullage relief capacity, when the Teflon element will be touching the tank cap, it will break at the level of the inlet, causing the leakage of propellant instead of the explosion of the tank.

**Figure 3.10:** Teflon separation element top end configuration where the design of the cap follows the curvature of the piston.

Furthermore, during the operative period, when the separation element is not in any of those two specific configurations, the differential pressure between the upper and lower face is minimal, less than 0.1 *bar*, this means that, according to the T4i expert, 1 *mm* of thickness is enough to handle the stresses acting on the Teflon element.
For what concern the two different types of sealing that should be included in this type of design, the one between the cap and the lateral surface of the tank is a static seal, while the one between the piston separation element and the tank is a reciprocating seal.
In a truly static seal, the mating gland parts are not subject to relative movement (except for small thermal expansion or separation by fluid pressure). This will be obtained fixing the cap to the tank by means of screws. The exact number of screws and their disposition however must be carefully analyzed, because to many would weaken the tank while too few would not withstand the inside pressure.

Instead, in a reciprocating seal[3], there is relative reciprocating motion (along the shaft axis) between the inner and outer elements. This motion tends to slide or roll the O-ring back and forth with the reciprocal motion.

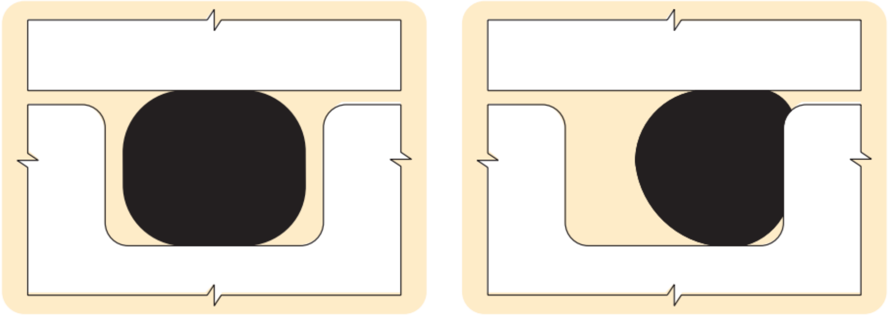

**Figure 3.11:** O-ring installed (left) and under pressure (right).

A classical O-ring seal can be seen in Fig.3.11, where on the left its represented the O-ring as installed, before the application of pressure, while on the right it's shown the application of fluid pressure on the O-ring, where it has been forced to flow up to, but not into, the narrow gap between the mating surfaces and in so doing, has gained greater area and force of sealing contact.

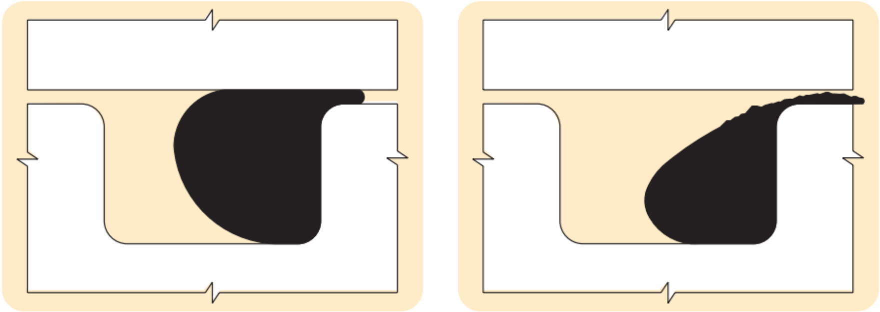

**Figure 3.12:** O-ring extruding (left) and extrusion failure (right).

In Fig.3.12 instead, it's shown on the left the O-ring at its pressure limit, with a small portion of the seal material entering the gap between inner and outer members of the gland, while on the right are illustrated the results of further increasing pressure and the resulting extrusion failure.
For what regards the choice of the actual O-ring, it has been chosen from the Parker catalogue[16] Parker Series 2-168, because of its compatibility with the dimensions of the propellant tank, since its inner diameter is 183.82 $mm$ and its width is 2.62 $mm$.
For what concerns the choice of the O-rings material, it was evaluated that the actual best material would be Fluorocarbon FKM, since it is considered "satisfactory" if used with Hydrogen Peroxide propellant and Nitrogen pressurant.
Once the O-Rings have been chosen, a proper design for the gasket housings can be easily achieved. As can be seen in Fig.3.13, each gasket housing has been shaped like a "c", build entirely with Ergal 7075 for the cap seal, because it must be able to stand the internal

---

[3] "According to the Parker O-Ring Handbook[16], O-ring seals are generally not recommended for reciprocating installations in which the speed is less than one foot per minute, it could be necessary to analyze if this represent a problem by contacting a Parker Territory Sales Manager for more information on special seals."

pressure stresses, while the piston one will be made of Teflon and build as a single piece with the separation element, since it will never have to bear any relevant stress. Its precise dimensions are shown in Annex E.

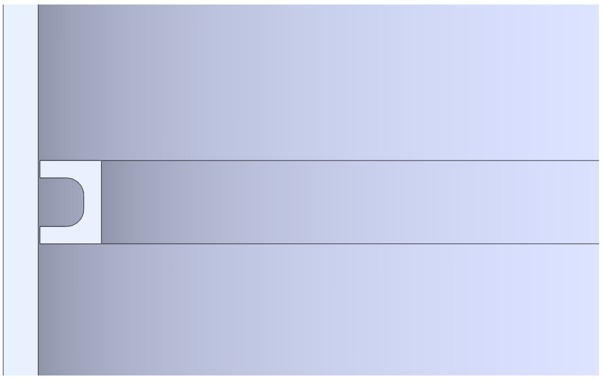

**Figure 3.13:** Gasket housing for the O-Rings.

## 3.2 Final propellant tank design

In conclusion, a sectional view of the final design for the propellant tank can be seen in detail in Fig.3.14. Starting from the bottom to the top, there is the Ergal 7075 cylinder shaped container, with a 2 *mm* thick reinforcement disc of 30 *mm* radius at the center of the base, then the Teflon piston-like separation element, which follows the 15 *mm* inner curvature radius of the edges of the tank, coupled with its O-ring reciprocating seal and gasket. Finally the "U" shaped reinforced Ergal 7075 cap, which again follows the same curvature of the piston, and its O-ring static seal whit gasket which, unlike the piston one, is made by the same material of the tank, since it has to bear the stresses related to the 18 *bar* internal pressure.

**Figure 3.14:** Sectional view of the final design for the propellant tank.

Again, all the dimensions of each component are shown in detail in Annex E.

# Chapter 4

# Fluidic line design

In this chapter, will be analyzed how the fluidic line could be modified from the previous design[1], understanding if each valve is really necessary and eliminating from the scheme the unnecessary ones, obtaining a final fluidic line design. After that, a product for each component, which must be compatible with the propulsion system requirements, is chosen from a professional seller. Once the fluidic line is fully defined, a pressure drop analysis can be carried on in order to calculate, starting from the required pressure in the combustion chamber, what will the propellant tank pressure be.

## 4.1 Fluidic line scheme

As already mentioned in Chapter 1, a preliminary fluidic line scheme has already been obtained in [17], in collaboration with a T4i expert. A schematic representation of how the pressure regulated propulsion system was planned to be can be seen in Fig.1.6 however, since the propulsion system has changed a lot with respect to how it was at the beginning of this study, many fluidic elements should be changed or even removed.
Since the propellant tank, with the actual design, has a physical element which prevents the pressurant from coming in contact with the propellant, the pressurant portion of the fluidic line can be rearranged and simplified.
According to the T4i expert, having this piston-like element separating the propellant and the pressurant cancels the failure risk linked to isentropic compression of the pressurant, entering the propellant tank at the first pressurization. When it's not pressurized, the propellant tank pressure would be around 1 *bar*, at the first pressurization, the pressurant will enter the tank at a pressure of 18 *bar*, this almost instantaneous isentropic compression would lead to an increase in temperature of the gas, meaning that an hot gas would be in direct contact with the Hydrogen Peroxide, risking to cause an explosion. Having the piston-like element separating the gas from the liquid resolve this problem.
This means that there is no more need for the pipe section with the *Bypass valve* and the *Orifice*, parallel to the main pipe with the *Pressure valve*, which the only purpose was the first pressurization of the fluidic line reducing the inlet pressurant pressure in the propellant tank. Now, according to the T4i expert, working with a *Pressure regulator* similar to the ones that they already use in many of their projects, there would be no need for a valve downstream of the regulator, like the *Check valve* in the scheme, in order to be able to make vacuum downstream of the *Pressure regulator*. Finally, since the *Pressure valve* is upstream of the regulator and it is designed for pressures of 350 *bar*, adding in line also a *Filling latch valve* would be a redundancy.
For what concerns the propellant fluidic line, it has almost remained unchanged, the only

---

[1] "The one devised by Gabriele Podestà in his thesis[17]."

simplifications have been the removal of the *Rupture disk* and the *Pressure relief*, since for safety reasons is not acceptable to pour any amount of Hydrogen Peroxide into the space vector during the transport procedures.
The new resultant fluidic line scheme could be represented by Fig.4.1.

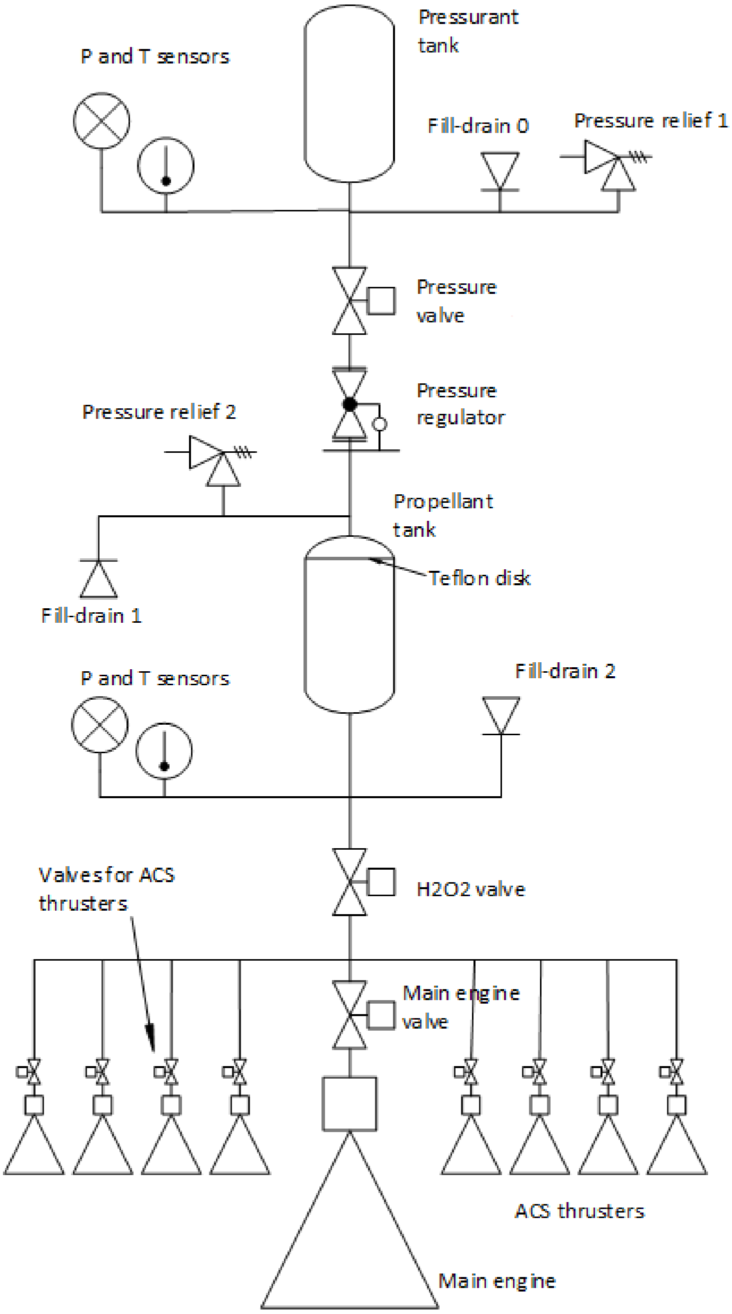

**Figure 4.1:** New fluidic line scheme.

## 4.2 Filling procedures

The most critical aspect of the fluidic line filling procedures is for sure the Hydrogen Peroxide tank filling.
Hydrogen Peroxide is not flammable, so the hazard of static charge build-up, due to droplet

free-fall from a top discharge fill line is minimal. Nevertheless, it is often advisable to have the fill line extend below the liquid surface. Usually, the more common hazard is an “explosive” pressure rupture due to a gas generation rate exceeding the vent capacity of a container. Catalytic decomposition results in the liberation of oxygen and heat. In concentration above 65%, a catalytic decomposition can become self-accelerating because the rate of heat evolution exceeds the rate of heat loss to the surroundings. In our case study, the fill line itself come from under the propellant tank so that there would be no risks due to droplet free-fall, however, since the Hydrogen Peroxide concentration is 90% and the container is a propellant tank without a dedicate ventilation system, it is much preferable to insert the propellant in the most delicate way possible, meaning not to pump it into the tank but suck it in by creating vacuum in the line, as will be shown in Fig.4.3.
The first step of the tanks filling procedures is the pressurant tank filling, that can be seen in Fig.4.2.

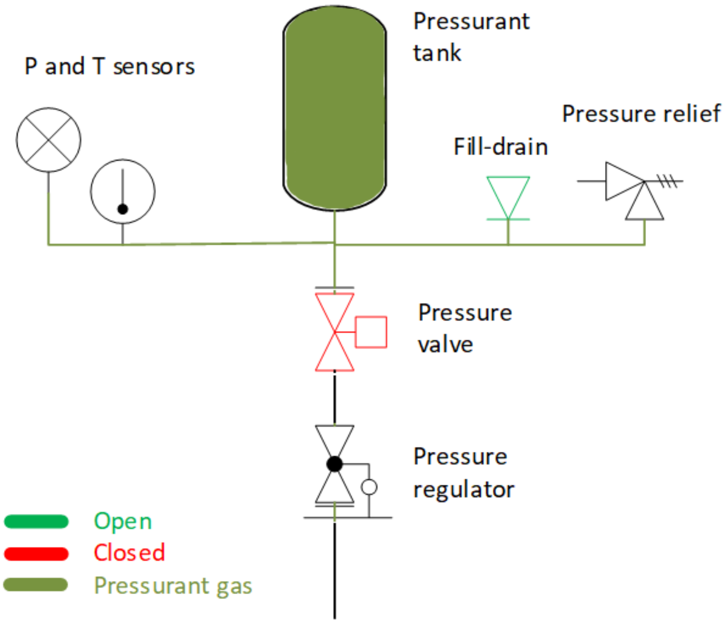

**Figure 4.2:** Pressurant filling procedure scheme.

First of all it must be created vacuum in the fluidic line through the *Fill drain valve*, and in order to achieve it the pressure valve will have to remain closed (it is a normally closed valve). As the *Fill drain*, that is a check valve, is a passive component, it should be opened and kept open with a custom tool, this instrument is an element that will be connected to the valve ensuring a sealing (e.g. threaded joint with o-ring) and will have a pin that entering the valve keeps it open.
That being said, the pressurant filling procedure could be summarized as follows:

1. Connect the custom tool (which in turn is connected to a vacuum pump) to the *Fill drain* and create vacuum in the line (up to the Pressure valve).
2. Close the valve (by pulling back the pin of the custom tool) and connect the tool to a Nitrogen pressurant tank. The valve is then reopened (advancing the pin of the tool) and the pressurant gas system is filled up until reaching the nominal pressure, which is 350 $bar$.

3. Close the valve by pulling back the pin, disconnect the custom tool and close the check valve with a cap (same interface of the tool for what concerns the connection to the valve) so as to have an additional barrier to reduce the leakage rate.

This way the fluidic line going from the pressurant tank to the *Pressure valve* will be filled with Nitrogen, while the rest of the line will still have air inside, as shown in Fig.4.2. For what concerns the propellant filling procedure, which is completely described in Fig.4.3, the process is a little more complex.

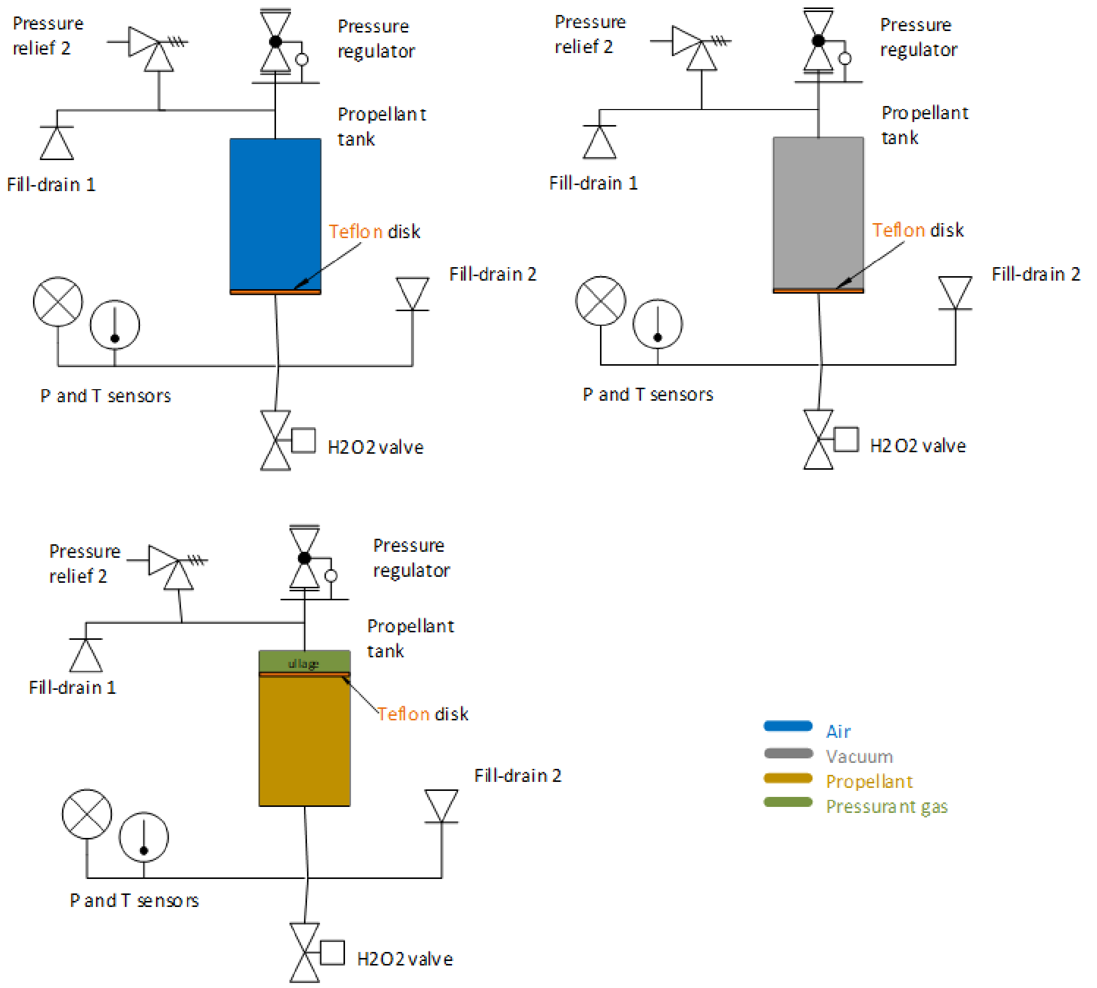

**Figure 4.3:** Propellant filling procedure scheme.

As already said before, the Hydrogen Peroxide should be sucked inside the tank and not pumped into it. In order to achieve this, considering the actual design of the propellant tank that is divided in two parts by the Teflon piston, a few more step are required:

1. Connect the custom tool (which in turn is connected to a vacuum pump) to the *Fill drain* 2 and vacuum the line enclosed between the *Teflon disk* and the *Fill drain* 2. This process will bring the Teflon piston to coincide to the lower face of the tank, this means that the pressure must be reduced gradually to make this process happen as "gently" as possible in order to avoid any structural load on the piston.

2. Close the *Fill drain* 2 valve (by pulling back the pin of the custom tool) and connect the tool to an external tank containing Hydrogen Peroxide at the pressure of

1 *bar*. At this point, maintaining closed the *Fill drain* 2, the *Fill drain* 1 is connected to a vacuum pump which will vacuum the line between the *Fill drain* 1, the *Pressure valve* and the *Teflon disk*, without reaching the same vacuum level the piston will not move from its position.

3. The *Fill drain* 2 is gradually reopened, sucking the propellant inside the fluidic line and inside the tank, letting the Teflon disc slowly go towards the top of the tank. Once the established amount of Hydrogen Peroxide has been stored in the tank, the *Fill drain* 2 can be closed.
4. Connect the *Fill drain* 1 to an external tank of Nitrogen, this way the remaining free volume of the tank and the pressurant fluidic line can be filled with pressurant, creating the ullage volume inside the tank and eliminating the vacuum from all the fluidic line.

## 4.3 Components selection

At this point, a definitive fluidic scheme has been defined and it is possible to proceed with the identification of a possible product to buy on the market for each component.
Since most of the identified valves would be produced by *The Lee Company*[2], it will be useful to know that they developed the a new way to define and measure resistance to fluid flow, the Lohm laws. Just as the "Ohm" defines electrical resistance, the "Lohm" or "liquid Ohm" can be used as a measure of fluid resistance. The Lohm is defined such that 1 *Lohm* will flow 100 *gpm* of water with a pressure drop of 25 *psi* at a temperature of 80° *F*. Since resistance is inversely proportional to flow, by definition:

$$\text{Lohms} \;=\; \frac{100}{\text{flow} \;\; (\text{gal/min } H_2O \text{ @ 25psid})} \tag{4.1}$$

1,000 Lohms will flow 0.1GPM (378.5 mL/min. )

378,500 Lohms will flow 1 mL/min.

An advantage of using Lohms is that one can specify performance without concern for coefficients for discharge, physical dimensions, passageway geometry or tolerances, the resistance of any flow can be expressed in Lohms.

Since Eqn.4.1 is referred to water, it is possible to extend the use of the Lohm laws to many different liquids.
The following formulas introduce compensation factors for liquid density and viscosity, furthermore the units constant $K$ eliminates the need to convert pressure and flow parameters to special units. They are applicable to any liquid of known properties, with minimum restrictions on pressure levels or temperature.

Volumetric Flow Units:

$$L = \frac{KV}{I}\sqrt{\frac{H}{S}} \tag{4.2}$$

Gravimetric Flow Units:

$$L = \frac{KV}{w_f}\sqrt{HS} \tag{4.3}$$

Where:
$L$ = Lohm rate (Lohms)

---

[2] "One of the leading companies in the field of miniature components for fluid control"

$H$ = Differential pressure
$I$ = Liquid flow rate: Volumetric
$S$ = Specific gravity
$V$ = Viscosity compensation factor
$w_f$ = Liquid flow rate: Gravimetric
$K$ = Units Constant

For this case study, the liquid taken into account was the Hydrogen Peroxide 90% concentration. Since its viscosity is really similar to the water one, there is no need for a viscosity compensation factor ($V$) and its value can be considered 1. The other useful parameters are shown in table 4.1 where the Unit constant $K$ depends on the units of volumetric flow ($L/min$) and of pressure ($bar$) used in the formulas.

| | Hydrogen Peroxide 90% |
|---|---|
| Viscosity compensation factor ($V$) | 1 |
| Specific gravity ($S$) | 1.392 (4/20°$C$) |
| Units constant ($K$) | 288 |

**Table 4.1:** Hydrogen Peroxide parameters useful for the Lohms calculation.

A very similar process can be done to extend the Lohm laws to any gas. The following formulas work well for all gases because they are corrected for the specific gas and for the flow conditions caused by the compressibility of gases due to pressure.

$$\mathrm{L} = \frac{\mathrm{K f_T P_1}}{\mathrm{Q}} \tag{4.4}$$

(Sonic condition) i.e. $\mathrm{P_1/P_2} \geq 1.9$

$$\mathrm{L} = \frac{2\ \mathrm{K f_T}\sqrt{\Delta \mathrm{P P_2}}}{\mathrm{Q}} \tag{4.5}$$

(Subsonic condition) i.e. $\mathrm{P_1/P_2} < 1.9$

Where:
$L$ = Lohm rate (Lohms)
$K$ = Units Constant – Gas
$f_T$ = Temperature correction factor
$P_1$ = Upstream absolute pressure
$P_2$ = Downstream absolute pressure
$Q$ = Gas flow rate
$\Delta P = P_1 - P_2$

Thanks in particular to Eqn.4.2 and 4.5, it was possible to identify from the Lee catalogue a product for each component needed by the fluidic line, paying attention that each one could work under this specific mission requirements of pressures, flows, leakage rates and dimensions. The chosen components are shown in table 4.3.

| Pressurant | | |
|---|---|---|
| | Lohm rate | Serial number |
| Pressure relief | 1500 | PHFA2815570D |
| Fill-Drain | 180 | CSFA2506005A |
| Pressure valve | 2800 | SDBB2122203A |
| To vacuum | 180 | CSFA2506005A |
| Propellant | | |
| | Lohm rate | Serial number |
| Fill-Drain | 180 | CSFA2506005A |
| H2O2 valve | 3500 | SDPB3321013A |
| Main engine valve | 200 | SDHB3321012A |
| ACS valves | 4100 | IEP Series |

**Table 4.2:** Hydrogen Peroxide parameters useful for the Lohms calculation.

For what concerns the pressure sensor and temperature sensor were chosen respectively Keller's[11] 6LHP Series and Amphenol's[2] JS8741, while for the moment the pressure regulator is still on a to be determined phase, it could be used TESCOM's[6] BB1 Series Pressure Regulator OEM or it could be made ad hoc[3] for our purpose.
Since each component has been chosen, a seller of Lee was contacted to confirm the selection. It turned out that the two solenoidal valves of the propellant fluidic line are not compatible with the operative conditions in terms of volumetric flow and, between their available valves, there are no substitute valves to choose so that the only possibility is to make a custom valve both for the *H2O2 valve* and the *Main engine valve.* For this reason the pressure drop calculation is still at an indicative level, since there are no precise information about the Lohm rate and dimensions of these valves.

## 4.4 Pressure drop

Since the propellant has to flow inside tubes and pass obstacles (valves) various dissipative effects will actually make the pressure decrease from the propellant tank value. In order to evaluate how much pressure the propellant will lose, it is possible to differentiate the drops in distributed and concentrated. As the names suggest, distributed pressure drops will be considered to occur in a finite space (the length of a tube, for example), while the concentrated ones in an localized space (valves). This is acceptable as a first approximation and gives a first estimate about what the pressure must be inside the propellant tank to ensure a correct feed to the engine.
As already evaluated by Gabriele Podestà[17], the distributed pressure drops can be considered as around 0.14 *bar* per meter of tube, while in order to calculate the concentrated pressure drops, it is possible to use the Lohm laws set out in Section 4.3.
Using Eqn.4.2 for the propellant valves pressure drops and Eqn.4.5 for the pressurant valves pressure drops, it is possible to obtain respectively $H$ and $\Delta P$. At this point, knowing the operative pressure of the main engine (10 *bar*), it is possible to perform a backward calculation, through the catalytic bed and valves, and find the pressure upstream of each component of the propellant fluidic line up to the propellant tank.
As already said, this calculation is still just an approximation because the *H2O2 valve* and the *Main engine valve* are still to be determined, but for these calculations will be used the the same solenoidal valve chosen for the *Main engine valve* shown in table 4.3 for both the propellant solenoidal valves.

---

[3] "In collaboration with Polytechnic University of Turin."

The calculated pressure drop of each valve is shown in table 4.3.

| Pressurant | Pressure drop [$bar$] |
|---|---|
| Pressure valve | 0.00069 |
| Propellant | Pressure drop [$bar$] |
| H2O2 valve | 1.32 |
| Main engine valve | 1.32 |
| ACS valves | 0.25 |

**Table 4.3:** Hydrogen Peroxide parameters useful for the Lohms calculation.

From a private call with a T4i expert, the catalytic bed dimensions and pressure drop have been assigned on the basis of previous experiences and heritage, in particular it will have a 30 $mm$ diameter, 60 $mm$ length and it will cause around 5 $bar$ of pressure drop.
With that been said, an estimated propellant tank operative pressure of around 18 $bar$ could be plausible.
At this point, the new design of the propulsion system needs a defined arrangement for all elements of the fluidic line, starting from the pressurant tank all the way to the combustion chamber, passing through valves, sensors, tubes and catalytic bed.
Considering the dimensions, taken from the Lee catalogue, of each element of the fluidic line considered in table 4.3, a new layout for the fluidic line has been designed as shown in Fig.4.4, 4.5 and 4.6.

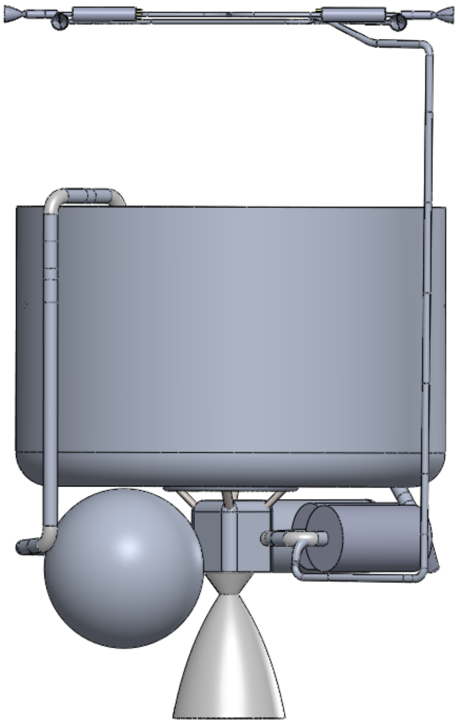

**Figure 4.4:** Propulsion system lateral view.

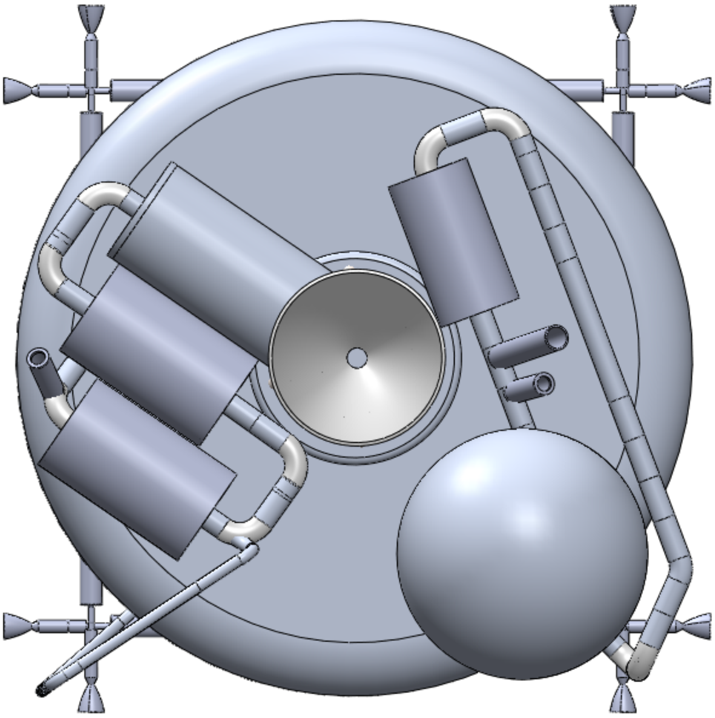

**Figure 4.5:** Propulsion system down view.

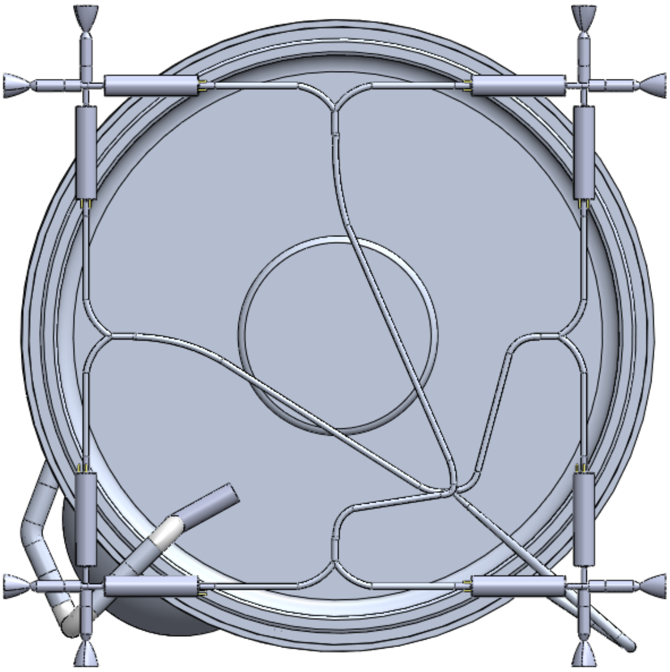

**Figure 4.6:** Propulsion system top view.

Where all the valves have been simplified as cylinders with the only purpose to obtain a quantitative model of the encumbrances.

In particular in Fig.4.5 on the left can be seen the propellant fluidic line, consisting of the catalytic bed, the main engine valve the H2O2 valve, the fill drain valve and the eight ACS solenoidal valves, while on the right its shown the pressurant tank, the pressure reliefs, the first fill drain valve, the pressure valve and the second fill drain valve (this last one can be seen better in Fig.4.6). The purpose of the serpentine like tubes in the pressurant branch of the fluidic line is to host the *Pressure regulator* on its free parts, downstream of the *Pressure valve*.

Again, the main engine valve and the H2O2 valve represented in Fig.4.5 are just an approximation based on the preliminary choice that then turned out not compatible.

# Chapter 5

# Nozzle optimization

Since the LuNaDrone is supposed to work on the Moon, where there is no atmosphere, its propulsion system could be compared to a "vacuum" engine, like a rocket engine for upper stages.
This kind of engines are supposed to work in vacuum, meaning ambient pressure equal zero, where the thrust coefficient $C_f$ loses its dependence from the chamber pressure, as can be seen in Eqn.5.1.

$$C_f = \sqrt{\frac{2k^2}{k-1}\left(\frac{2}{k+1}\right)^{\frac{k+1}{k-1}}\left[1-\left(\frac{P_e}{P_0}\right)^{\frac{k-1}{k}}\right]} + \frac{(P_e - P_a)\,A_e}{P_0 A^*} \tag{5.1}$$

Where $P_0$ is the chamber pressure, $P_e$ is the exit section pressure, $P_a$ is the ambient pressure, $A_e$ is the exit area, $A^*$ is the critic area and $k$ is the specific heat ratio.
Representing on a graphic the relations between the thrust coefficient $C_f$ and the expansion ratio $\epsilon$, the upper curve is the one corresponding to a vacuum thruster, therefor it can be seen in Fig.5.1 that the bigger the expansion ratio is, the higher the thrust coefficient will be, reaching the maximum value of 2.246 .

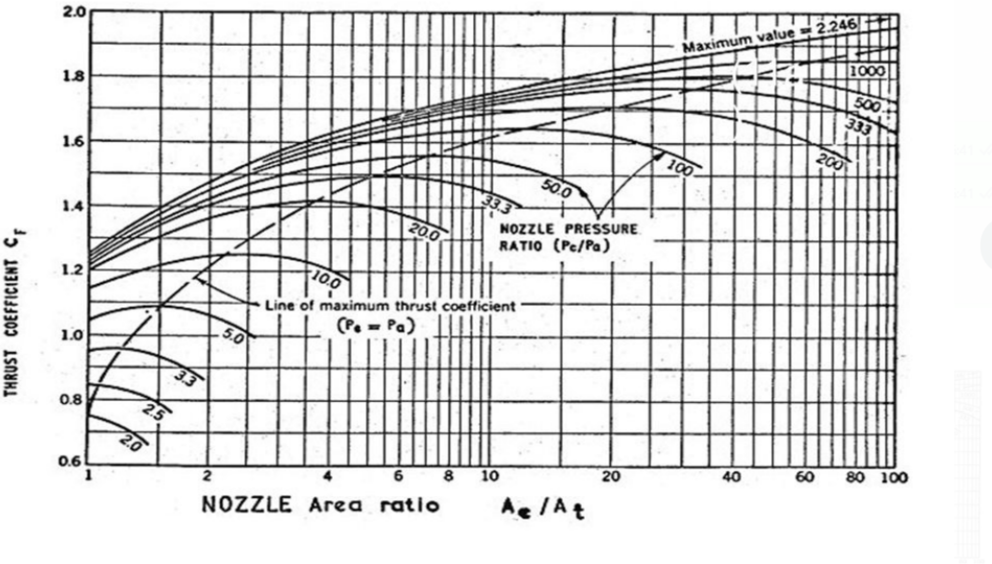

**Figure 5.1:** Thrust coefficient $C_f$ versus expansion ratio $\epsilon$, which is the ratio between the exit area $A_e$ and the throat area $A_t$.

For these reasons an upper stage rocket engine usually works at very high expansion ratios,

often also exploiting nozzle extensions, because having a high $C_f$ would lead to a higher $Isp$, that could be summarized as a lower mass flow rate for equal thrust.
For what concerns the LuNaDrone, this logic is also valid, but it should also be considered that it has to provide a relatively low thrust and one of the most critical requirement is the volume encumbrance of the drone. In fact, having a bigger expansion ratio will lead to have a higher nozzle length, which must be carefully analyzed in the perspective of advantages and disadvantages.
Having a shorter nozzle could mean that the propulsion system could be much more compacted near the bottom of the drone, leaving empty volumes on top that could be used for storing more propellant, giving the opportunity to spend more time in hovering or even do more trips in the lunar lava tubes. In the other hand, having a nozzle with a lower expansion ratio would lead to a bigger mass flow rate for equal thrust.
The actual design of the drone provides for certain elements to be put below the propellant tank, such as a Lidar Range Finder pointing perpendicularly under the drone and the various elements of the fluidic line. Between all these components the the most cumbersome and limiting element is the pressurant tank, which makes it impossible for the propellant tank to lower further, leaving the possibility for the nozzle to decrease its length up to a minimum value of 32.65 $mm$.

## 5.1 Performance analysis

Through a Matlab code which purpose was to analyze the increase in storable propellant mass, resulting from the decrease in nozzle length, it can be see that an expansion ratio of 17 is linked to a nozzle length of 33.6 $mm$, which is the minimum acceptable value. Decreasing the nozzle length more than this would not bring any advantage in terms of propellant tank height increase, because the bulkiest element below it would become the pressurant tank.
This code works by imposing the required thrust of 50 $N$, making the expansion ratio vary between 10 and 70, calculating for each step the corresponding values of $C_f$, $Isp$, mass flow rate, throat area and exit area, and finally the calculating the new bell nozzle length, the corresponding new dimensions of the tank (assumed as a cylinder) and the new storable propellant mass.

Specific impulse:

$$I_{sp} = \frac{c}{g_0} = \frac{c^* C_F}{g_0} \tag{5.2}$$

Mass flow rate:

$$T = \dot{m}c = \dot{m} I_{sp} g_0 \rightarrow \dot{m} = \frac{T}{I_{sp} g_0} \tag{5.3}$$

Throat diameter:

$$c^* = \frac{p_c A_t}{\dot{m}} \rightarrow A_t = \frac{c^* \dot{m}}{p_c} \rightarrow D_t = \sqrt{4A_t/\pi} \tag{5.4}$$

Exit section diameter:

$$A_e = \varepsilon A_t \rightarrow D_e = \sqrt{4A_e/\pi} \tag{5.5}$$

For each step of the simulation, after the calculation of the new $C_f$ corresponding to the actual expansion ratio through Eqn.5.1, it is possible to proceed to determinate the new value for the $Isp$, mass flow, throat area and exit area, through the Eqn.5.2, 5.3, 5.4 and 5.5.

At this point, knowing the throat and exit nozzle dimensions, it is possible to determine the conical nozzle equivalent length through the formula in Fig.5.2 for $L_{cone}$, the equivalent length of a conical nozzle with 15° semi-opening angle, then the corresponding bell nozzle length through Eqn.5.6.

$$L_{bell} = 0.7 L_{cone} \tag{5.6}$$

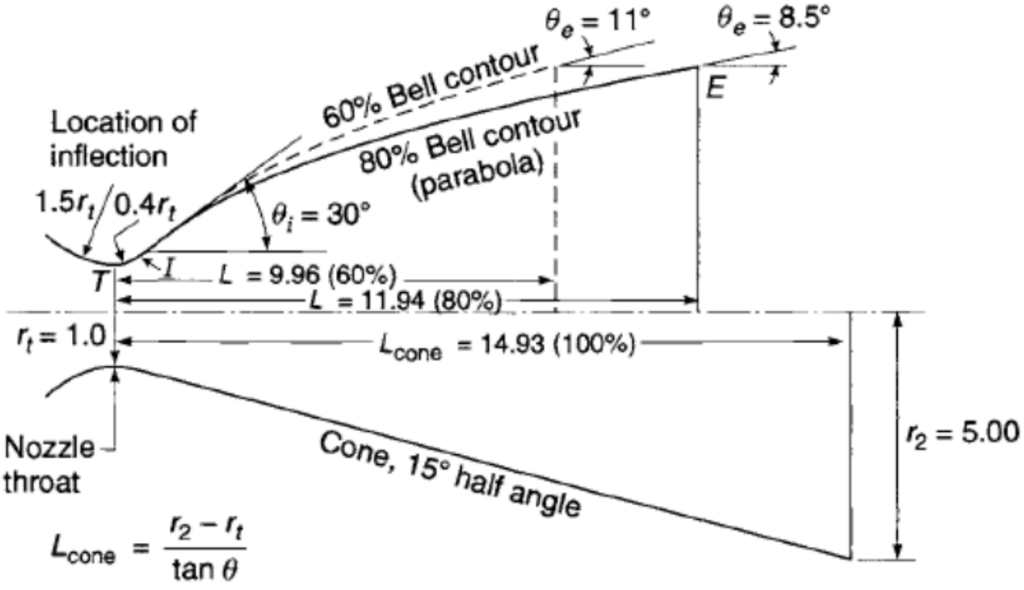

**Figure 5.2:** Comparison between a conical and a bell nozzle.

Finally, knowing the bell nozzle length and the convergent conical part, it is possible to calculate the length of the whole nozzle and thus the corresponding increase in propellant tank height, meaning a new available volume for storing more Hydrogen peroxide.
The various relationships between these quantities and the expansion ratio are shown in Fig.C.1 and C.2, where choosing 17 as the expansion ratio value, it can be seen that this is not the best choice in terms of $Isp$ but it will lead to a propellant mass increase of the 33.5%, starting from 3.94 $kg$ and reaching 5.26 $kg$.

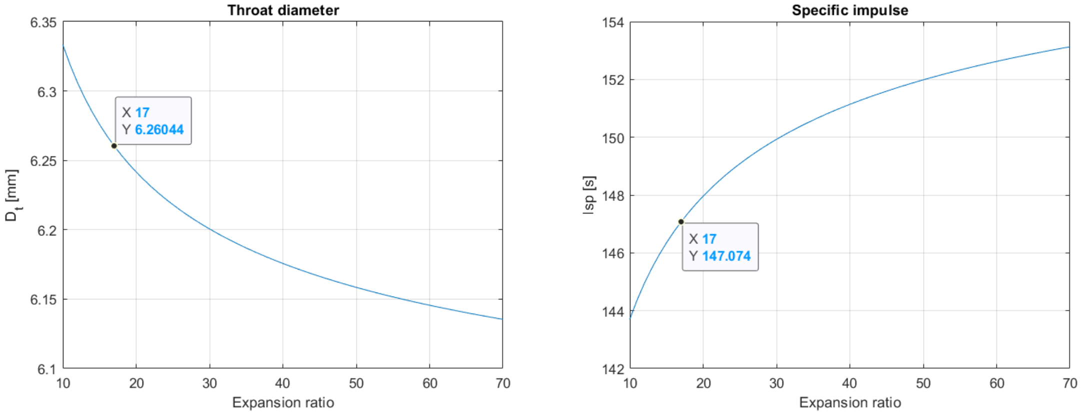

**Figure 5.3:** On the left is shown the relationship between the throat diameter and the expansion ratio while on the right the one between the specific impulse and the expansion ratio.

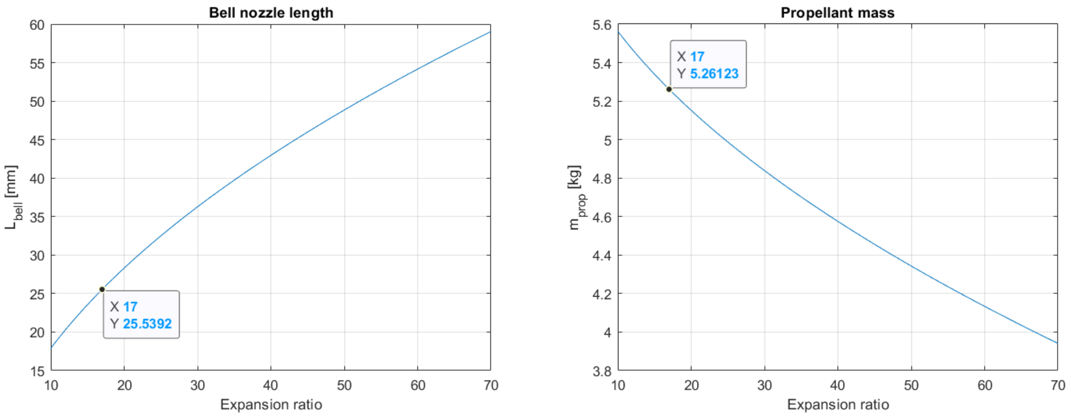

**Figure 5.4:** On the left is shown the relationship between the bell nozzle length and the expansion ratio while on the right the one between the propellant mass and the expansion ratio.

For what concerns the increase in terms of mass flow rate, resulting from the lower $Isp$ (which in turn is resulting from the lower expansion ratio), choosing to have a 17 expansion ratio on the bell nozzle starting from 70 leads to an increase of the 4.12%, starting from a 0.0332846 $kg\ s^{-1}$ mass flow rate and reaching 0.0346549 $kg\ s^{-1}$, as can be seen in Fig.5.5.

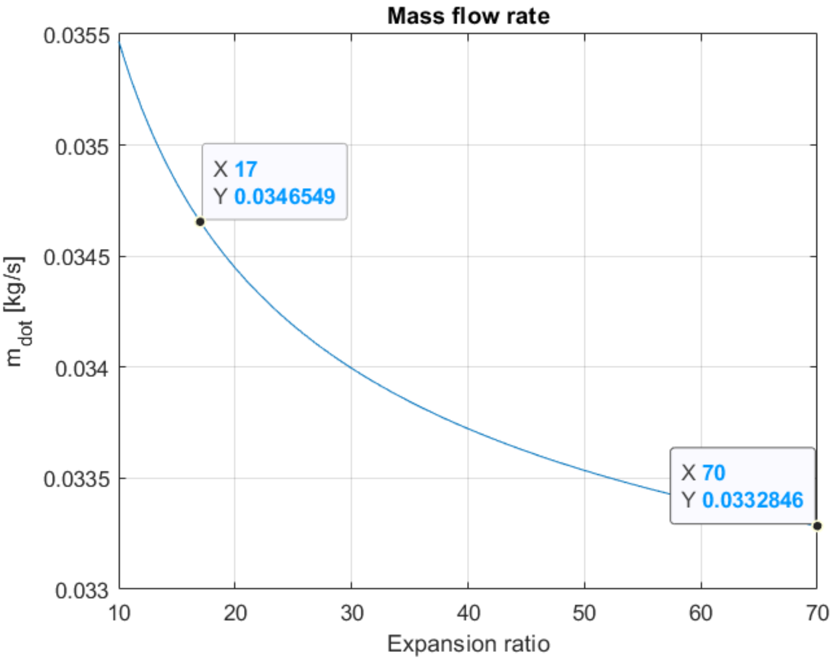

**Figure 5.5:** Relationship between the mass flow rate and the expansion ratio of the bell nozzle.

This means that choosing to work with a bell nozzle with 17 of expansion ratio instead of 70 would mean that per each second of firing of the main engine, it would need 0.0013703 $kg$ of hydrogen Peroxide more. Considering that the total expected burning time will be less than 3 minutes, this would mean that the main engine would consume at most 0.246654 $kg$ more than of how much it would in the configuration with 70 of expansion ratio.
In conclusion choosing to work with a bell nozzle of 17 of expansion ratio would make it possible to carry 1.32 $kg$ more of Hydrogen Peroxide, however the inferior $Isp$ would cause the increase in terms of mass flow rate, needed by the main engine to provide 50 $N$ of thrust, resulting in a total consumption of around 0.247 $kg$ more of propellant.

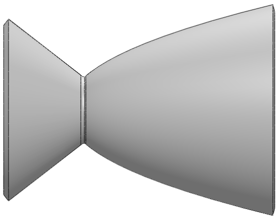

**Figure 5.6:** Optimized bell nozzle.

For this reasons, the final design of the propulsion system will provide for a 17 expansion ratio bell nozzle, as the one shown in Fig.5.6, with the possibility of increasing the propellant tank height of around 33.5 *mm* just thanks to the nozzle length reduction, without considering the potential other empty volume inside the drone. A final optimized design of the propulsion system is shown in Fig.5.7.

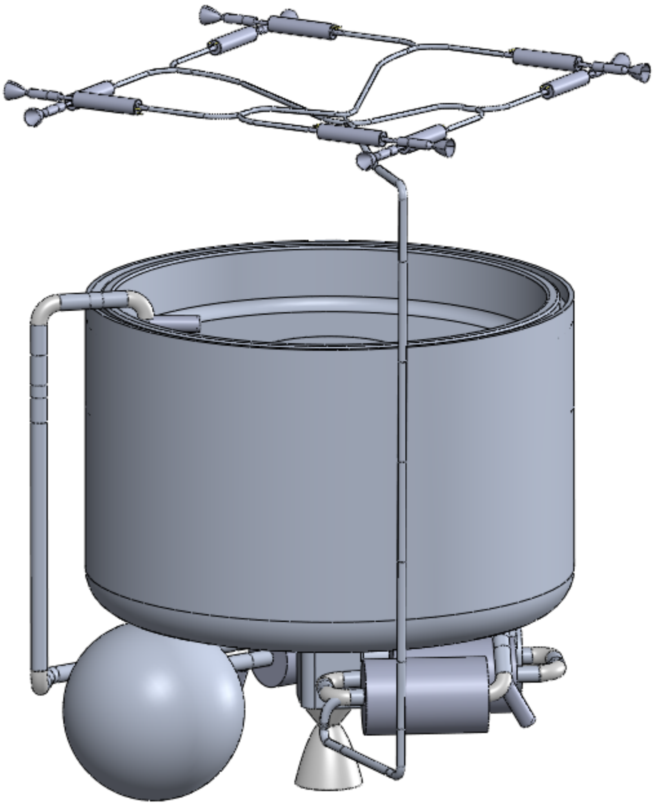

**Figure 5.7:** Final optimized design for the propulsion system.

# Chapter 6

# Drone structure and ACS design

At this point of the study, a quite definitive design for the LuNaDrone propulsion system has been obtained, but all its components cannot be left free to float in the $20x20x30$ $mm$ volume. There is a need for a fixed external structure that encloses, protects and anchors the components to itself.

In this chapter will be shown how the external structure have been designed and mostly how this affected the attitude control subsystem.

## 6.1 Structure design

Since the dimensions of the drone coincide with a 12U CubeSat, it is reasonable to design the structure on the model of its primary structure.

Two general approaches are common for primary structures in the small spacecraft market: commercial-off-the-shelf (COTS) structures and custom machined or printed components. There are several companies providing for spacecraft primary structures, most are machined from aluminum alloy 6061 or 7075 and are designed with several mounting locations for components to allow flexibility in spacecraft configuration. They come in different types, like monocoque, modular frame or custom primary structure.

Monocoque structures skins are specifically designed to bear loads and have significant heritage on aircraft. On small spacecraft, the intent of this design is to maximize internal volume, to provide more thermal mass for heat sinks or sources, to allow for more mounting points and to have more surface area to potentially reduce total ionizing dose (TID). Monocoque construction is common, and “extruded” designs are relatively easy to fabricate through CNC machining, waterjet, or laser cutting.

Modular frames, as the name suggest, come in modular units to assemble in order to obtain a bigger structure. They allow for a flexible internal design for quick turn missions, while still ensuring strict adherence to external dimensions of the CubeSat standard, especially when deployment from a standardized, reusable dispenser is a requirement. Finally, the custom primary structures design require to respect detailed interface requirement guidelines. These focus on payload designs with the understanding of rideshare safety considerations for mission readiness and deployment methods. Safety considerations include safety switches, such as the "remove before flight" pins and foot switch, and requirements that the spacecraft remain powered-off while stowed in the deployment dispensers. The required interface documents originate with the rideshare integrator for the specific dispenser being used with the launch vehicle. The launch vehicle provider typically also provides for the launch vibrational conditions.

For this case study, since the elements that the drone will carry are many in a tiny amount of volume, disposed in a very peculiar configuration, it will probably be necessary to design a custom primary structure, in a monocoque configuration.

The reference model for the design of drone external structure was ISISPACE[1], in particular their 12-Unit CubeSat structure shown in Fig.6.1. However, it must be said that this will be just a qualitative design to understand the encumbrances and masses of the primary external structure. In fact, very likely it will be changed during further developments, in order to meet the LuNaDrone navigation requirements and the launch vehicle provider conditions.

**Figure 6.1:** ISISPACE 12-Unit CubeSat structure.

Following all the indications and dimensions provided in the data sheet[9], an almost identical structure have been designed, where the lateral faces follow the same pattern of the original ones, while the lower base is quite different because it must present an open spot to permit the release of accelerated combustion products from the nozzle.

Even if this design is just at quantitative level, it should follows all the structural requirements required by ISISPACE, such as:

- "Rails must be smooth and edges must be rounded to a minimum radius of 1 *mm*".
- "At least 75% (85.125 *mm* of a possible 113.5 *mm*) of the rail must be in contact with the P-POD rails. 25% of the rails may be recessed and no part of the rails may exceed the specification".
- "All rails must be hard anodized to prevent cold-welding, reduce wear, and provide electrical isolation between the CubeSats and the P-POD".
- "Separation springs must be included at designated contact points".
- "The use of Aluminum 7075 or 6061-T6 is suggested for the main structure".

Of course, the structure must be able to bear the maximum structural loads, that are the one the drone undergoes during the launch. About this, no FEM analysis has been made as the carrier is still to be determinate meaning the launch vibrational conditions are still unknown.

A possible design for the lateral, upper and lower faces structure is shown in Fig.6.2.

---

[1] "A company specialized in realizing innovative turn-key small satellite missions including launch and operations for in-orbit delivery."

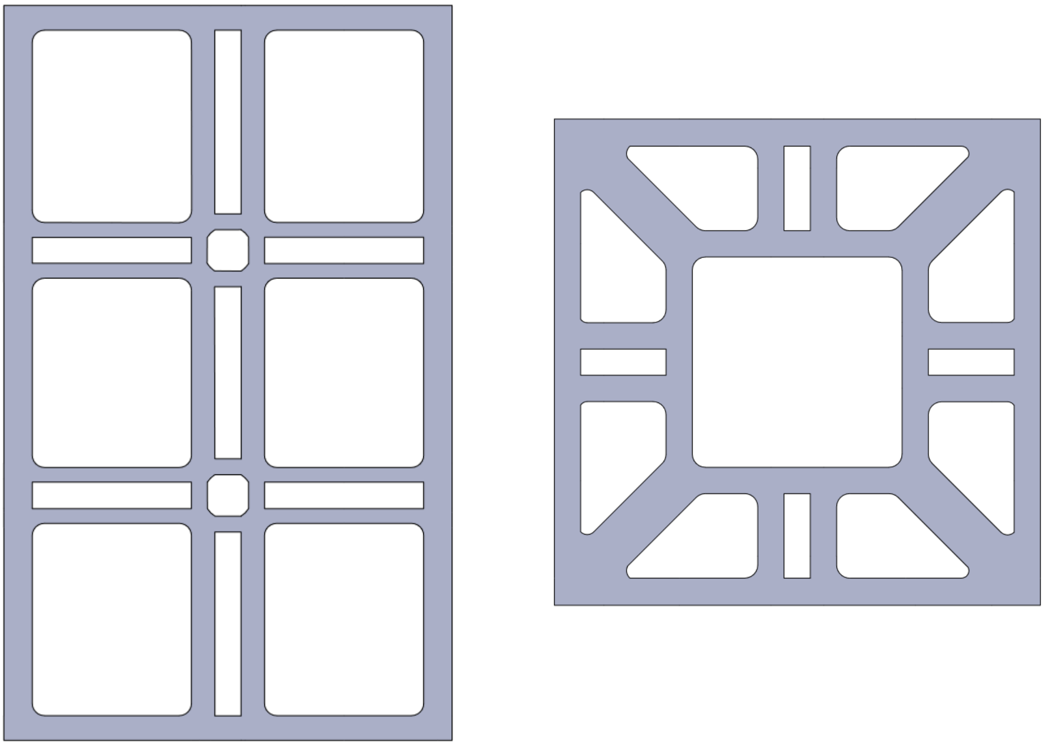

**Figure 6.2:** On the left is shown the 5 $mm$ thick lateral face structure while on the right the lower (and upper) base structure.

Assembling four of the lateral faces and two bases with the deployment switches and separation springs, a complete external primary structure for the drone can be obtained. The final design for the drone structure can be seen in Fig.6.3.

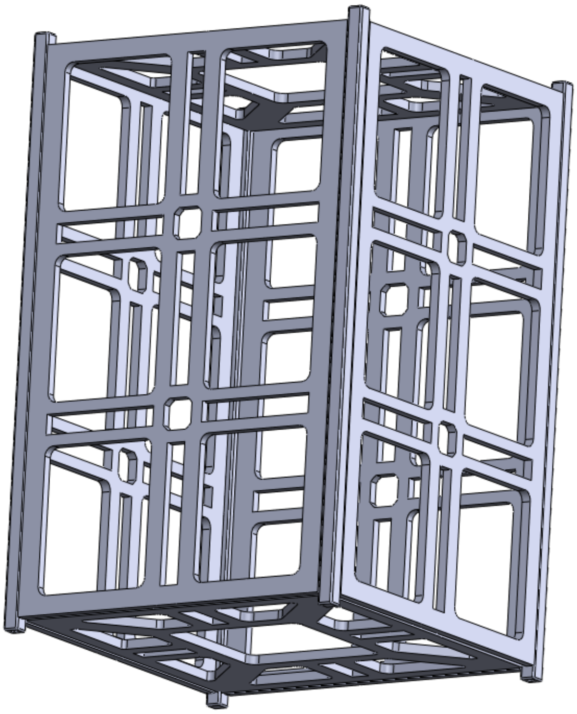

**Figure 6.3:** Final design for the LuNaDrone external primary structure.

## 6.2 ACS design

The actual configuration for the ACS thrusters provides for eight 1 $N$ engines, two for each lateral face of the drone, placed at the four top edges of the drone. Each thruster is coupled with a a Lee IEP solenoid valve of 4.7 $grams$ of mass, about 0.5 $ms$ of response time and 4100 $Lohm$ flow rate. Thanks to the latter it is possible to know the predicted pressure drop, following the instruction on The Lee Company's website[22] that can be seen in Fig.6.4, it's possible to provide a pressure drop of around 0.213 $bar$ for a 1 $N$ thruster.

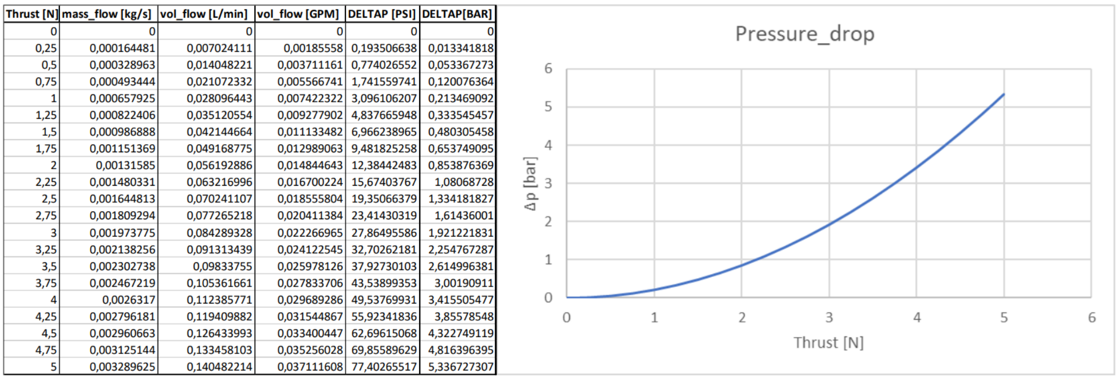

| Thrust [N] | mass_flow [kg/s] | vol_flow [L/min] | vol_flow [GPM] | DELTAP [PSI] | DELTAP[BAR] |
|---|---|---|---|---|---|
| 0 | 0 | 0 | 0 | 0 | 0 |
| 0,25 | 0,000164481 | 0,007024111 | 0,00185558 | 0,193506638 | 0,013341818 |
| 0,5 | 0,000328963 | 0,014048221 | 0,003711161 | 0,774026552 | 0,053367273 |
| 0,75 | 0,000493444 | 0,021072332 | 0,005566741 | 1,741559741 | 0,120076364 |
| 1 | 0,000657925 | 0,028096443 | 0,007422322 | 3,096106207 | 0,213469092 |
| 1,25 | 0,000822406 | 0,035120554 | 0,009277902 | 4,837665948 | 0,333545457 |
| 1,5 | 0,000986888 | 0,042144664 | 0,011133482 | 6,966238965 | 0,480305458 |
| 1,75 | 0,001151369 | 0,049168775 | 0,012989063 | 9,481825258 | 0,653749095 |
| 2 | 0,00131585 | 0,056192886 | 0,014844643 | 12,38442483 | 0,853876369 |
| 2,25 | 0,001480331 | 0,063216996 | 0,016700224 | 15,67403767 | 1,08068728 |
| 2,5 | 0,001644813 | 0,070241107 | 0,018555804 | 19,35066379 | 1,334181827 |
| 2,75 | 0,001809294 | 0,077265218 | 0,020411384 | 23,41430319 | 1,61436001 |
| 3 | 0,001973775 | 0,084289328 | 0,022266965 | 27,86495586 | 1,921221831 |
| 3,25 | 0,002138256 | 0,091313439 | 0,024122545 | 32,70262181 | 2,254767287 |
| 3,5 | 0,002302738 | 0,09833755 | 0,025978126 | 37,92730103 | 2,614996381 |
| 3,75 | 0,002467219 | 0,105361661 | 0,027833706 | 43,53899353 | 3,00190911 |
| 4 | 0,0026317 | 0,112385771 | 0,029689286 | 49,53769931 | 3,415505477 |
| 4,25 | 0,002796181 | 0,119409882 | 0,031544867 | 55,92341836 | 3,85578548 |
| 4,5 | 0,002960663 | 0,126433993 | 0,033400447 | 62,69615068 | 4,322749119 |
| 4,75 | 0,003125144 | 0,133458103 | 0,035256028 | 69,85589629 | 4,816396395 |
| 5 | 0,003289625 | 0,140482214 | 0,037111608 | 77,40265517 | 5,336727307 |

**Figure 6.4:** Pressure drop of IEP series solenoid valves by The Lee Company.

The thrusters are thought to fire coupled with their symmetrical at the opposite angle, as shown schematically in Fig.6.5, in order to provide pure couple around the roll axis.

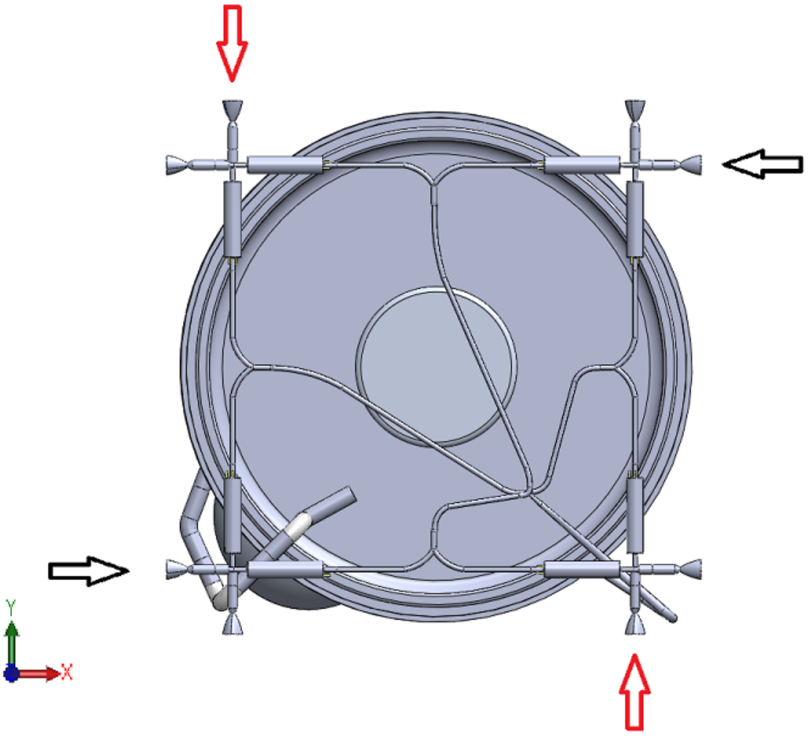

**Figure 6.5:** Example of two possible firing configuration for the ACS thrusters in order to obtain pure couple around the roll axis. In both these examples, the ACS thrusters provide a counterclockwise rotation.

The actual design is not provided for obtaining a pure couple also around the pitch and yaw axis, in order to obtain them it would be necessary to add at least two more thrusters and place them on the lower edges of the drone.
However, at the moment this is not supposed to be necessary because it would be acceptable to have the lever only on top, so that the drone moves in the same direction of the side that will be inclined.
A schematic representation of how the pitch and yaw rotations will be obtained is shown in Fig.6.6 and Fig.6.7, where for both the rotations two thrusters are shooting in the same direction, in order to compensate the roll couple that would be created otherwise.
In order to determine if it will be acceptable to make the whole drone move in the same direction of firing of the ACS in the case of pitch and yaw control, a dynamic simulation would be necessary.

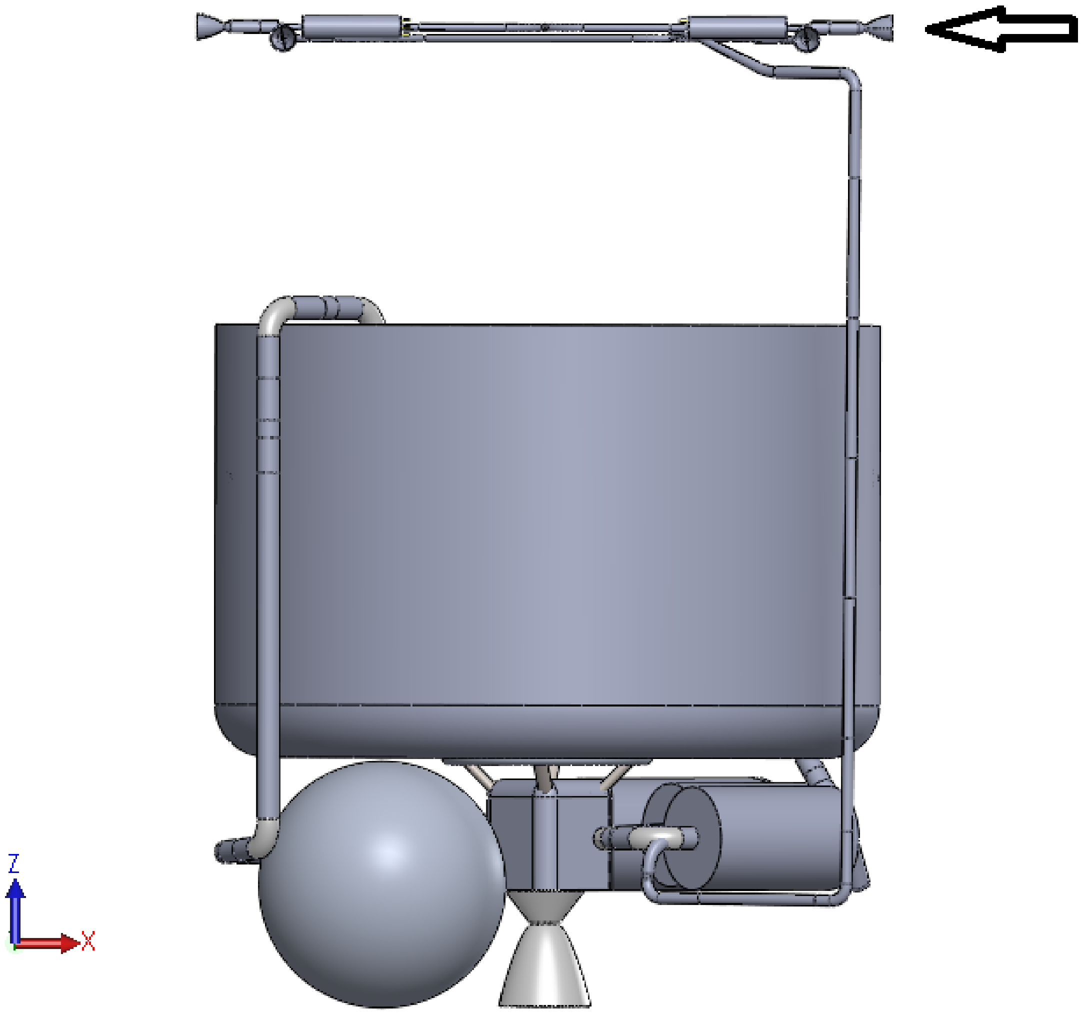

**Figure 6.6:** Example of a firing configuration for the ACS thrusters in order to obtain a non pure couple around the pitch axis.

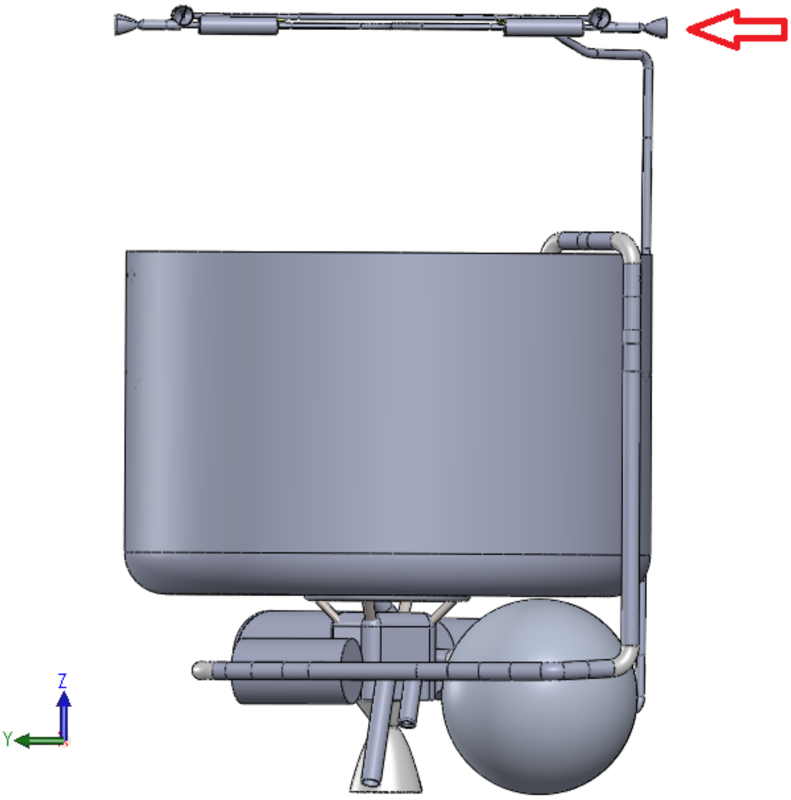

**Figure 6.7:** Example of a firing configuration for the ACS thrusters in order to obtain a non pure couple around the pitch axis.

Once the firing procedures have been defined, a possible configuration for placing the eight thruster was obtained, paying attention to the fact that having an external structure is a limitation in terms of available volumes. Furthermore, a possible solution for fixing the eight thrusters to the structure should be found, paying attention that it would resist the launch vibrational loads.

As can be seen in Fig.6.8, the four thrusters shooting in y-direction are placed right under the remaining four, which in turn are placed at the first available position under the structure.

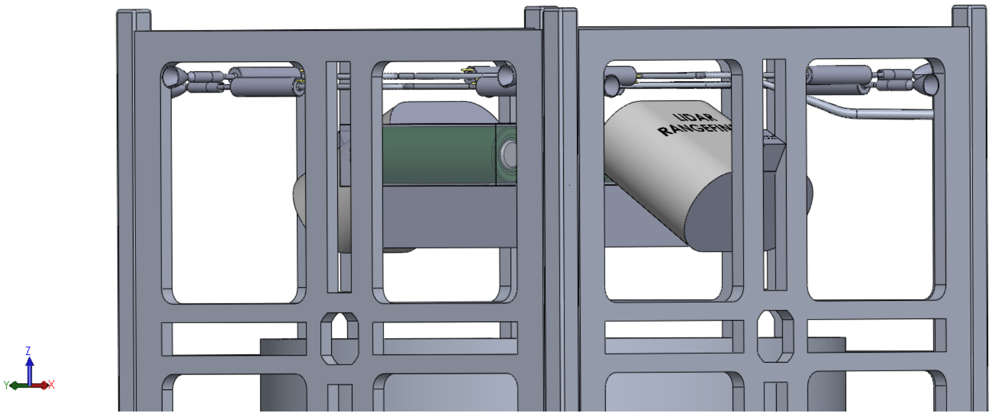

**Figure 6.8:** ACS thrusters configuration.

### 6.2.1 ACS thrusters design

At this point a it could be possible to calculate the maximum actuation time (they are supposed to work in bang-bang mode) of the eight ACS thrusters in order to satisfy the drone requirements, that are mostly navigation requirements, which are 1° of angle precision and 80° per second of angular velocity tolerance.
Considering the two different directions of the thrusters (x and y-direction), the four relevant arms referred to the geometrical center of the drone are shown in table 6.1, along with the three principal moments of inertia.

| | | |
|---|---|---|
| $B_{x\_y}$ | Arm $x$, y-direction thruster $[m]$ | 0.07546 |
| $B_{y\_x}$ | Arm $y$, x-direction thruster $[m]$ | 0.07489 |
| $B_{z\_x}$ | Arm $z$, x-direction thruster $[m]$ | 0.13444 |
| $B_{z\_y}$ | Arm $z$, y-direction thruster $[m]$ | 0.13109 |
| $I_x$ | X principal moment of inertia $[kg\ m^3]$ | $35808623.93\ e - 9$ |
| $I_y$ | Y principal moment of inertia $[kg\ m^3]$ | $59895302.87\ e - 9$ |
| $I_z$ | Z principal moment of inertia $[kg\ m^3]$ | $62542437.11\ e - 9$ |

**Table 6.1:** Distances between the thrusters and the mass center of the drone and its principal moments of inertia, estimated for the dry drone.

According to the simulations, with this design for the attitude control subsystem, the maximum actuation time of the eight thruster in order to satisfy the navigation requirements is 0.0488 $s$ which, according with a T4i expert, is an achievable value.
In addition to the drone navigation, the ACS thrusters are also useful to make small attitude adjustments, in order to correct manufacturing errors of the nozzle as misalignment of the thrust direction in terms of axis offset and inclination.
Assuming an offset of the nozzle axis direction of 1 $mm$ and radial and tangential misalignment of 0.5 degrees, it is possible to calculate the derivative error couples on the roll, pitch and yaw axis. Consequently the needed force the thrusters have to provide in x and y-directions to correct the pitch and yaw couples can be easily calculated. However, by shooting thrusters paired as shown in Fig.6.6 and Fig.6.7, only these two couples are corrected, leaving the roll error still to be adjusted. In order to compensate the roll error couple it will necessary to shot with two opposites thrusters as shown in Fig.6.5. This additional thrust can be provided by two thrusters firing in x-direction, by two thrusters firing in y-direction or it can be even partitioned between four thruster firing in the two directions.
According to the simulations, in order to correct the pitch eventual error couple each of the two thrusters should provide at least a thrust of 0.3969 $N$, to correct the yaw couple they should provide a thrust of .4071 $N$, while the remaining roll couple to correct can be divided as shown in Fig.6.9 and Fig.6.10.

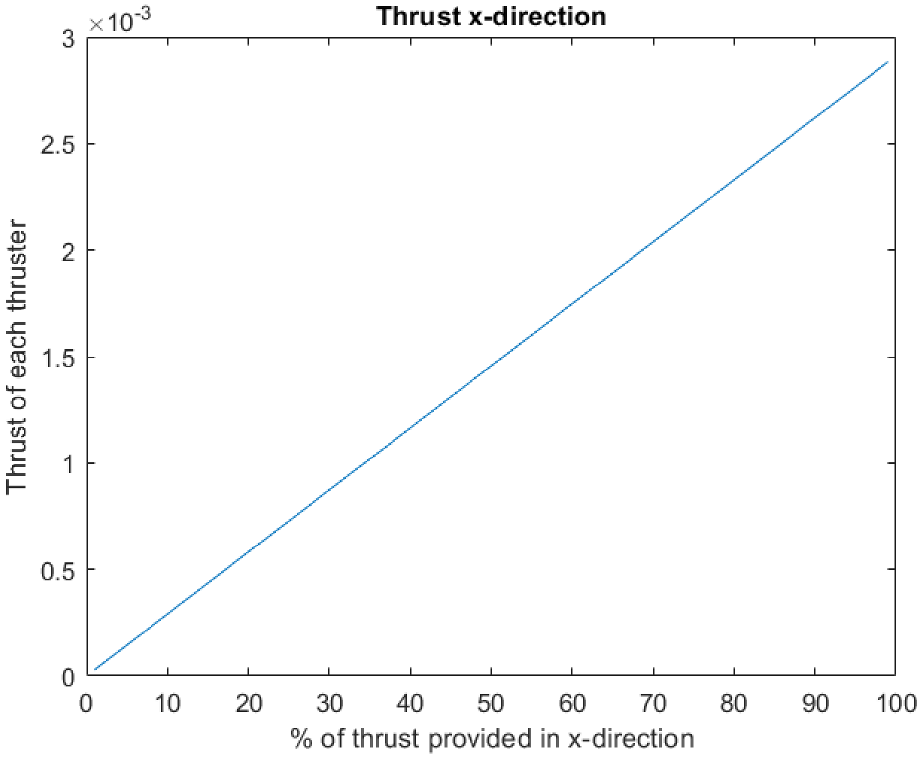

**Figure 6.9:** Minimum thrust that each of the two thrusters firing in x-direction should provide in order to compensate its part of the roll error couple.

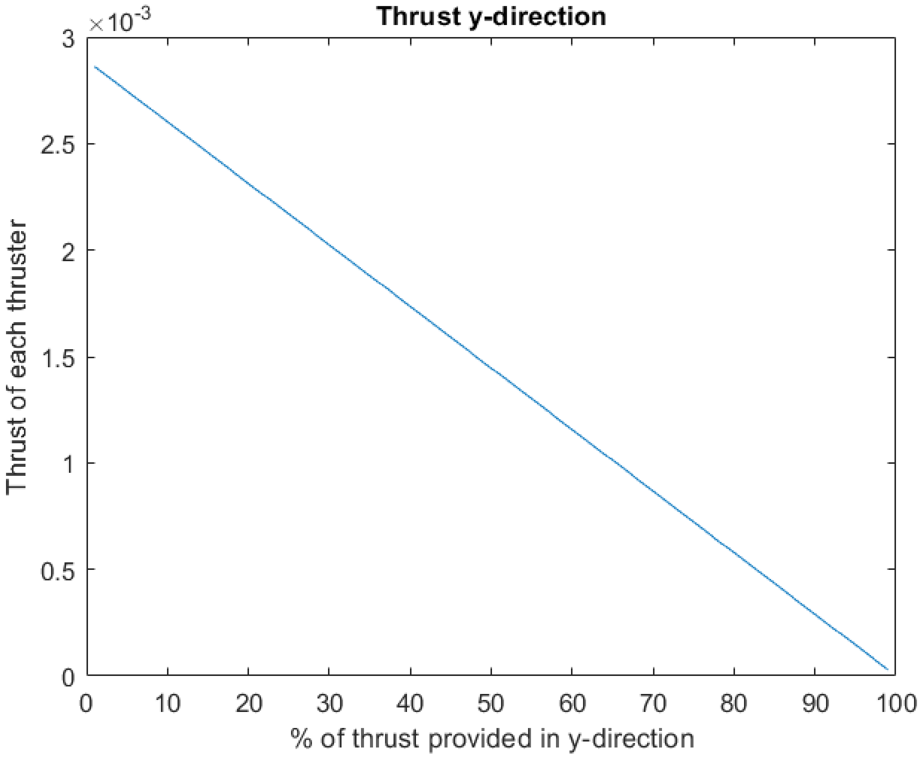

**Figure 6.10:** Minimum thrust that each of the two thrusters firing in y-direction should provide in order to compensate its part of the roll error couple.

If the roll couple is equally partitioned between the two directions, each of the four involved thruster should provide at least a 0.0015 $N$ thrust, this low results from the low couple to compensate, which is three orders of magnitude smaller than the others because only the tangential misalignment provide a roll couple.
In the end, it is possible to affirm that 1 $N$ thrusters are enough to compensate the manufacturing errors of the main nozzle.

# Chapter 7

# Conclusions and recommendations

This thesis started with the aim of try to make the LuNaDrone mission feasible, specifically to design a working propulsion system compatible with the requirements.
A final design for this 12-U, 20x20x30 *cm* autonomous non-orbiting flying drone has been obtained and can be seen in Fig.7.1, where is displayed the propulsion system, and in Fig.7.2, where the whole drone with all its components is shown.

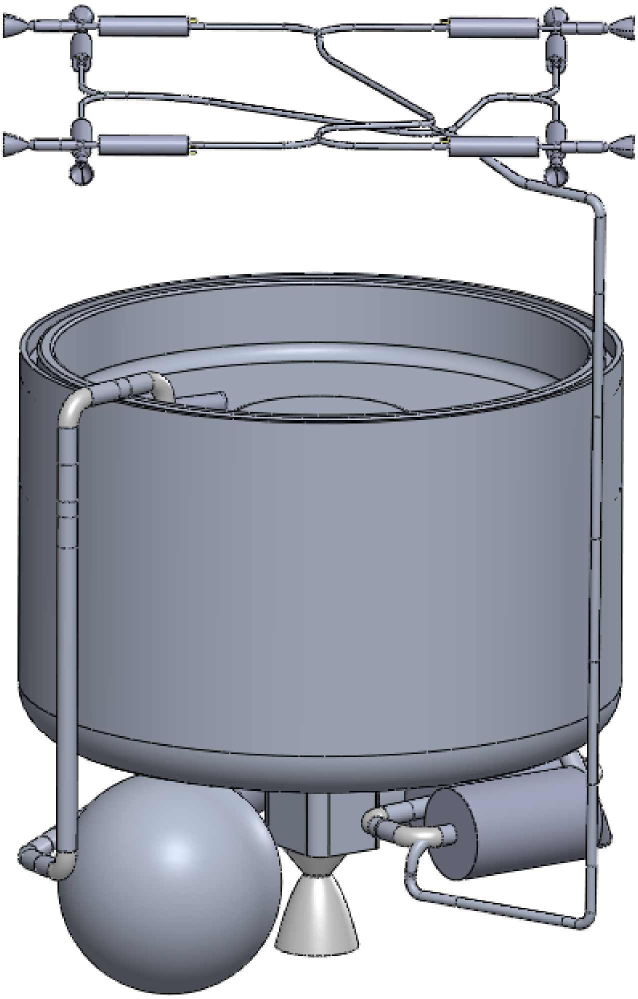

**Figure 7.1:** Final design for the LuNaDrone propulsion system.

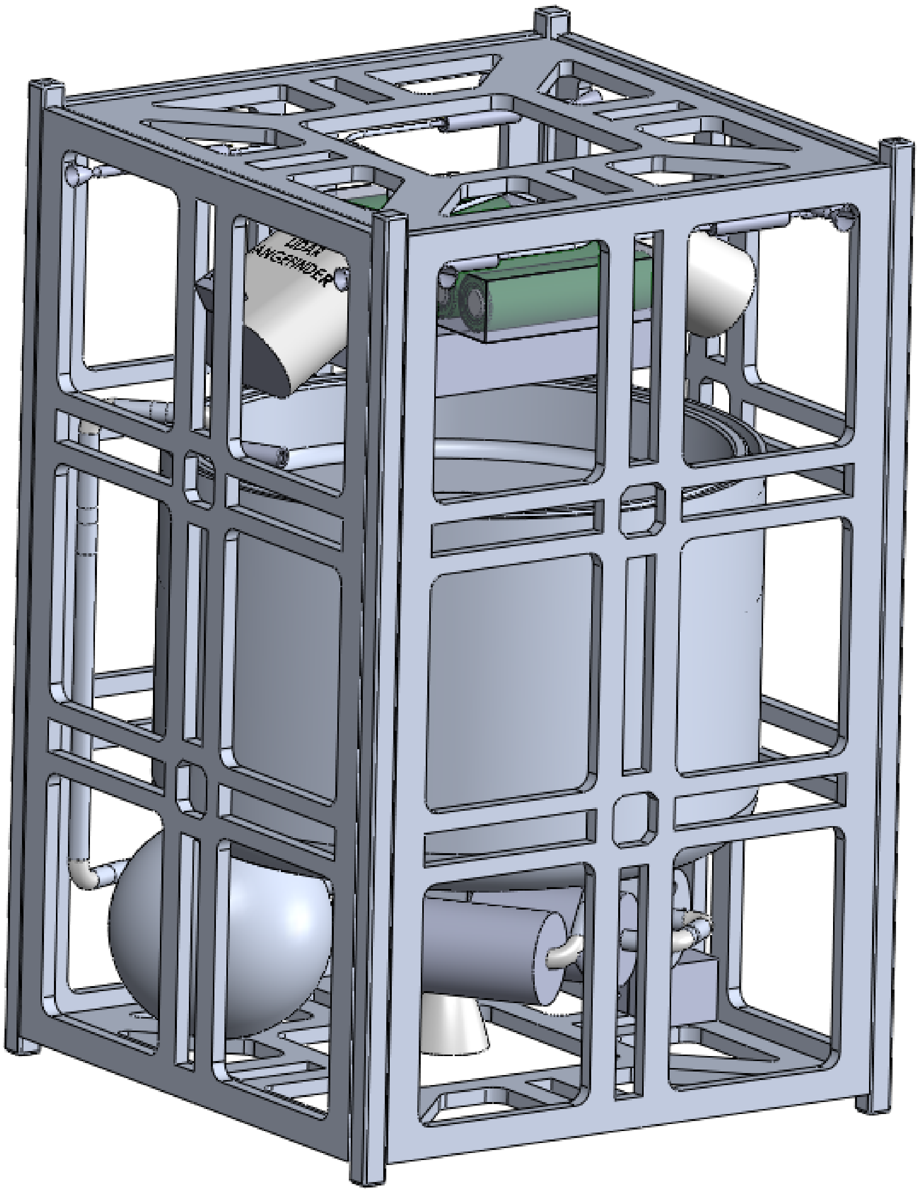

**Figure 7.2:** Final design for the whole LuNaDrone.

However, this is not a working design for what was said in Chapter 4, since the two chosen solenoidal valves of the propellant fluidic line are not compatible with the operative conditions in terms of volumetric flow. A possible solution would be continue collaborating with the Lee seller in order to obtain a quote for a custom valve both for the $H2O2$ *valve* and the *Main engine valve*, otherwise it will be necessary to find another COTS valve from another company. Furthermore, the pressurant pressure regulator is still to be determined, even if the TESCOM's BB1 Series Pressure Regulator OEM could be a valuable alternative. Leaving aside these problems, the main features of the propulsion design are shown in table 7.1.

| | |
|---|---|
| Propellant tank internal volume | 2380730 $mm^3$ |
| Propellant tank internal pressure | 18 $bar$ |
| Propellant mass | 3.3092 $kg$ |
| Pressurant tank internal pressure | 350 $bar$ |
| Combustion chamber internal pressure | 10 $bar$ |
| Mass flow rate | 0.0346549 $kg\ s^{-1}$ |
| Nozzle expansion ratio | 17 |
| Throat diameter | 6.26 $mm$ |
| Isp | 147.07 $s$ |
| Total nozzle length | 35.5 $mm$ |
| Thrust | 50 $N$ |
| Total dry drone mass | 4.87 $kg$ |
| Total wet drone mass | 8.18 $kg$ |

**Table 7.1:** Propulsion system main features.

The components external to the propulsion system, have been arranged in a possible optimal configuration, as shown in detail in Fig,7.3, where the two 60° Lidar Range Finder (corresponding to number 3) have been moved on top of the propellant tank, along with the batteries and the on board computer (respectively number 1 and 2), while the one pointing perpendicularly under the drone (number 5) must be below the tank along with the payload camera (number 4).

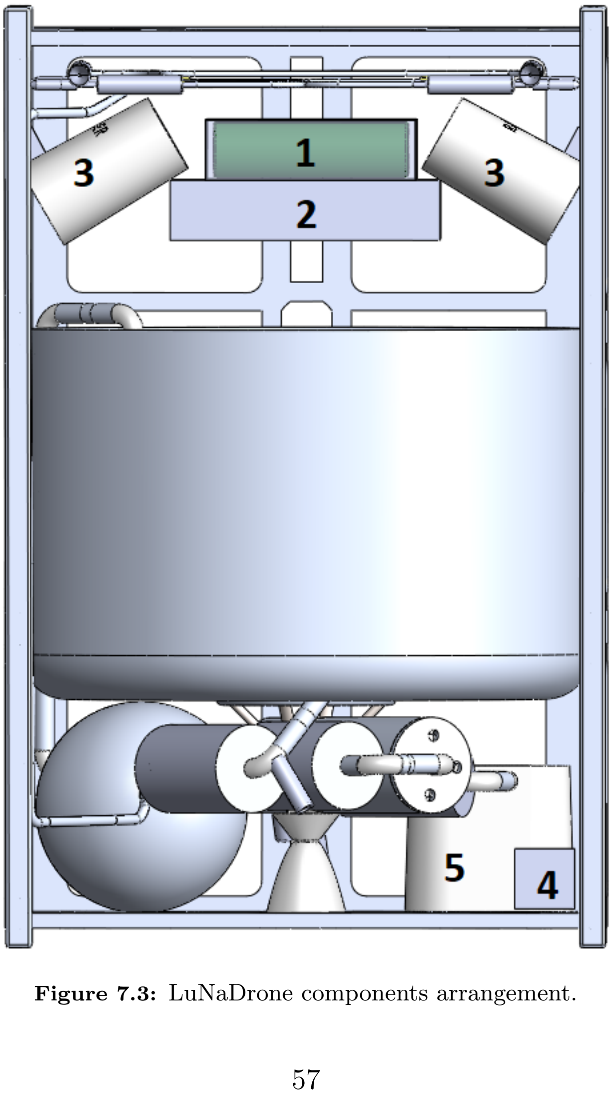

**Figure 7.3:** LuNaDrone components arrangement.

The on board computer and the batteries could also be placed inside the concave part of the top of the propellant tank, since it is essentially a free unused volume, making it more clear how much the propellant tank height could be increased from the actual design, which only provides for the required minimum internal volume.

Future developments should aim to define a definitive fluidic line scheme, making sure it follows the ECSS[5] rules, finding an acceptable product for the *H2O2 valve*, the *Main engine valve* and the *Pressure regulator*.
Furthermore, a CFD analysis of the combustion chamber with canted nozzle configuration could be useful to verify the assumption that the asymmetry of the flow at the nozzle entry does not affect thrust and its direction.
Another element to focus is for sure the design of the actual primary external structure, which must be compatible with the drone navigation requirements and must bear the launch load. Moreover, a possible solution for fixing the eight thrusters to the primary external structure have to be found, paying attention that it would resist the launch vibrational loads. A possible solution could be a ring-like attachment for each thruster, screwed to the structure, through which make the nozzle pass.
For what concerns the propellant tank, the long time storage problem between Ergal 7075 and Hydrogen Peroxide should be deeply analyzed. If the Chrome treatment or the anodization are not sufficient to overcome the corrosion problem, it would be necessary to film the inner surfaces of the tank with a thin layer of Teflon.
Furthermore, the exact number of screws, between the tank and he cap, and their disposition must be determined, in order to do not weaken the tank and to withstand the inside pressure.
Ultimately, a deeper analysis on the required ullage volume should be carried on. This additional volume, occupied by the pressurant in the propellant tank, is required to prevent ruptures resulting from the Hydrogen Peroxide decomposition during storage time. Once the required ullage will be determined, a new pressurant tank design could be evaluated.

# Appendix A

# Chemistry

In this annex are shown the result of a simulation of the chemistry for Hydrogen Peroxide 90% using CproPep, a propellant evaluation software that will let you compute rocket motor performance in function of the propellant. Some of these will be taken as reference values, such as $c^*$, the combustion chamber temperature $T$ and the $c_p$ over $c_v$ ratio.

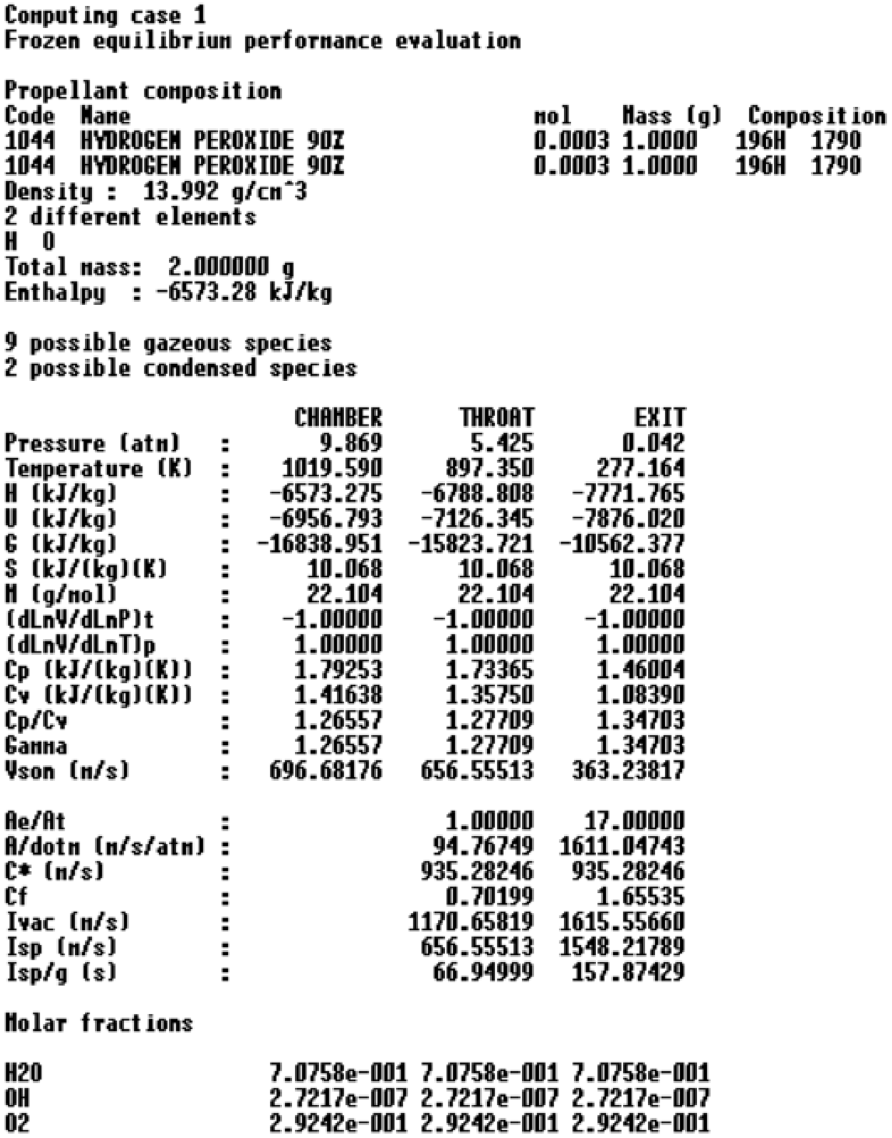

```
Computing case 1
Frozen equilibrium performance evaluation

Propellant composition
Code  Name                                  mol    Mass (g)  Composition
1044  HYDROGEN PEROXIDE 90%                 0.0003 1.0000    196H  179O
1044  HYDROGEN PEROXIDE 90%                 0.0003 1.0000    196H  179O
Density :  13.992 g/cm^3
2 different elements
H  O
Total mass:  2.000000 g
Enthalpy  : -6573.28 kJ/kg

9 possible gazeous species
2 possible condensed species

                          CHAMBER        THROAT          EXIT
Pressure (atm)     :        9.869         5.425         0.042
Temperature (K)    :     1019.590       897.350       277.164
H (kJ/kg)          :    -6573.275     -6788.808     -7771.765
U (kJ/kg)          :    -6956.793     -7126.345     -7876.020
G (kJ/kg)          :   -16838.951    -15823.721    -10562.377
S (kJ/(kg)(K)      :       10.068        10.068        10.068
M (g/mol)          :       22.104        22.104        22.104
(dLnV/dLnP)t       :     -1.00000      -1.00000      -1.00000
(dLnV/dLnT)p       :      1.00000       1.00000       1.00000
Cp (kJ/(kg)(K))    :      1.79253       1.73365       1.46004
Cv (kJ/(kg)(K))    :      1.41638       1.35750       1.08390
Cp/Cv              :      1.26557       1.27709       1.34703
Gamma              :      1.26557       1.27709       1.34703
Vson (m/s)         :    696.68176     656.55513     363.23817

Ae/At              :                    1.00000      17.00000
A/dotm (m/s/atm)   :                   94.76749    1611.04743
C* (m/s)           :                  935.28246     935.28246
Cf                 :                    0.70199       1.65535
Ivac (m/s)         :                 1170.65819    1615.55660
Isp (m/s)          :                  656.55513    1548.21789
Isp/g (s)          :                   66.94999     157.87429

Molar fractions

H2O                     7.0758e-001 7.0758e-001 7.0758e-001
OH                      2.7217e-007 2.7217e-007 2.7217e-007
O2                      2.9242e-001 2.9242e-001 2.9242e-001
```

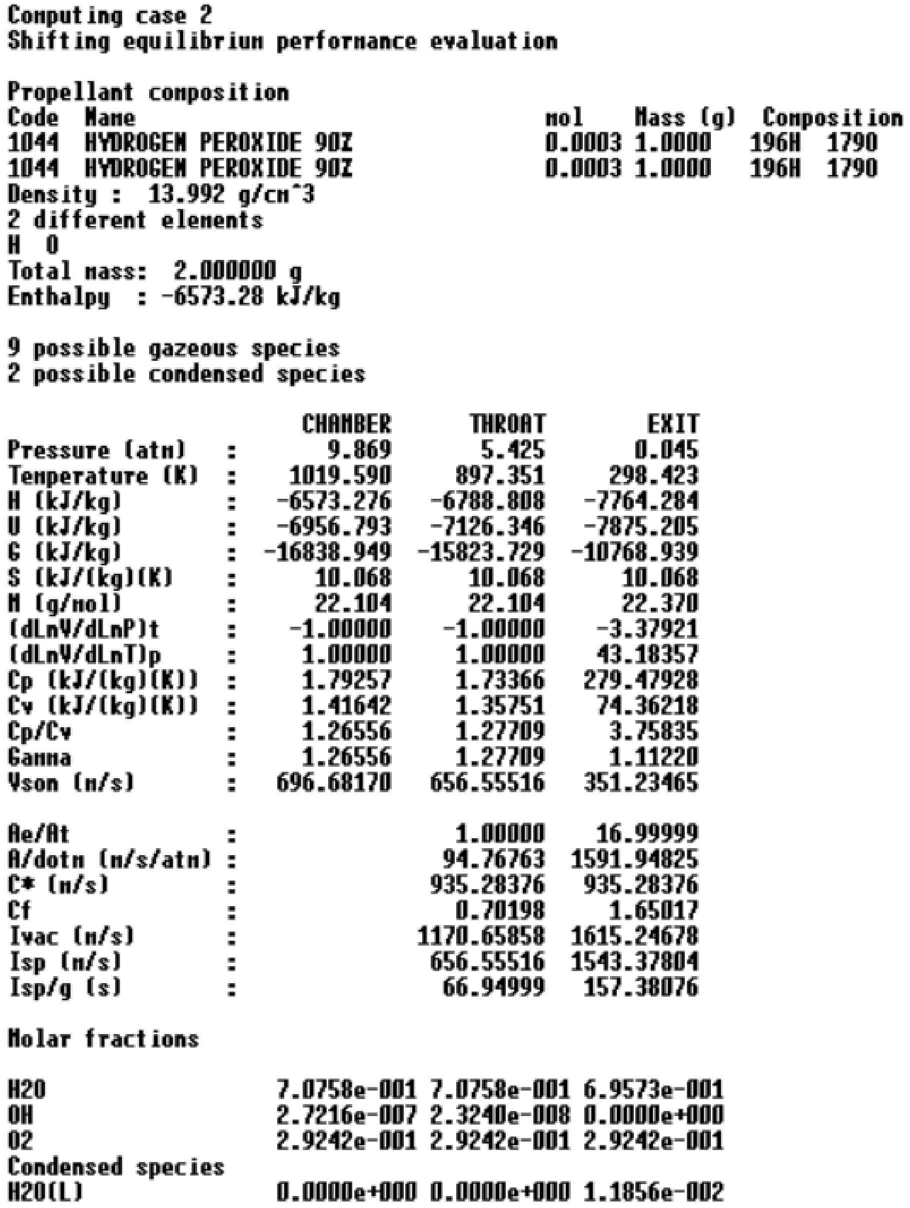

```
Computing case 2
Shifting equilibrium performance evaluation

Propellant composition
Code  Name                                    mol    Mass (g)  Composition
1044  HYDROGEN PEROXIDE 90%                   0.0003 1.0000    196H  1790
1044  HYDROGEN PEROXIDE 90%                   0.0003 1.0000    196H  1790
Density :  13.992 g/cm^3
2 different elements
H  O
Total mass:  2.000000 g
Enthalpy  : -6573.28 kJ/kg

9 possible gazeous species
2 possible condensed species

                          CHAMBER      THROAT        EXIT
Pressure (atm)     :        9.869       5.425       0.045
Temperature (K)    :     1019.590     897.351     298.423
H (kJ/kg)          :    -6573.276   -6788.808   -7764.284
U (kJ/kg)          :    -6956.793   -7126.346   -7875.205
G (kJ/kg)          :   -16838.949  -15823.729  -10768.939
S (kJ/(kg)(K)      :       10.068      10.068      10.068
M (g/mol)          :       22.104      22.104      22.370
(dLnV/dLnP)t       :     -1.00000    -1.00000    -3.37921
(dLnV/dLnT)p       :      1.00000     1.00000    43.18357
Cp (kJ/(kg)(K))    :      1.79257     1.73366   279.47928
Cv (kJ/(kg)(K))    :      1.41642     1.35751    74.36218
Cp/Cv              :      1.26556     1.27709     3.75835
Gamma              :      1.26556     1.27709     1.11220
Vson (m/s)         :    696.68170   656.55516   351.23465

Ae/At              :                  1.00000    16.99999
A/dotm (m/s/atm)   :                 94.76763  1591.94825
C* (m/s)           :                935.28376   935.28376
Cf                 :                  0.70198     1.65017
Ivac (m/s)         :               1170.65858  1615.24678
Isp (m/s)          :                656.55516  1543.37804
Isp/g (s)          :                 66.94999   157.38076

Molar fractions

H2O                       7.0758e-001 7.0758e-001 6.9573e-001
OH                        2.7216e-007 2.3240e-008 0.0000e+000
O2                        2.9242e-001 2.9242e-001 2.9242e-001
Condensed species
H2O(L)                    0.0000e+000 0.0000e+000 1.1856e-002
```

# Appendix B

# Propellant tank stress simulations

In this annex are shown the result of each simulation carried out on the three alternative design for the propellant tank. The SOLIDWORKS Simulation add-in has been used for each analysis.

The initial design for the propellant tank provided for 2 *mm* thick lateral walls and 5 *mm* thick bases, which, if subjected to an internal pressure of 18 *bar*, undergoes the stresses shown in Fig.B.1. It can be easily seen that the upper and lower bases host the most critical stresses in the middle of each face and in correspondence of the edges. Their value does not match with the safety requirement of having at least a factor of safety of 2 on each spot of the tank, they even exceed the yield stress of AISI 316 stainless steel, meaning that this design would lead to the failure of the tank.

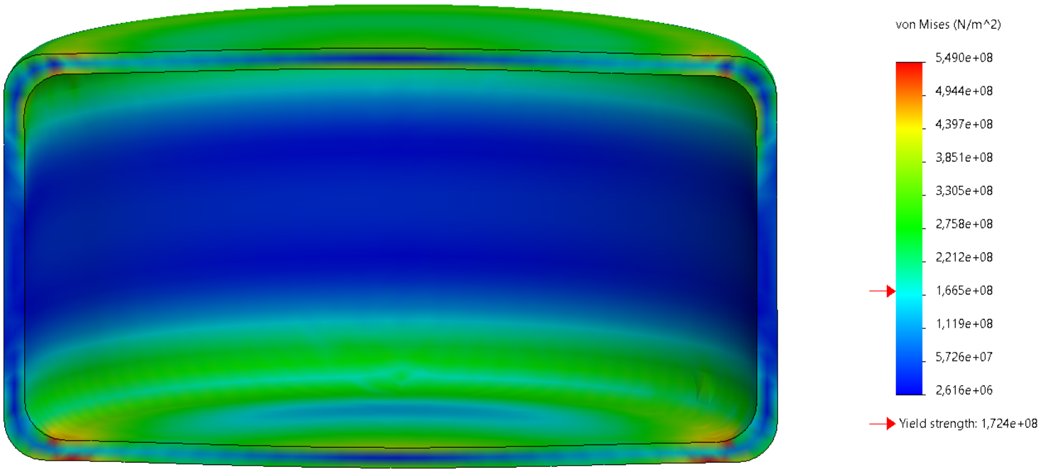

**Figure B.1:** Stresses for the cylindrical propellant tank in its initial design.

The first alternative was the one which provided for increasing the thickness of the whole upper and lower faces, until the stresses on the most critical spots will be at most half of the yield stress of AISI 316 stainless steel, following the von Mises criterion. In Fig.B.2 are shown the resultant stresses the tank undergoes if its upper and lower faces are increased in thickness by 10 *mm*, reaching 15 *mm*.

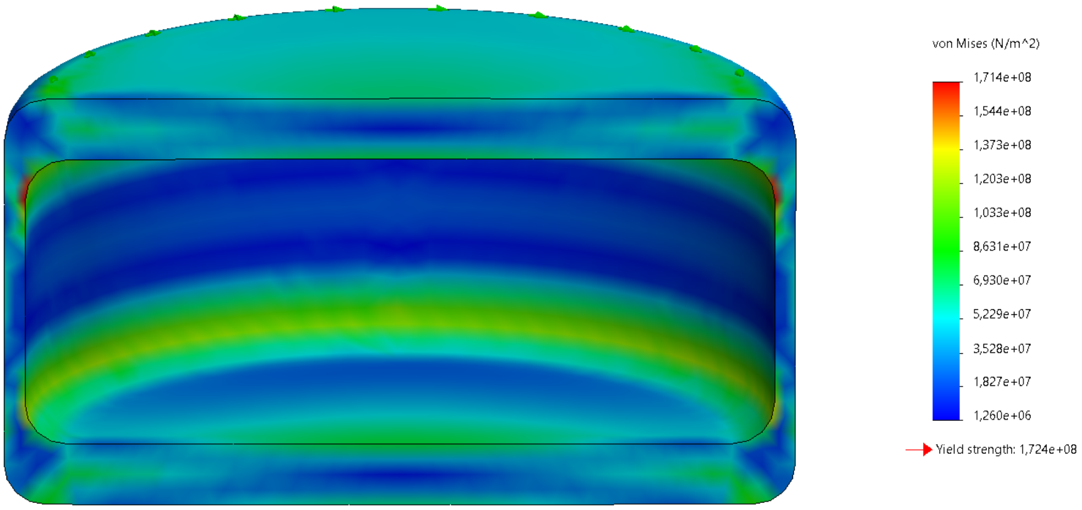

**Figure B.2:** Stresses for the cylindrical propellant tank with thickened upper and lower bases.

It can be seen that the stress issues slightly persist and the mass increase is significant.

The second solution, instead, provided for fixing to the upper and lower bases an isogrid like reinforcement. The simulation of the stresses acting on the propellant tank with this design are shown in Fig.B.3.

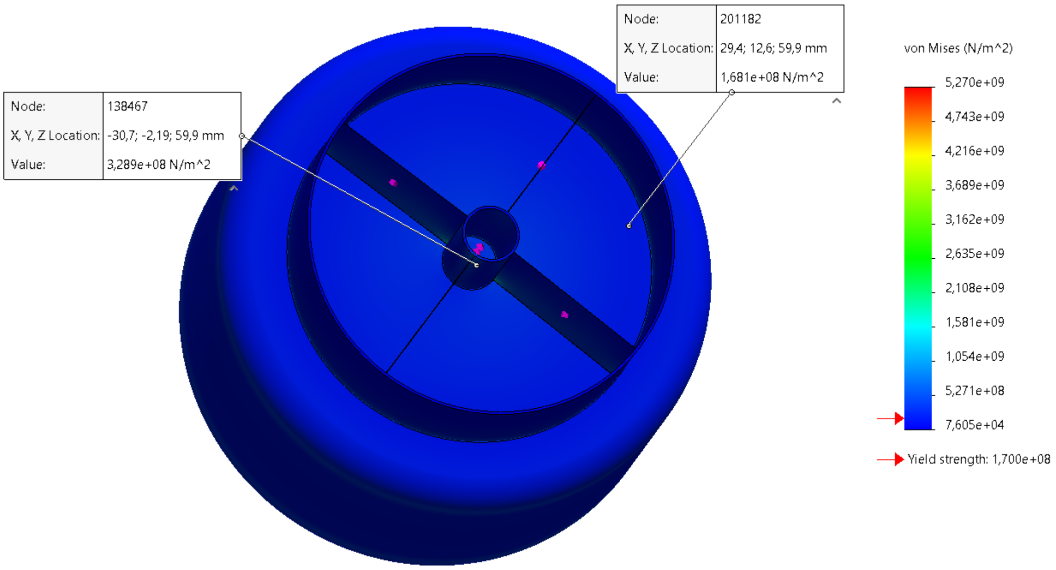

**Figure B.3:** Stresses for the cylindrical propellant tank with isogrid reinforcements for the upper and lower bases.

The colours of this graphic could be misleading because it could seems like there are very low stresses on each spot of the tank. However, the sharp edges of the isogrid reinforcements, combined with the not too fitted mesh of the simulation, sent the legend off scale. The probed spots could help to read the graphic correctly.

The third solution provided for implementing other possible materials and geometries for the whole tank. Using ERGAL 7075 as material for the tank, increasing the curvature radius on the edges, from 10 $mm$ to 15 $mm$, and adding a reinforcement disc at the center of the bases with 30 $mm$ of radius and 2 $mm$ of thickness, would resolve the stresses problem. The simulation of the stresses acting on the propellant tank and cap with this design are shown in Fig.B.4, B.5, B.6 and B.7 .

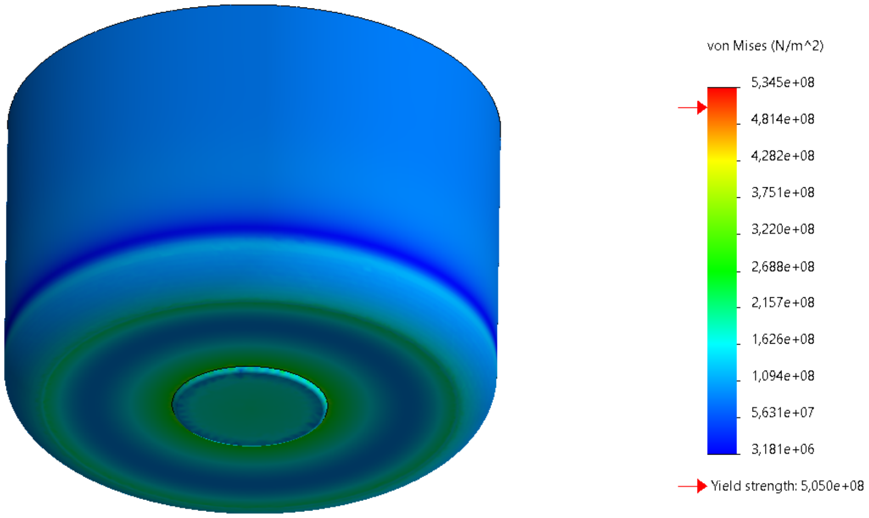

**Figure B.4:** Stresses for the Ergal 7075 propellant tank.

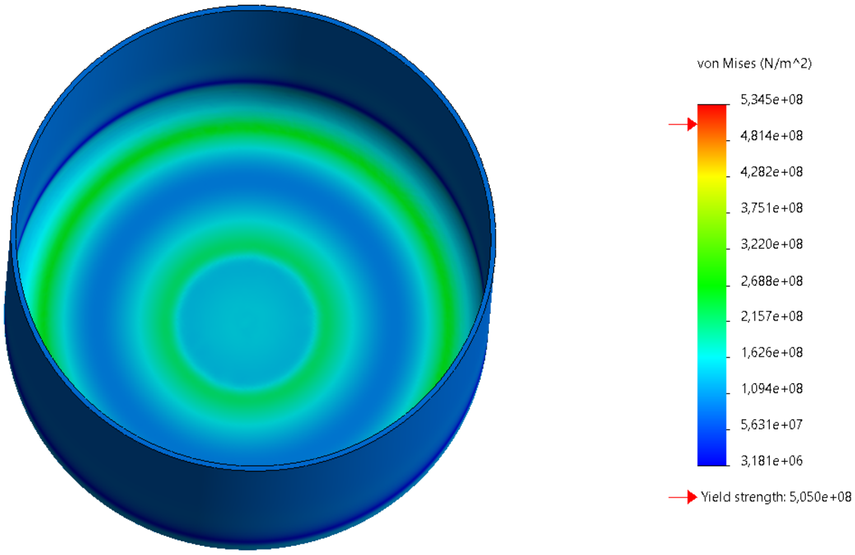

**Figure B.5:** Stresses for the Ergal 7075 propellant tank.

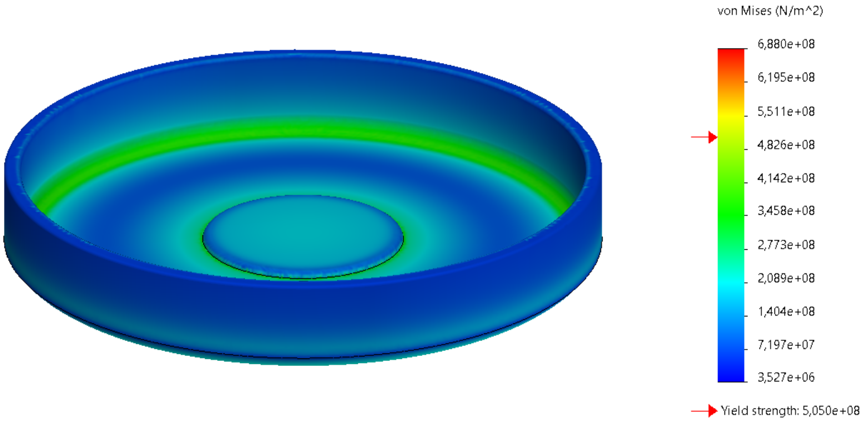

**Figure B.6:** Stresses for the Ergal 7075 propellant tank cap.

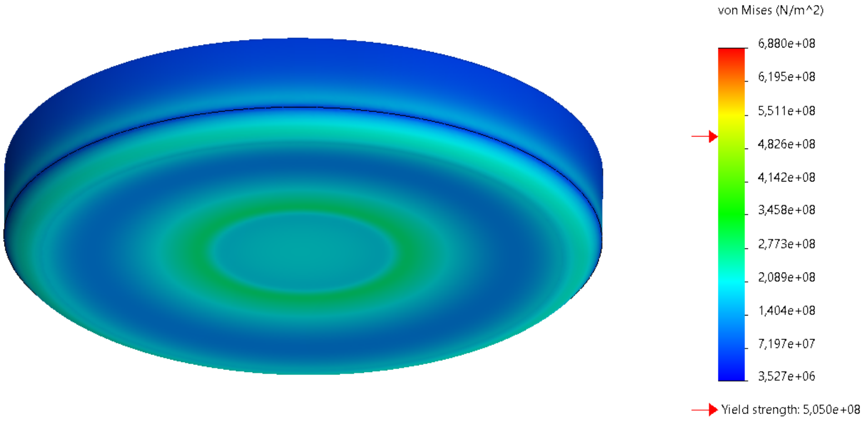

**Figure B.7:** Stresses for the Ergal 7075 propellant tank cap.

# Appendix C

# Main engine nozzle optimization

In this annex are shown in detail the results of the MATLAB analysis regarding the main engine nozzle optimization.

It's been developed a code which works by imposing the required thrust of 50 $N$, the chamber pressure of 10 $bar$, $c^*$, the combustion chamber temperature $T$ and the $c_p$ over $c_v$ ratio, where these last ones were obtained from CproPep. Making the expansion ratio vary between 10 and 70, for each step it calculates the corresponding values of $C_f$, $Isp$, mass flow rate, throat area and and all the other dependent parameters. Considering the minimum acceptable length of the nozzle, due to the pressurant tank, it is possible to determine the minimum expansion ratio (17) and the correspondent propellant tank height increase, hence the additional propellant mass storable.

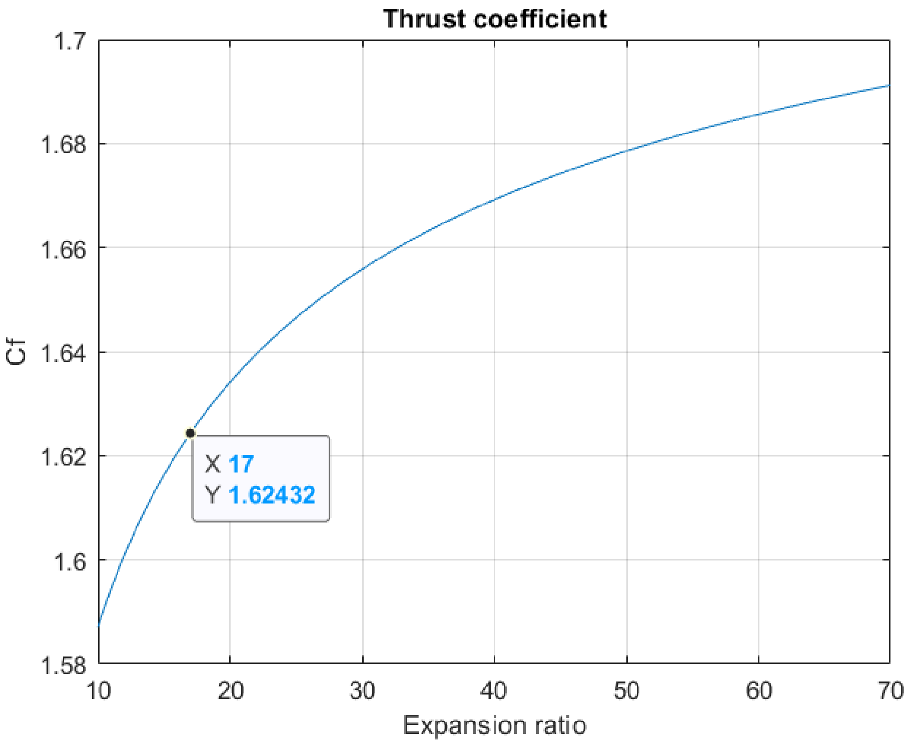

**Figure C.1:** Relationship between the thrust coefficient and the expansion ratio of the bell nozzle.

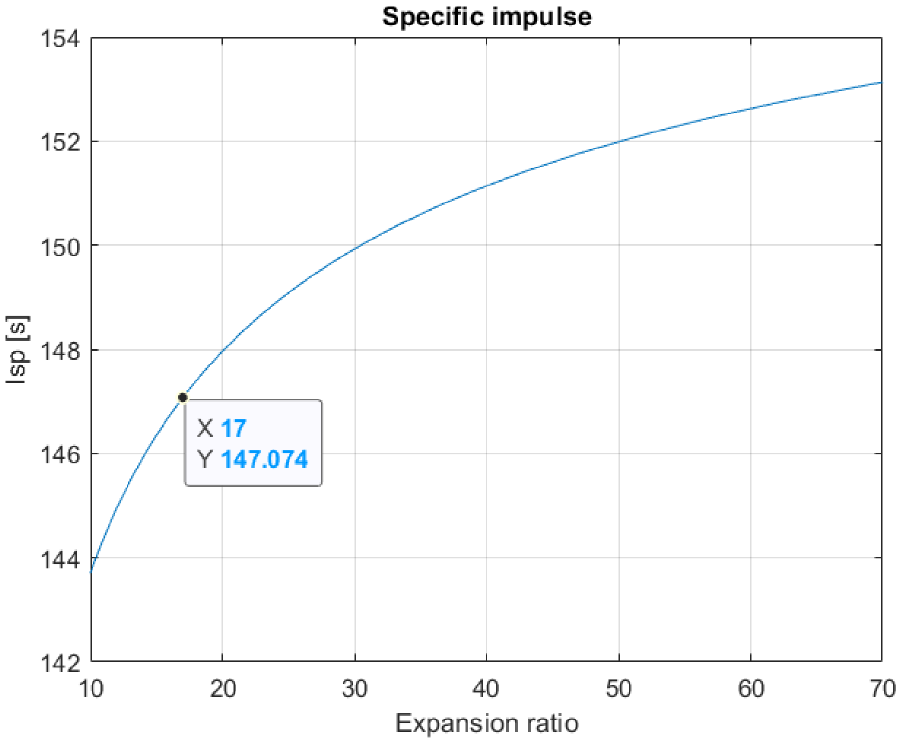

**Figure C.2:** Relationship between the specific impulse and the expansion ratio of the bell nozzle.

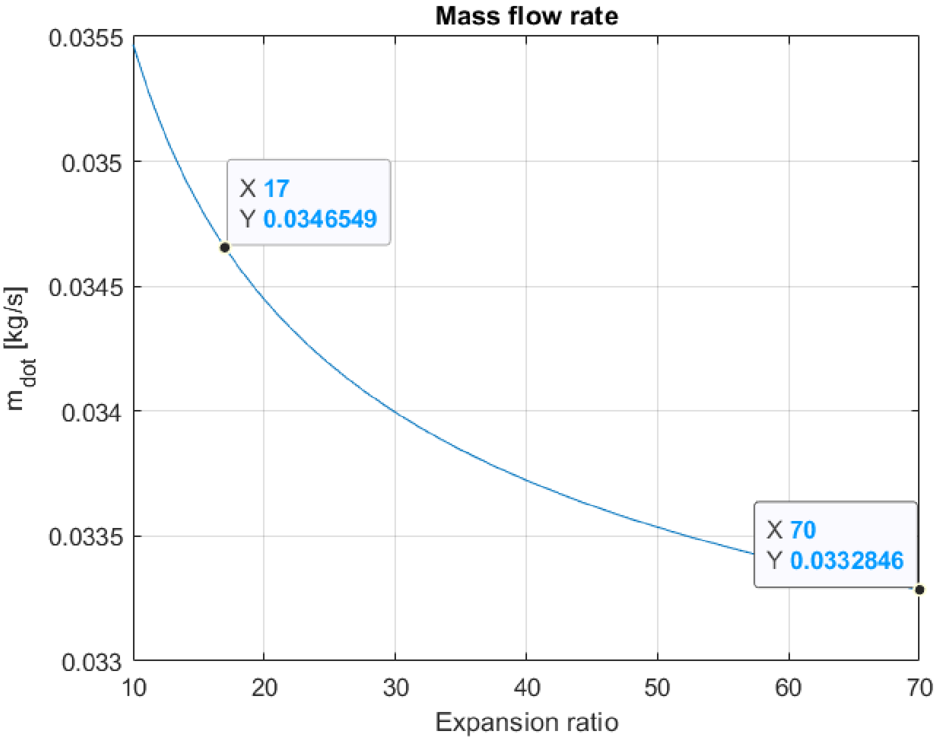

**Figure C.3:** Relationship between the mass flow rate and the expansion ratio of the bell nozzle.

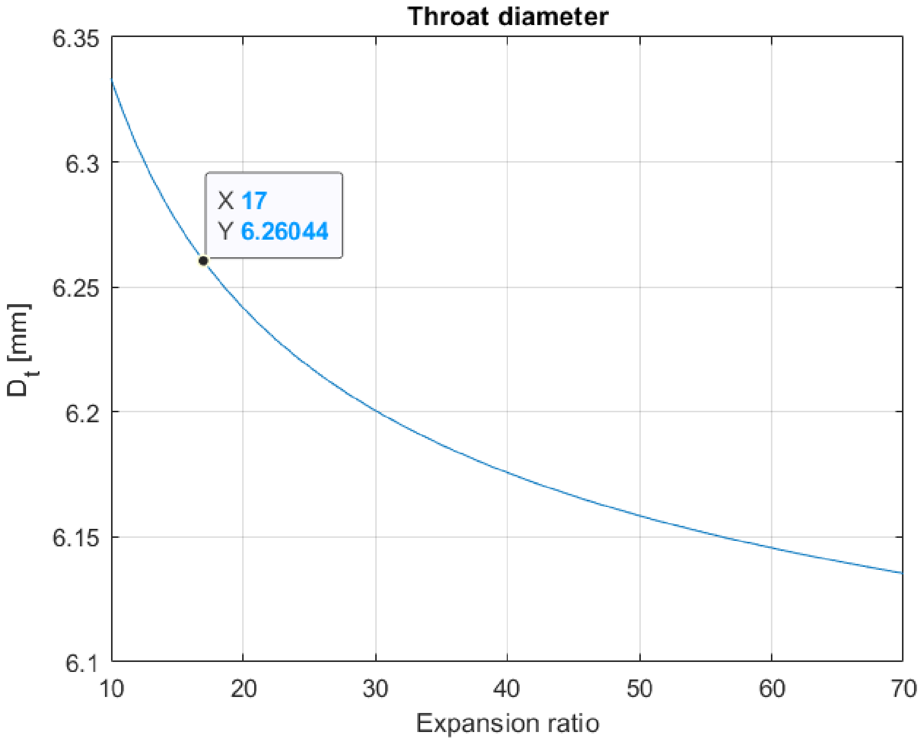

**Figure C.4:** Relationship between the throat diameter and the expansion ratio of the bell nozzle.

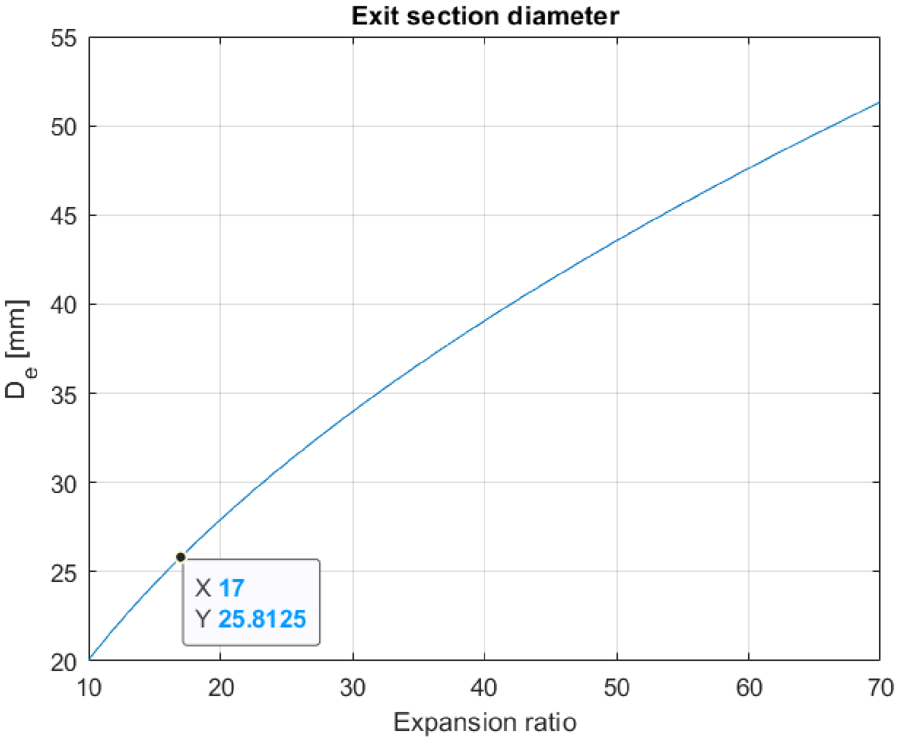

**Figure C.5:** Relationship between the exit section diameter and the expansion ratio of the bell nozzle.

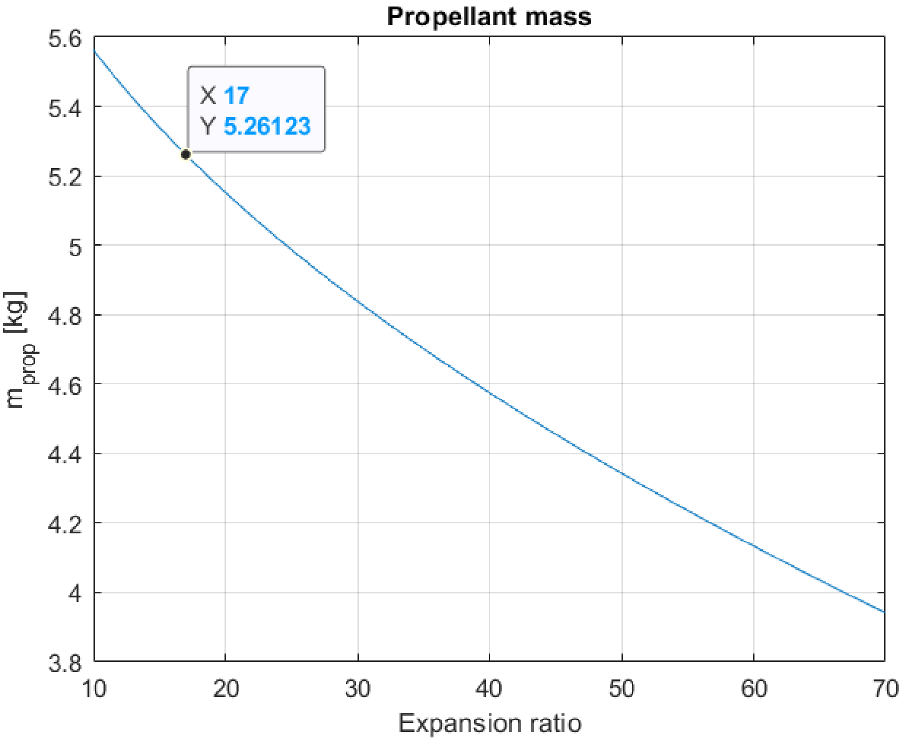

**Figure C.6:** Relationship between the propellant mass and the expansion ratio of the bell nozzle.

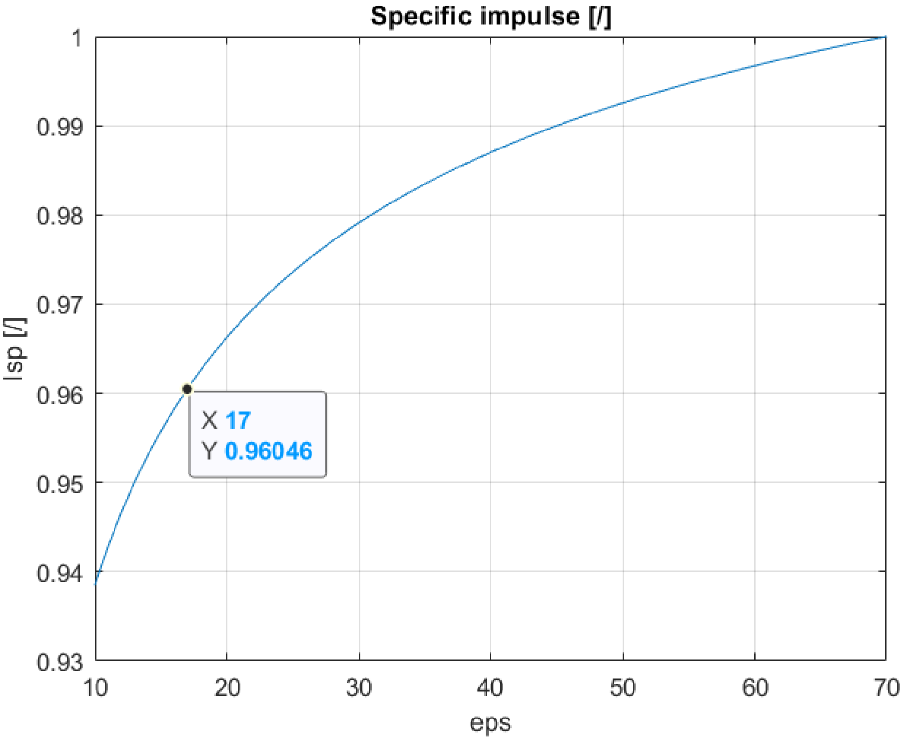

**Figure C.7:** Relationship between the specific impulse divided by its maximum value (with 70 of expansion ratio) and the expansion ratio of the bell nozzle.

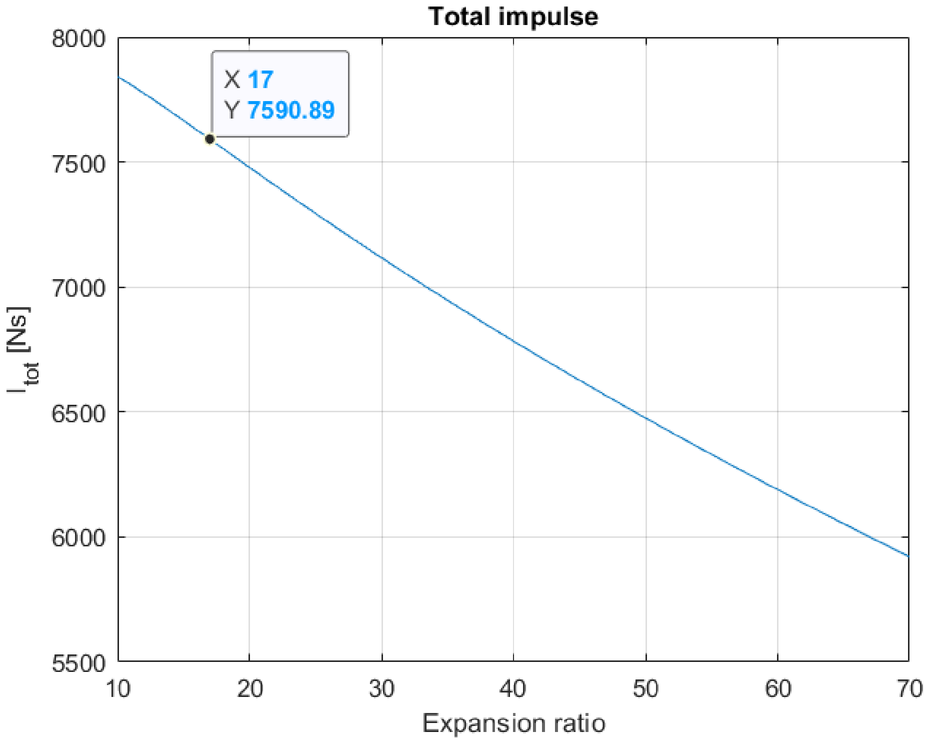

**Figure C.8:** Relationship between the total impulse and the expansion ratio of the bell nozzle.

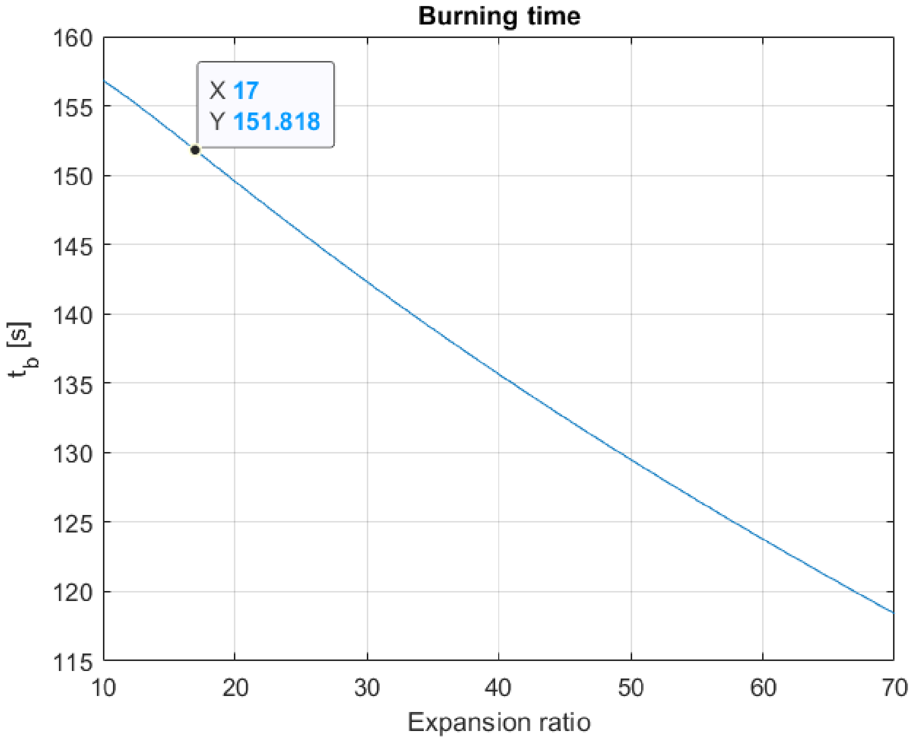

**Figure C.9:** Relationship between the total burning time of the main engine and the expansion ratio of the bell nozzle. This value is the total time the main thruster could fire, which is different from the flight time of the drone.

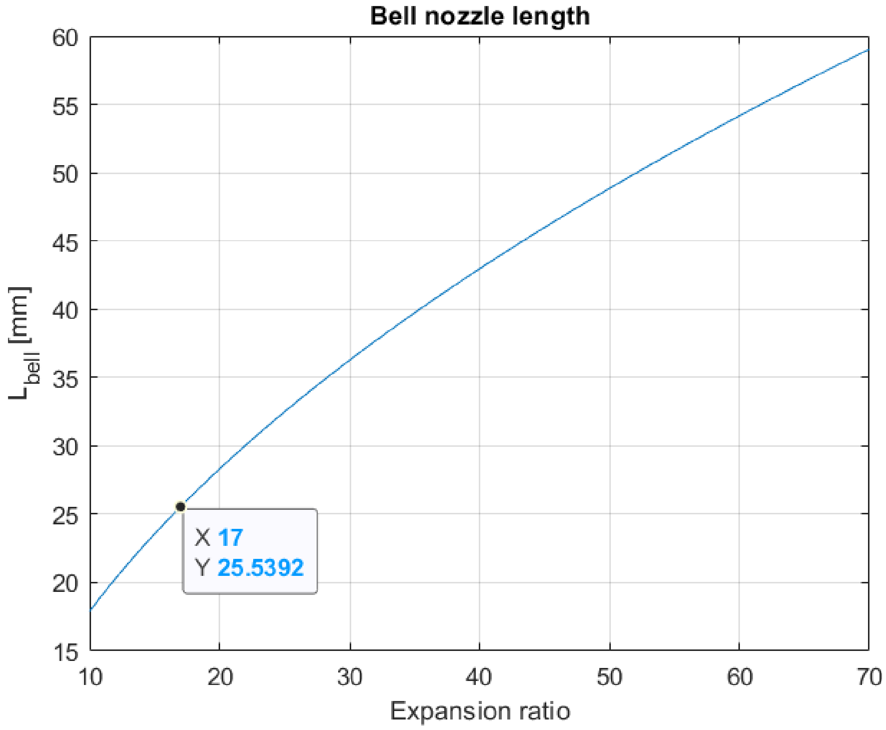

**Figure C.10:** Relationship between the divergent length and the expansion ratio of the bell nozzle.

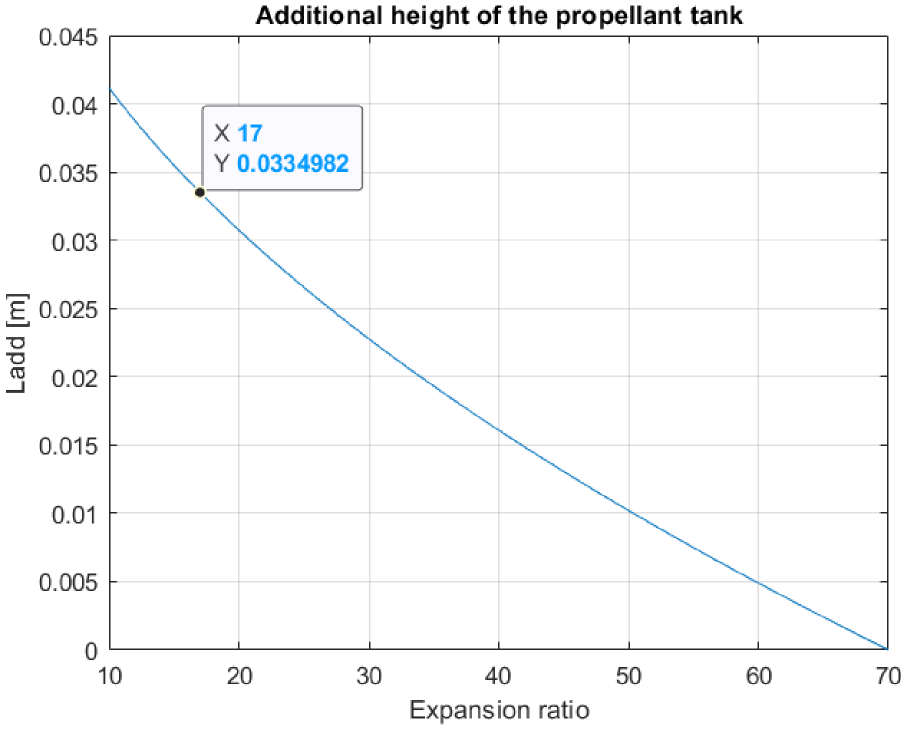

**Figure C.11:** Relationship between the additional height of the propellant tank, resulting from the shorter nozzle, and the expansion ratio of the bell nozzle.

Furthermore, from a different code provided by Stefano Pescaglia in collaboration with Turin Polytechnic, it was possible to analyze the flight profile of the drone. In particular, it can be seen how the decrease in performance, resulting from the shorter nozzle, affects the propellant consumption.

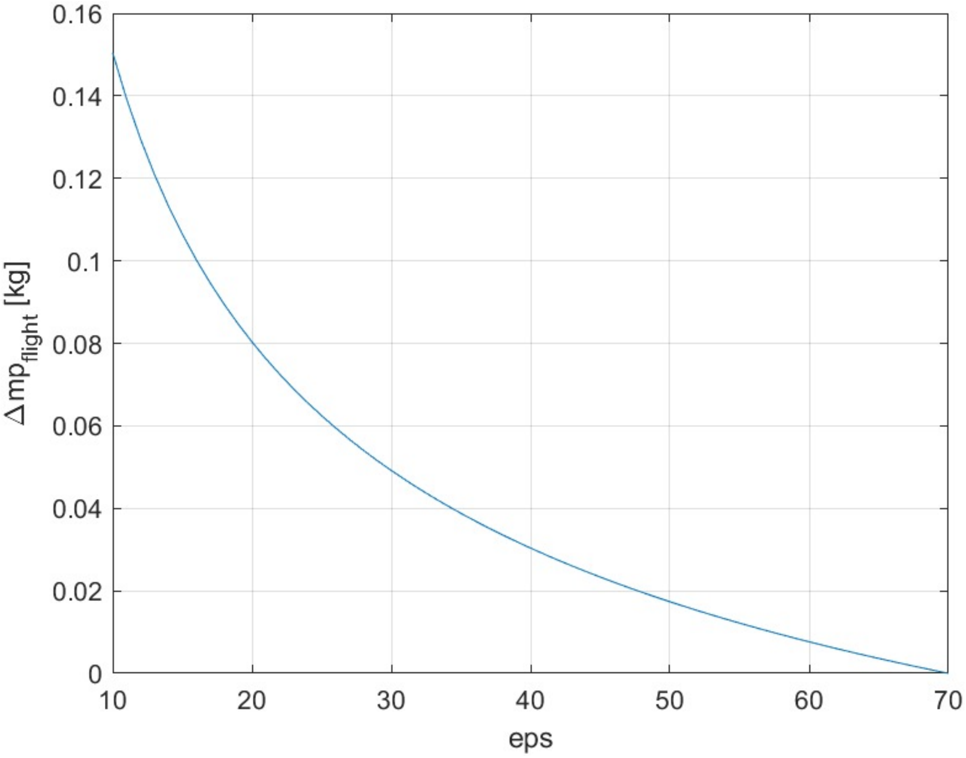

**Figure C.12:** Relationship between the additional propellant consumption, due to the lower $Isp$, and the expansion ratio of the bell nozzle.

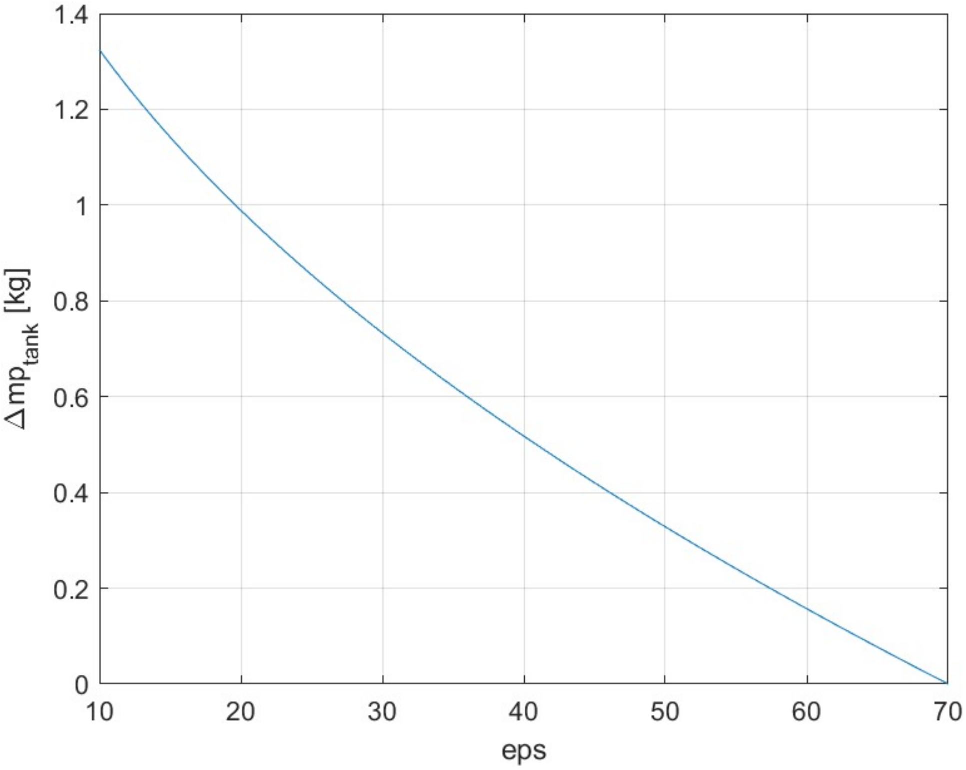

**Figure C.13:** Relationship between the additional storable propellant mass and the expansion ratio of the bell nozzle.

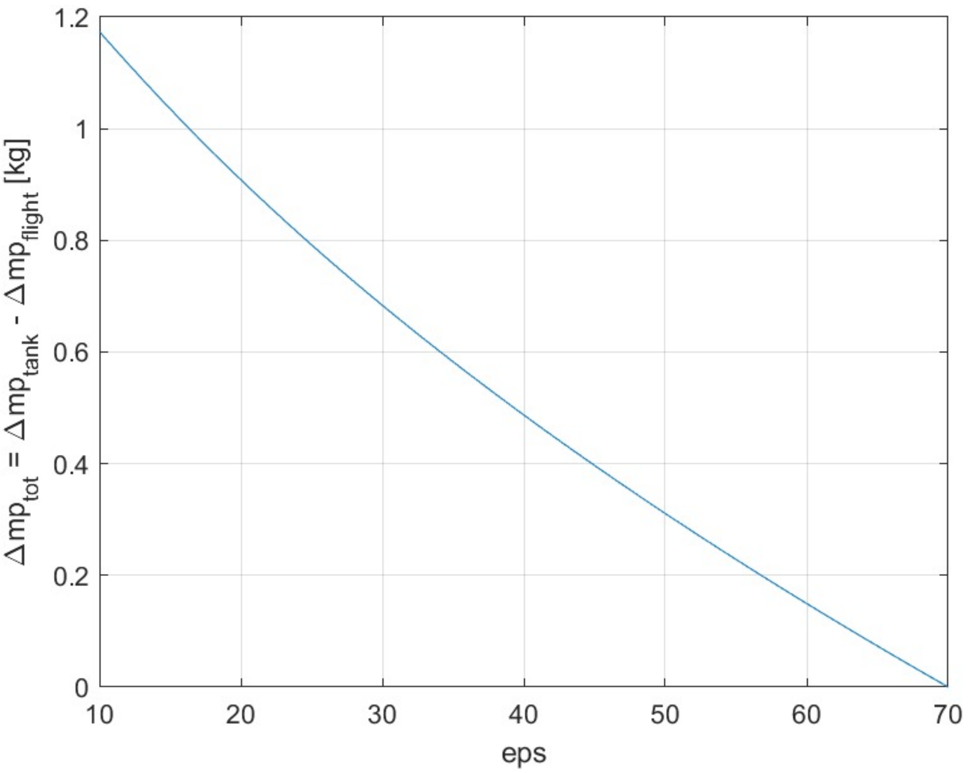

**Figure C.14:** Relationship between the propellant mass gain and the expansion ratio of the bell nozzle.

# Appendix D

# ACS Design

In this annex are shown the main equations that govern the attitude control system design process.

The following equation are directly obtained from Euler equations for the dynamics of a rigid body. Their purpose is to determine the maximum actuation time of each ACS thruster in order to meet the mission navigation requirements. It can be determined as the minimum between the following.
Maximum actuation time of the thrusters firing in x-direction, in order to meet the requirements of rotational speed $\dot{\varphi}$:

$$t_x = \frac{\dot{\varphi}}{\frac{2F_y B_{z\_y}}{I_x}} \tag{D.1}$$

Maximum actuation time of the thrusters firing in y-direction, in order to meet the requirements of rotational speed $\dot{\theta}$:

$$t_y = \frac{\dot{\theta}}{\frac{2F_x B_{z\_x}}{I_y}} \tag{D.2}$$

Maximum actuation time of the thrusters firing in x and y-direction, in order to meet the requirements of rotational speed $\dot{\psi}$:

$$t_z = \frac{\dot{\psi}}{\frac{2F_x B_{y\_x}}{I_z}} \tag{D.3}$$

Maximum actuation time of the thrusters firing in x-direction, in order to meet the requirements of rotation angle precision $\varphi$:

$$t_x = \sqrt{\frac{\varphi}{0.5\frac{2F_y B_{z\_y}}{I_x}}} \tag{D.4}$$

Maximum actuation time of the thrusters firing in y-direction, in order to meet the requirements of rotation angle precision $\theta$:

$$t_y = \sqrt{\frac{\theta}{0.5\frac{2F_x B_{z\_x}}{I_y}}} \tag{D.5}$$

Maximum actuation time of the thrusters firing in x and y-direction, in order to meet the requirements of rotation angle precision $\psi$:

$$t_z = \sqrt{\frac{\psi}{0.5\frac{2F_x B_{y\_x}}{I_z}}} \tag{D.6}$$

The following equations represent the unwanted couples, due to the misalignment and inclination of the main engine axis, and the required minimum thrust to provide in order to compensate them.

Unwanted couples around the x-axis:

$$\begin{aligned} C_1 &= T\cos(x_2)\,x_1 \\ C_2 &= T\sin(x_2)\,B \end{aligned} \quad C_x = |C_1 + C_2| \tag{D.7}$$

Unwanted couples around the y-axis:

$$\begin{aligned} C_3 &= T\cos(x_2)\,x_1 \\ C_4 &= T\sin(x_2)\,B \end{aligned} \quad C_y = |C_3 + C_4| \tag{D.8}$$

Unwanted couple around the z-axis:

$$C_5 = T\sin(x_3)\,x_1 \quad C_z = |C_5| \tag{D.9}$$

Minimum thrust to provide respectively along the y and x-direction to compensate the unwanted $C_x$ and $C_y$ couples:

$$F_y = \frac{C_x}{2B_{z-y}} \quad F_x = \frac{C_y}{2B_{z\_x}} \tag{D.10}$$

Minimum thrust to provide respectively along the x or y-direction to compensate the unwanted $C_z$ couple:

$$F_{xplus} = \frac{C_z}{2B_{y\_x}} \quad F_{yplus} = \frac{C_z}{2B_{x\_y}} \tag{D.11}$$

Where $x_1$ refers to the axis offset of 1 $mm$, $x_2$ refers to the axis radial inclination of 0.5° and $x_3$ to the axis tangential inclination of 0.5°. $T$ is the main engine nominal thrust and $L$ is the nozzle to mass center distance.

# Appendix E

# Components dimensions

In this annex are shown in detail the dimensions of the most relevant components of the new LuNaDrone design. Each value is expressed in millimeters.

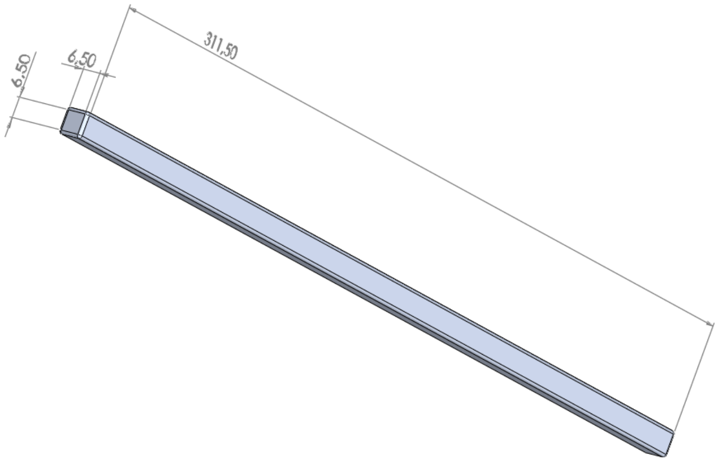

**Figure E.1:** Design of the deployment switches of the LuNaDrone structure, according to ISISPACE guidelines[9].

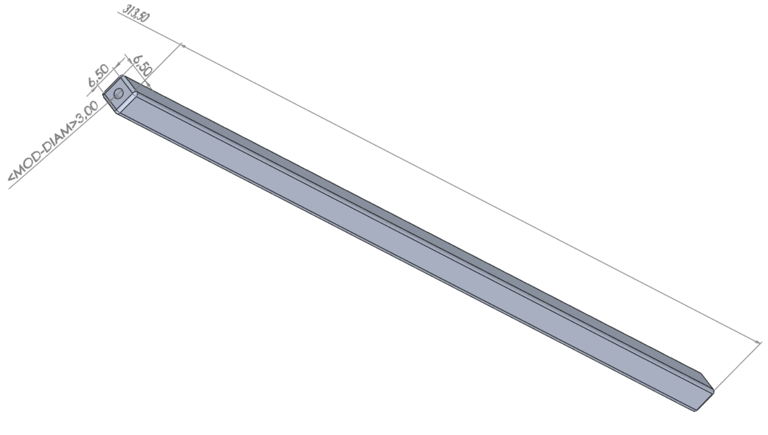

**Figure E.2:** Design of the separation springs of the LuNaDrone structure, according to ISISPACE guidelines[9].

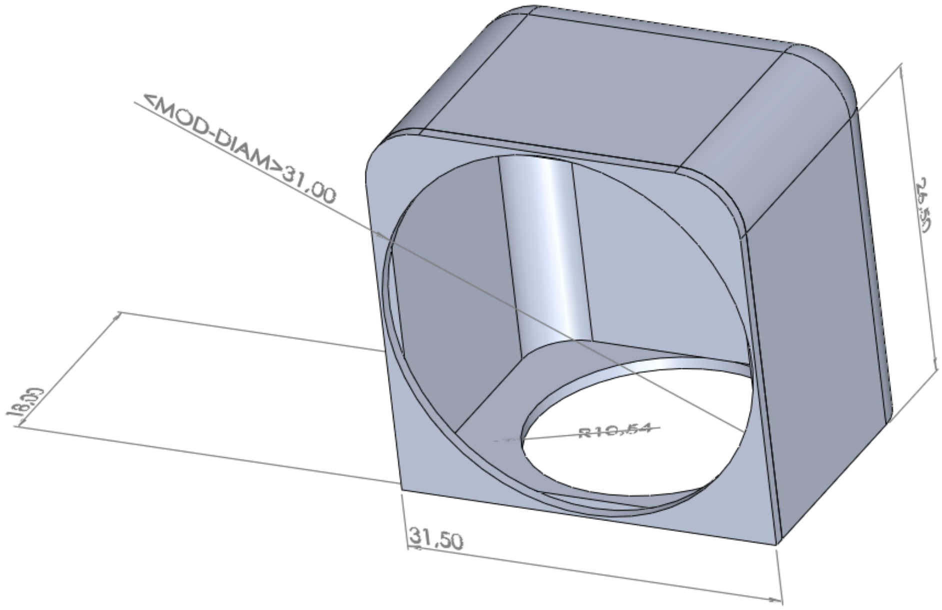

**Figure E.3:** Design of the LuNaDrone combustion chamber.

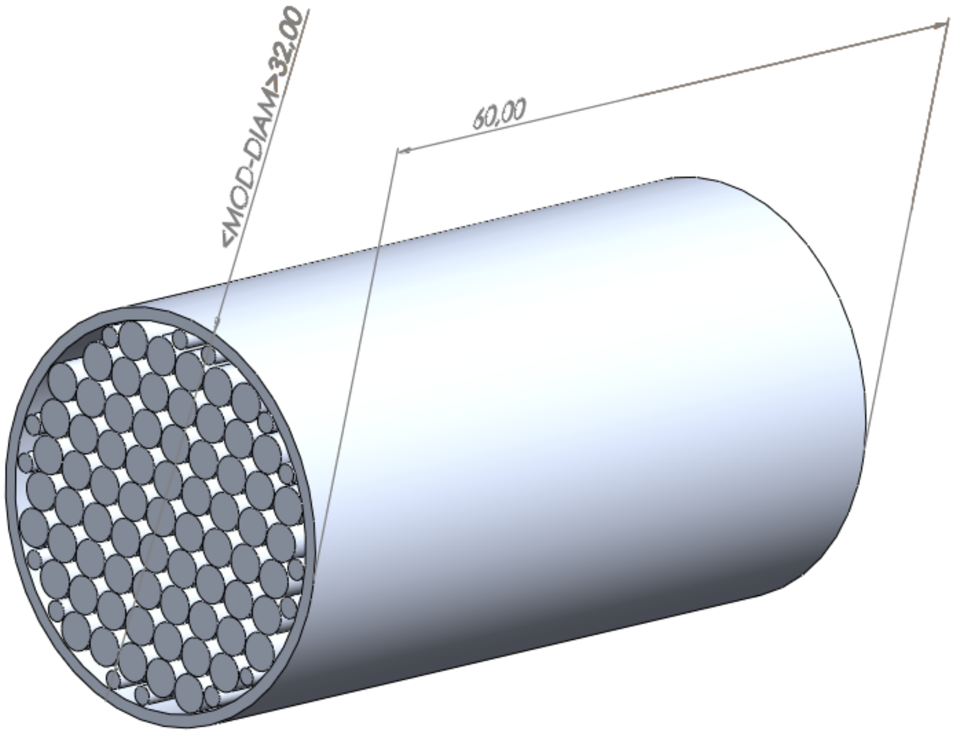

**Figure E.4:** Design of the LuNaDrone catalytic bed.

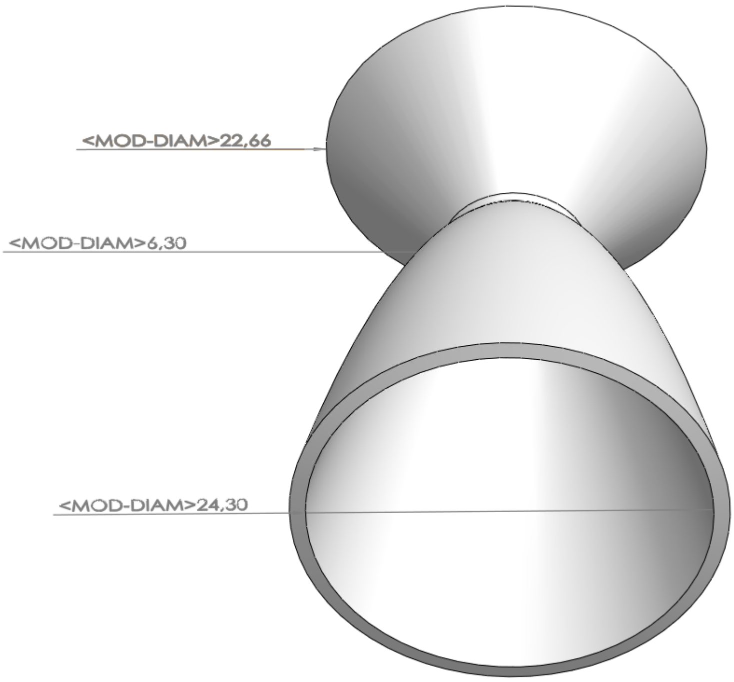

**Figure E.5:** Design of the LuNaDrone main thruster nozzle: inlet, throat and exit section diameters.

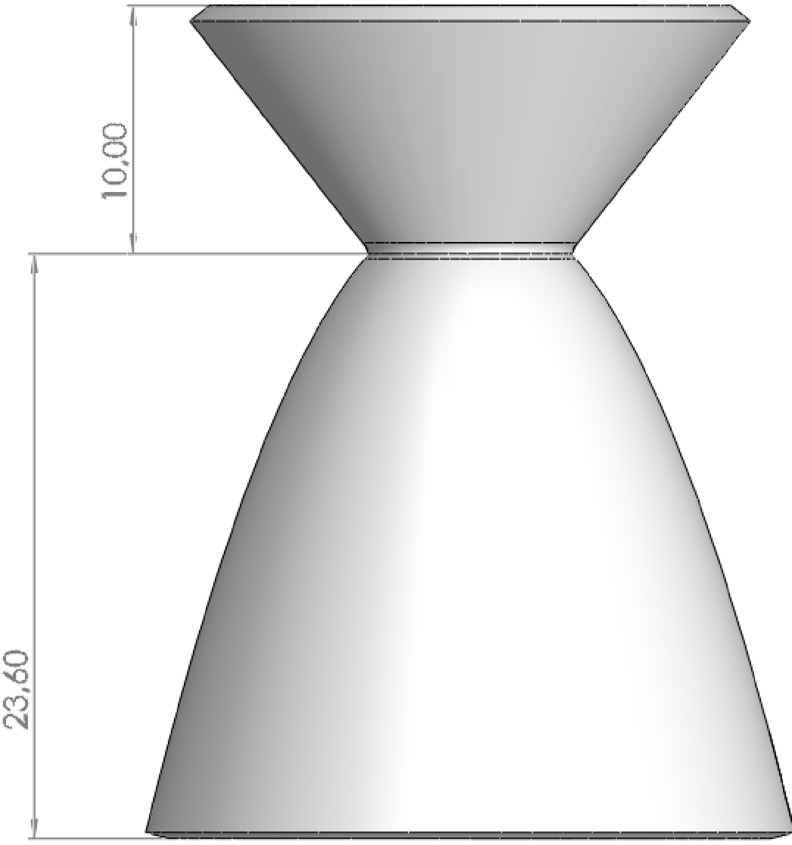

**Figure E.6:** Design of the LuNaDrone main thruster nozzle: convergent and divergent length.

**Figure E.7:** Design of the four combustion chamber supports, each one inclined by 45°.

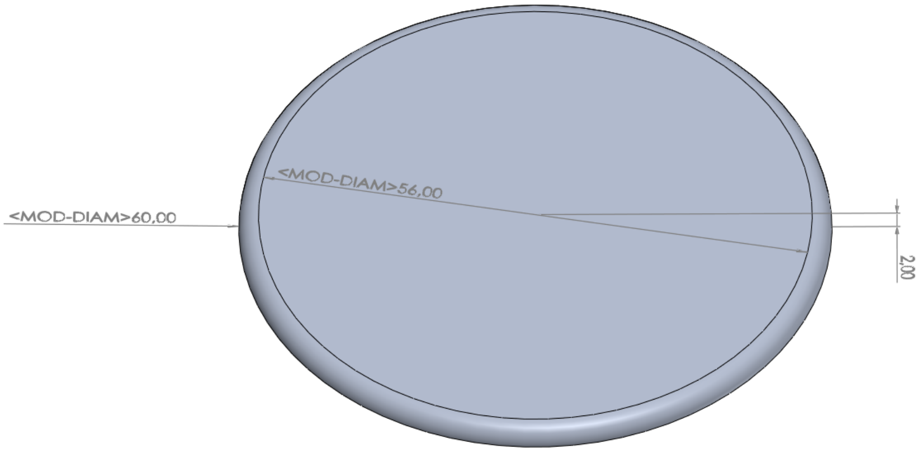

**Figure E.8:** Design of the tank Ergal 7075 disc reinforcements.

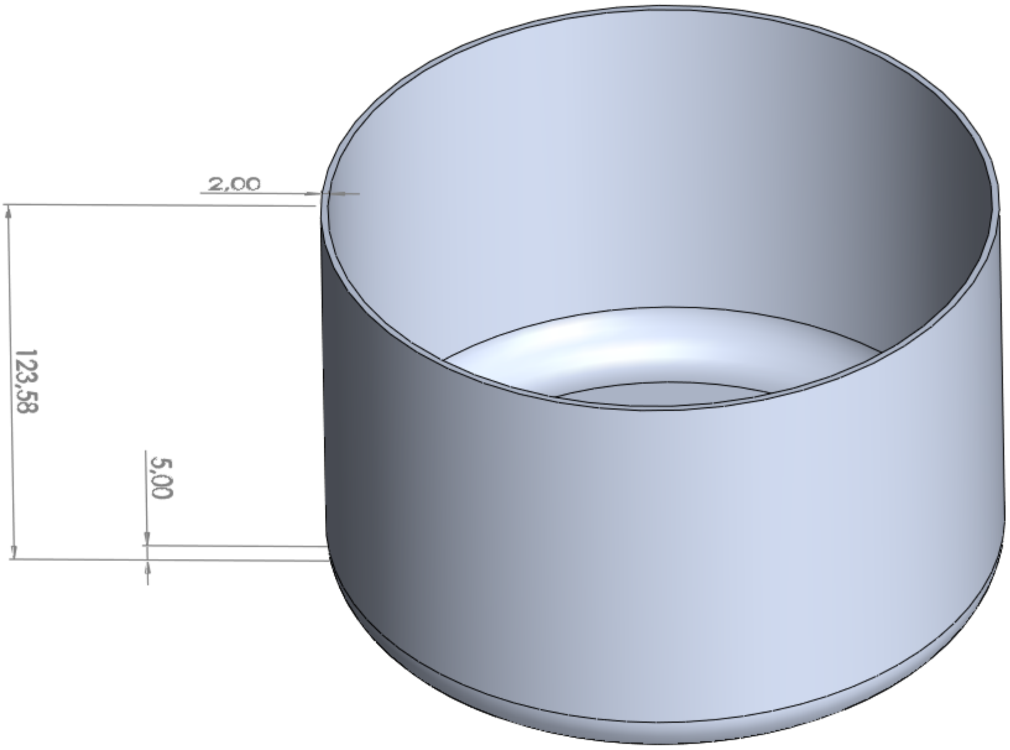

**Figure E.9:** Design of the LuNaDrone propellant tank.

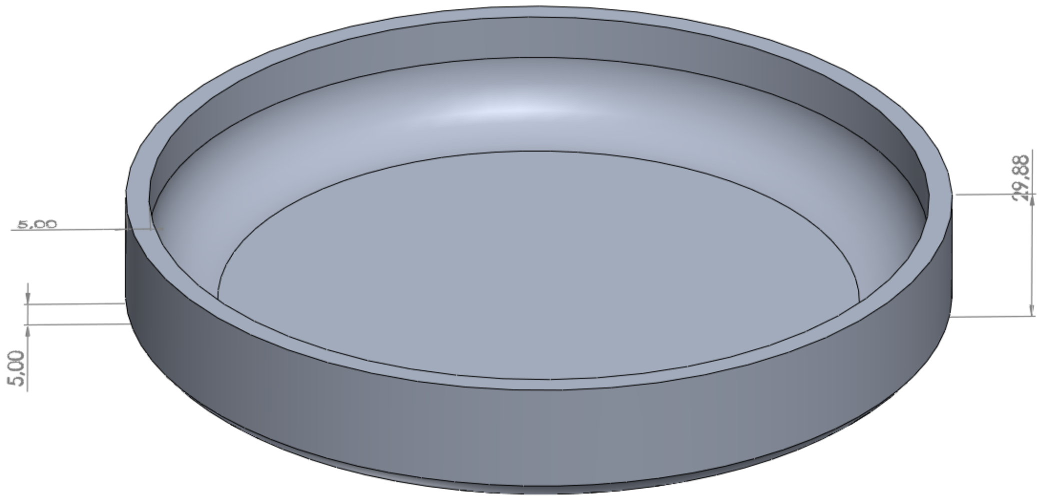

**Figure E.10:** Design of the LuNaDrone propellant tank cap.

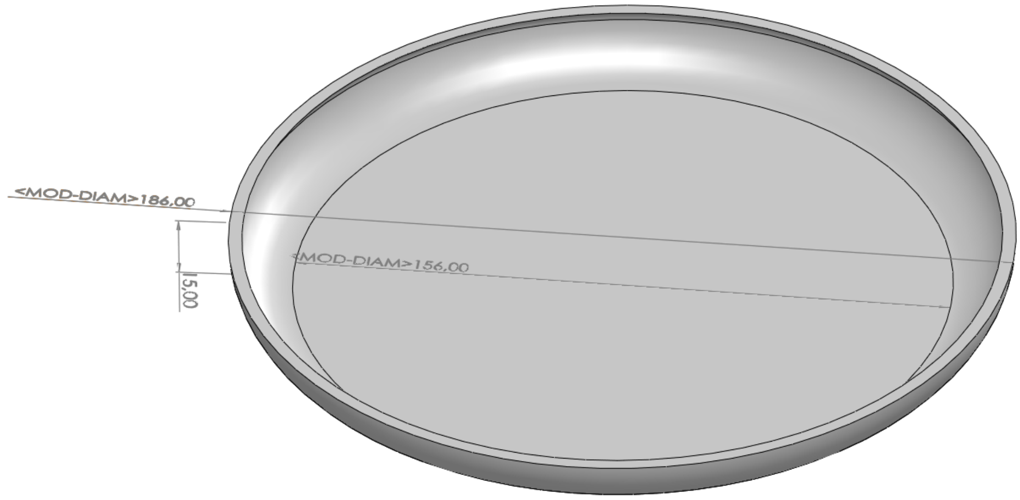

**Figure E.11:** Design of the Teflon separation element of the propellant tank.

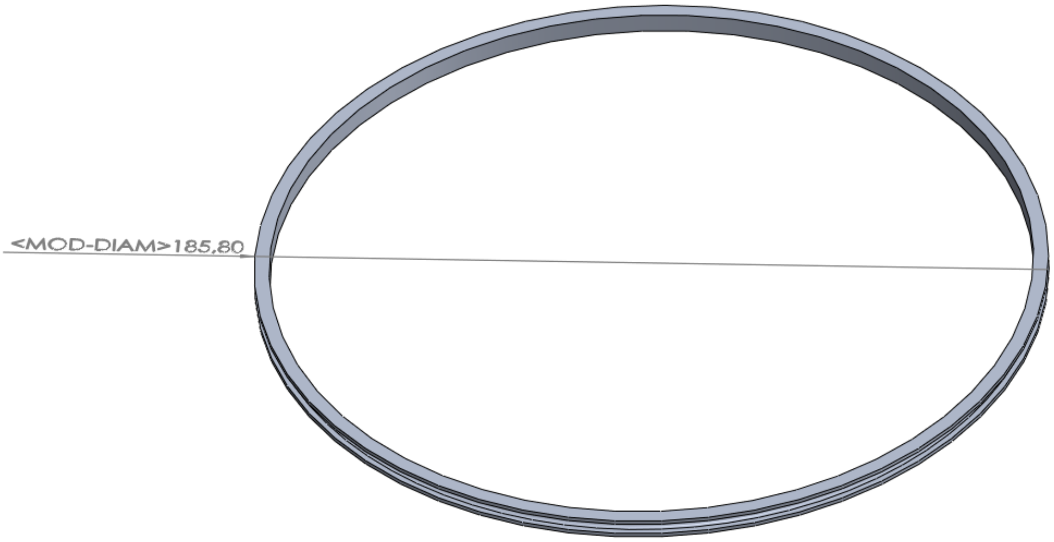

**Figure E.12:** Design of the O-Ring sealing gasket.

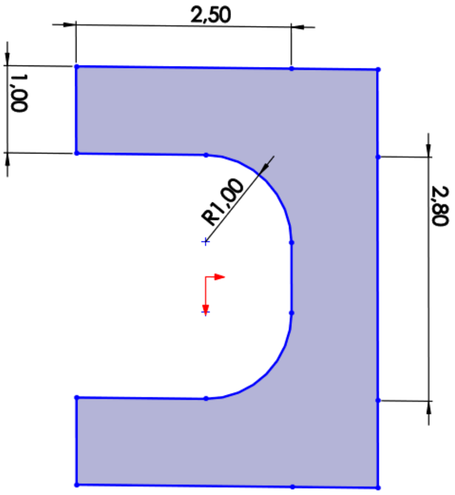

**Figure E.13:** Sketch of the O-Ring sealing gasket section.

**Figure E.14:** Design of the O-Ring sealing.

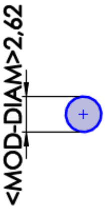

**Figure E.15:** Sketch of the O-Ring sealing section.

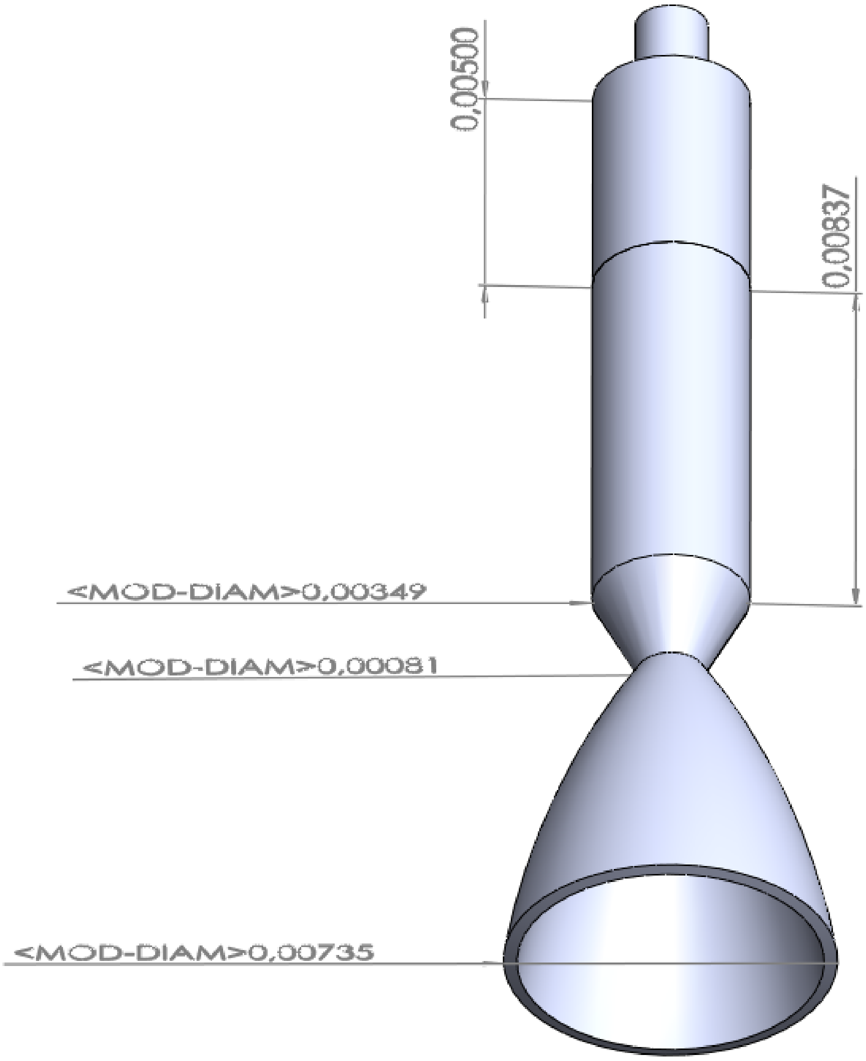

**Figure E.16:** Design of each ACS thruster.

# Bibliography

[1] S. Afandizadeh and E.A. Foumeny. "Design of packed bed reactors: guides to catalyst shape, size, and loading selection". In: *Applied Thermal Engineering, Volume 21, Issue 6, April 2001, Pages 669-682* (2001).

[2] Amphenol, ed. *JS8741 Integrated Pipe Clip Surface Temperature Sensor*. Amphenol. 2019. URL: `https://f.hubspotusercontent40.net/hubfs/9035299/Documents/AAS-920-700D-Thermometrics-JS8741-PipeClip-100119-web.pdf`.

[3] ArianeGroup, ed. *20 N Chemical Monopropellant Hydrazine Thruster*. ArianeGroup. 2020. URL: `https://www.ariane.group/en/equipment-and-services/satellites-and-spacecraft/20n/`.

[4] Hatem Belal. "Modeling of Hydrazine Decomposition for Monopropellant Thrusters". In: *13th International Conference on AEROSPACE SCIENCES AVIATION TECHNOLOGY, ASAT- 13* (2009).

[5] ECSS, ed. *ECSS – A Single Set of European Space Standards*. ECSS. 1996. URL: `https://ecss.nl/home/ecss-a-single-set-of-european-space-standards/`.

[6] Emerson.com, ed. *TESCOM™ BB1 Series Pressure Regulator OEM*. TESCOM. 2022. URL: `https://www.emerson.com/en-us/catalog/tescom-bb-1`.

[7] Mooristica E Packaging Fondazione Istituto Tecnico Superiore Meccanica Meccatronica, ed. *Alluminio e leghe di alluminio*. Fondazione Istituto Tecnico Superiore Meccanica, Meccatronica, Mooristica E Packaging. 2017. URL: `https://itsmaker.it/wp-content/uploads/2018/10/ALLUMINIO-E-LEGHE-DI-ALLUMINIO.pdf`.

[8] ISISPACE, ed. *12-Unit CubeSat structure*. ISISPACE. 2021. URL: `https://www.isispace.nl/product/12-unit-cubesat-structure/`.

[9] ISISPACE, ed. *CubeSat Design Specification (CDS)*. ISISPACE. 2004. URL: `https://org.ntnu.no/studsat/docs/proposal_1/A8%20-%20Cubesat%20Design%20Specification.pdf`.

[10] Afroz Javed and Debasis Chakraborty. "Numerical Simulations of Canted Nozzle and Scarfed Nozzle Flow Fields". In: *Journal of The Institution of Engineers (India): Series C Mechanical, Production, Aerospace and Marine Engineering. The final publication is available at link.springer.com* (2016).

[11] Keller, ed. *Trasduttori di pressione serie 6LHP*. Keller. 2022. URL: `https://keller-druck.com/it/prodotti/trasduttori-di-pressione/trasduttori-di-alta-pressione-oem/serie-6lhp`.

[12] Eric Pereira Kevin Martin and Finn O'Brien. "Hydrogen Peroxide Propulsion System for Nanosatellites". In: *NAG1702, WORCESTER POLYTECHNIC INSTITUTE* (2017).

[13] NASA, ed. *State-of-the-Art of Small Spacecraft Technology. 6.0 Structures, Materials, and Mechanisms*. NASA. 2021. URL: `https://www.nasa.gov/smallsat-institute/sst-soa/structures-materials-and-mechanisms#6.2`.

[14] Rick Newlands. “The Thrust Optimised Parabolic nozzle”. In: *Aspire Space Technical papers* (2017).

[15] B Gherman O Dumitrescu and T Tipa. “Development of a Laval nozzle for a cold gas propulsion system”. In: *IOP Conference Series: Materials Science and Engineering* (2018).

[16] Parker, ed. *Parker O-Ring Handbook*. Parker. 2021. URL: `https://www.parker.com/Literature/O-Ring%20Division%20Literature/ORD%205700.pdf`.

[17] Gabriele Podestà. “Lunar Nano Drone for a mission of exploration of lava tubes on the Moon: Propulsion System”. thesis. 2020.

[18] American Industrial Hygiene Association Quarterly. “Hydrogen Peroxide 90%”. In: *American Industrial Hygiene Association Quarterly, 18:3, 275-276, DOI: 10.1080/00968205709343507* (2008).

[19] Richard Nakka’s Experimental Rocketry Web Site, ed. Richard Nakka. 2016. URL: `https://www.nakka-rocketry.net/th_thrst.html#:~:text=The%20total%20thrust%20produced%20is,1%2C%20then%20F%20%3D%200.`.

[20] TAPPI, ed. TAPPI. 2010. URL: `https://www.fpl.fs.fed.us/documnts/pdf2010/fpl_2010_anderson001.pdf`.

[21] Accu Dyne Test, ed. Accu Dyne Test. 2022. URL: `https://www.accudynetest.com/visc_table.html?sortby=sort_surface_tension%20DESC#015`.

[22] TheLeeCompany, ed. *The Lee Company, ENGINEERING TOOLS OVERVIEW*. TheLeeCompany. 2022. URL: `https://www.theleeco.com/support-resources/engineering-tools/`.

[23] UniPi, ed. *Lezioni sull’analisi di piastre circolari assialsimmetriche*. UniPi. 2013. URL: `http://www.dimnp.unipi.it/leonardo-bertini/Corsi/CAC/Materiale%20didattico/Lez2-Piastre%20circolari%20assialsimmetriche.pdf`.

[24] Wikipedia, ed. *Ergal*. Wikipedia. 2021. URL: `https://it.wikipedia.org/wiki/Ergal`.

[25] Wikipedia, ed. *Nozzle extension*. Wikipedia. 2021. URL: `https://en.wikipedia.org/wiki/Nozzle_extension`.